

VRIJE UNIVERSITEIT

# Wavelength-resolved Extreme Ultraviolet Lensless Imaging and Metrology

ACADEMISCH PROEFSCHRIFT

ter verkrijging van de graad Doctor aan  
de Vrije Universiteit Amsterdam,  
op gezag van de rector magnificus  
prof.dr. V. Subramaniam,  
in het openbaar te verdedigen  
ten overstaan van de promotiecommissie  
van de Faculteit der Bètawetenschappen  
op vrijdag 10 januari 2020 om 13.45 uur  
in de aula van de universiteit,  
De Boelelaan 1105

door

Gijsbert Simon Matthijs Jansen  
geboren te Utrecht

promotor: prof.dr. K.S.E. Eikema  
copromotor: dr. S. Witte

*Sometimes it's the detours which turn out to be the fruitful ideas.*  
Roger Penrose

This thesis was approved by the members of the reviewing committee:

Prof. Dr. K.J. Boller	(Universiteit Twente)
Prof. Dr. W.M.J.M. Coene	(Technische Universiteit Delft)
Prof. Dr. M.L. Groot	(Vrije Universiteit Amsterdam)
Dr. P.M. Kraus	(ARCNL)
Prof. Dr. S. Matthias	(Georg-August-Universität Göttingen)



The research reported in this thesis was carried out at the Advanced Research Center for Nanolithography (ARCNL), a public-private partnership between the University of Amsterdam (UvA), Vrije Universiteit Amsterdam (VU Amsterdam), the Netherlands Organization for Scientific Research (NWO), and the semiconductor equipment manufacturer ASML.

The front cover shows the result of supercontinuum generation by tightly focusing the pulses normally used for high-harmonic generation in air. Due to the very high intensity, the self-focused pulse breaks up into several filaments, leading a complicated and colorful pattern. The pattern is projected on a white screen and photographed.

The flip book in the margins of Chapter 1 - 9 shows extreme ultraviolet interference as a function of time-delay. These results are explained in Chapter 4.

The images on the backcover show microscopic images of the logos of the VU university and ARCNL, acquired using diffractive shear interferometry, which is explained in Chapter 5.



# Contents

<b>1</b>	<b>Introduction</b>	<b>1</b>
1.1	Microscopy	1
1.2	X-ray microscopy	3
	Lensless X-ray microscopy	5
	Light sources	6
1.3	Multicolor microscopy	8
	Fourier-transform interferometry	9
1.4	Outline of this thesis	10
<b>2</b>	<b>A table-top source of coherent extreme ultraviolet light</b>	<b>13</b>
2.1	High-harmonic generation	13
	The single atom response	13
	Phase matching of high harmonics	15
2.2	Ultrafast optics	17
	Dispersion management	18
	Ultrafast laser systems	20
2.3	Amplification of femtosecond optical pulses	21
	Chirped pulse amplification	23
	The pump laser	26
	Non-collinear optical parametric chirped pulse amplification	31
<b>3</b>	<b>Interference and diffraction</b>	<b>35</b>
3.1	Waves	35
	Fourier transform spectroscopy	38
3.2	Diffraction	39
	Coherent diffractive imaging: phase retrieval methods	41
	Holography	45
	Monochromaticity as a requirement for CDI	47

<b>4</b>	<b>Spatially Resolved Fourier Transform Spectroscopy in the Extreme Ultraviolet</b>	<b>51</b>
4.1	Introduction	52
4.2	Experimental setup	53
4.3	Extreme ultraviolet interference: results and analysis	55
	Spatial interference	55
	Temporal interference	56
4.4	Spatially resolved spectroscopy	59
4.5	Conclusion	61
4.6	Supplementary material	61
	Birefringent wedge-based interferometer	61
	High-harmonic generation geometry	62
	Single-shot Fourier Transform interferometry	63
<b>5</b>	<b>Diffraction shear interferometry for extreme ultraviolet high-resolution lensless imaging</b>	<b>65</b>
5.1	Introduction	66
5.2	Spatial shearing interferometry of diffraction patterns	68
	Interference of diffraction patterns	68
	Image reconstruction	70
	Comparison between DSI and single-beam CDI	72
5.3	Experimental demonstration of DSI using high-harmonics	75
	Fourier-transform holography	75
	DSI reconstruction	78
	DSI imaging of complex objects	79
5.4	Conclusions	80
5.5	Appendix: Holography in a DSI setting	81
<b>6</b>	<b>Broadband extreme ultraviolet dispersion measurements using a high-harmonic source</b>	<b>85</b>
6.1	Introduction	86
6.2	Experimental setup	87
6.3	Analysis	89
6.4	Experimental results and discussion	93
<b>7</b>	<b>Outlook on quantitative lensless imaging</b>	<b>97</b>
7.1	Spectral resolution with a wide field of view	98

<b>8 Spectrally resolved single-shot wavefront sensing of broadband high-harmonic sources</b>	<b>103</b>
8.1 Introduction	104
8.2 Spectrally resolved wavefront characterization	106
Spectroscopic Hartmann mask design	106
Measuring HHG wavefront data	108
SHM diffraction pattern analysis	111
Wavefront reconstruction	112
8.3 Wavefront characterization of a high-harmonic beam	113
Wavefront reconstructions of individual harmonics	113
Spectroscopic wavefront analysis	115
Detection of HHG pulse front tilts	117
8.4 Conclusions	119
<b>9 Intrinsic wavefront variations in gas-cell-based high-harmonic generation</b>	<b>121</b>
9.1 Chromatic wavefront variation of high harmonics	121
9.2 The Lund high-power EUV beamline	122
9.3 Measurement analysis	125
9.4 Preliminary results	126
9.5 Outlook	132
<b>Bibliography</b>	<b>135</b>
<b>List of Publications</b>	<b>157</b>
<b>Summary</b>	<b>159</b>
<b>Samenvatting</b>	<b>163</b>
<b>Dankwoord</b>	<b>175</b>

# Introduction

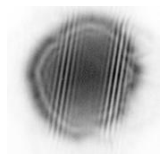
## 1.1 Microscopy

Nowadays, the microscope is regarded as one of the most important instruments in science. While simple lenses have been used to magnify objects already for many centuries, it was the development of a compound microscope which really started the field of microscopy in the early seventeenth century. Not so long after this discovery, scientists Antonie van Leeuwenhoek and Robert Hooke used microscopes to discover and describe life on the microscale. With that, the microscope was firmly set as one of the most powerful and widespread tools of science.

Since the seventeenth century, there has been a continuous effort to develop more powerful microscopes. Of particular interest are the discoveries by Ernst Abbe in the second half of the nineteenth century. Not only did he contribute significantly to the theory of lens design, he also demonstrated that the achievable resolution of an optical microscope is limited by the wavelength of the illumination. The *Abbe diffraction limit* states that the minimum resolvable distance  $d$  is given by

$$d = \frac{\lambda}{2n \sin \theta}, \quad (1.1)$$

where  $\lambda$  is the illumination wavelength and  $n \sin \theta$  is the numerical aperture of the optical system [1]. The numerical aperture depends on the maximum scattering angle  $\theta$  captured by the optical system and



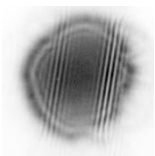
the refractive index  $n$ . It follows that the resolution of a microscope operating in air or vacuum is limited to  $\lambda/2$ . Immersion microscopes, in which the sample is immersed in a high-refractive index fluid, can perform slightly better, but improvements larger than 50% are very hard to achieve. Therefore, the limit of optical microscopes is typically limited to 200 nm.

While this resolution is sufficient for many applications, including for example cellular biology, there are also many applications which require a higher resolution. For example, the typical size of a virus is only 100 nm, and a strand of DNA is only 2 nm wide. Another application area for high-resolution microscopy that is rapidly becoming more important is nanotechnology. Transistors, the base component driving the digital world, currently have 10 nm gates, and there is a continuous drive to make them ever smaller [2].

Over the years, there have been many successful approaches to push the resolution in microscopy beyond the 200 nm limit for visible light. These approaches include electron microscopy, scanning-probe microscopy and super-resolution fluorescence microscopy. Of these, electron microscopy is the oldest technique. The first electron microscope which performed better than an optical microscope was developed in 1933 [3]. Nowadays, electron microscopy can be used to resolve the position of individual atoms in a sample. Such extreme resolutions are possible because the resolution is limited by the electron characteristic wavelength, instead of the visible light photons used in optical microscopy.

Scanning probe microscopy is a family of imaging techniques which work by scanning a probe over the sample. The first of these techniques, scanning tunneling microscopy (STM), was developed in 1981 [4]. In STM, the current from sample to the probe is measured, yielding the local electronic density of states. Lacking a lens-based imaging system, the resolution in scanning probe microscopy is not limited by the illumination wavelength but rather by the probe size and shape. With a very sharp single-atom tip, many scanning probe microscopy techniques are able to resolve individual atoms in the sample.

In 2014, the Nobel prize was awarded to Eric Betzig, William Moerner and Stefan Hell for their development of a class of super-resolved fluorescence microscopy techniques. Contrary to the previ-



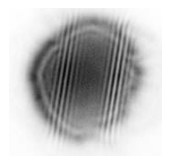
ously mentioned techniques, fluorescence microscopy employs ‘normal’ visible or infrared photons for which imaging is bound by the Abbe diffraction limit. There are many different approaches towards super-resolution in fluorescence microscopy, each using a different principle and analysis. For example in PALM, the fluorescence of a few separated molecules is detected [5]. The fluorescence is visible as diffraction limited spots on the camera. Since each must originate from a much smaller molecule, a molecule is detected in the center of the spot. Repeating this many times, a map of molecule positions can be made with much higher resolution than the diffraction limit normally allows.

It is clear that there are numerous microscopy techniques, and more are being developed. In fact, a single thesis would not nearly be enough to describe all of them. This raises the question: Why? What is the benefit of this? This is not an easy question to answer, but at least part of the answer lies in *applicability*. A microscopy technique is generally developed for a specific set of applications and will have its limitations. Scanning probe microscopy, for example, is strictly limited to the surface of a sample. Electron microscopy can work in transmission of a sample, but requires that the sample is very thin. Fluorescence microscopy can deal with large specimens, but requires the presence of fluorescing molecules. Often, biological samples are stained using special fluorescent molecules.

## 1.2 X-ray microscopy

There is a need for a high-resolution microscopy technique which is compatible with thick samples and which does not depend on the availability of specific components such as fluorescent dyes. X-ray microscopy can fill this gap. X-rays allow for much higher resolutions due to their shorter wavelength. X-rays interact directly with tightly bound core electrons, leading to elemental contrast. While the penetration depth depends strongly on the photon energy, X-ray microscopy is compatible with much larger samples than what can be handled with transmission electron microscopy.

Fig. 1.1 provides an example of the results that can be obtained with X-ray microscopy [6]. In this experiment, 90 projections from



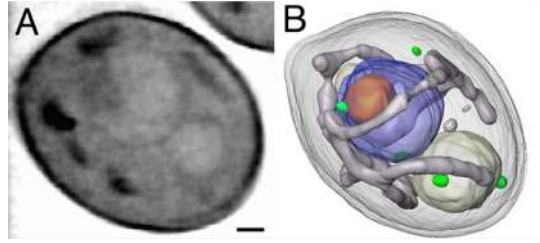


Figure 1.1: **A:** Image of a *C. albicans* cell acquired through soft-X-ray microscopy. **B:** False-color result of a tomographic reconstruction based on a large set of images such as **A**, all taken at different incidence angles. The scale bar has a length of 500 nm and the reconstruction resolution is 50 nm. Image taken from M. Uchida et al., PNAS 106, 19375 (2009)

different angles were used to calculate tomograms with 50 nm resolution for many different *C. albicans* cells. The X-ray wavelength used in this experiment was between 2 and 4 nm, a region known as the water window due to the very low absorption of oxygen compared to carbon and nitrogen. These results demonstrate the promise of X-ray microscopy for microbiology.

Like the other types of microscopy mentioned in section 1.1, X-ray microscopy is a family of techniques. The results in Fig. 1.1 were obtained using a the full-field X-ray microscope based on Fresnel zone plates and a synchrotron light source. The use of diffractive rather than refractive optics and the use of large-scale synchrotron facilities demonstrate some of the complexities of X-ray microscopy. The first of these complexities is highlighted by the use of Fresnel zone plates where an optical microscope would use lenses. At X-ray wavelengths, the refractive index of materials is generally weak while the absorption is significant. It is therefore highly challenging to make good quality lenses for image formation. On the other hand, Fresnel zone plates rely on diffraction rather than refraction. A zone plate is typically a binary amplitude mask of concentric rings of which the width decreases with increasing radius. The resulting diffraction pattern behaves like the light emerging from a lens: it focuses to a small spot or a sharp

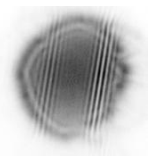


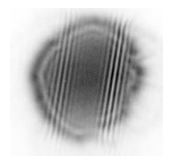
image. Similar to refractive lenses, the resolution offered by Fresnel zone plates is determined by the numerical aperture. As a result, the resolution offered by a zone plate is determined by the width of the thinnest, outermost ring. With the current nanofabrication possibilities, 12 nm resolution zone plates are now commercially available [7]. The resolution does not approach  $\lambda/2$ , as can be achieved with optical wavelengths.

Although zone plates enable very high resolution microscopy, they have several drawbacks. These include low power efficiency, a monochromaticity requirement and a small field of view. Similar to a diffraction grating, a zone plate has several diffraction orders. The first order of diffraction is well focused, the zeroth order is not affected, the minus first order diverges, and higher orders of diffraction cannot be ignored. Combined with absorption losses, this leads to an efficiency of only a few percent. Because a zone plate focuses by diffraction, the focal length scales with the inverse of the wavelength. In order to achieve the desired resolution, the incident light must have a very narrow spectral bandwidth. Finally, zone plates have significant off-axis aberration. As a result, high resolution is only obtained over a small field of view.

### Lensless X-ray microscopy

In the last 20 years, an alternative to zone plate-based X-ray microscopy has rapidly been gaining ground [8]. This alternative, named coherent diffractive imaging (CDI), was first demonstrated in 1999 [9]. CDI is a lensless imaging technique: rather than using lenses, a camera is used to directly capture the scattered light from a sample. The experimental setup for CDI consist of three main components: illumination, an object and a detector, as depicted in Fig. 1.2. The object is illuminated with coherent, monochromatic light. This leads to a diffraction pattern which is directly related to the light field in the object plane; for example in the case of far-field diffraction, the diffraction pattern equals the Fourier transform of the electric field at the object. Therefore, if the diffraction pattern is known, an image of the object can be calculated by wave propagation.

Wave propagation requires knowledge of both the amplitude and phase of the electric field. Since a camera only measures the light



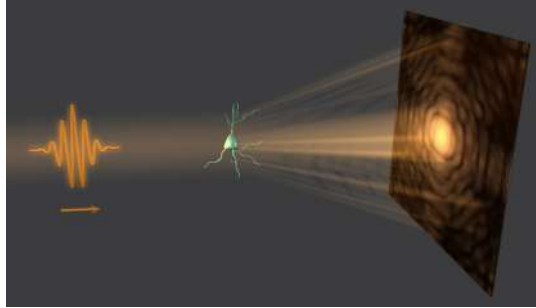
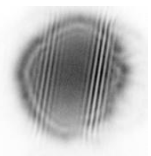


Figure 1.2: Schematic overview of a CDI experiment: light illuminates an object, which scatters part of the light. The resulting diffraction pattern is recorded on a camera.

intensity, the phase is not known. The measurement as shown in Fig. 1.2 does not provide sufficient information: the phase of the diffraction pattern needs to be retrieved as well. The approach in CDI is to use numerical methods to calculate the phase of the diffraction pattern [10]. In general, just the diffraction pattern is not enough information to reconstruct the phase, and some additional information is necessary. For example, it may be known that the object has a certain size significantly smaller than the field of view of the imaging system and that the object is isolated. This finite support is in general enough to enable a phase retrieval algorithm to reconstruct the phase for a diffraction pattern measured with a good signal to noise ratio [11]. In addition to this support-based reconstruction, there exist many different approaches which enable efficient phase retrieval [12], [13]. The resolution in coherent diffractive imaging can be calculated directly from equation 1.1, in which the numerical aperture  $n \sin \theta$  is defined as the largest scattering angle that can still be measured on the camera. Coherent diffractive imaging is therefore well suited for high-resolution X-ray microscopy.

### Light sources

In order to generate good diffraction patterns with a well-defined phase, CDI relies on coherent and monochromatic illumination [14], [15]. The

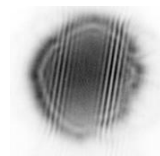


main light sources that have been used for CDI are synchrotrons, and recently, free electron lasers [16], [17]. These are very large facilities in which X-rays are produced from relativistic electron pulses. While the resulting light is not fully coherent, synchrotrons and free-electron lasers provide high intensities, decent monochromaticity and a tuneable wavelength. These light sources are therefore good candidates for high-resolution coherent diffractive imaging.

However, synchrotrons and free-electron lasers are expensive and measurement time at such facilities is usually limited. This is a large difference with other microscopy techniques, where small-scale tabletop microscopes are the norm. A tabletop x-ray coherent diffractive imaging system would increase the impact of high-resolution x-ray microscopy by making it available for a much wider audience. There is therefore a need for compact coherent x-ray light sources. High-harmonic generation provides such a source.

High-harmonic generation (HHG) is a highly nonlinear optical process in which low-energy photons are upconverted to much higher energies. It was first observed by McPherson and coworkers in 1987 [18]. As explained in section 2.1, in HHG an ultrashort intense laser pulse is focused in a generating medium such that the electric field of the light is comparable to the Coulomb potential that the electrons experience. In a process [19] where the electrons are ionized, accelerated and recombined with the parent atom, high energy photons are produced. Despite the high nonlinearity of this process, high-harmonics have a high level of coherence [20]–[22]. The spectrum typically consists of a series narrow peaks at odd multiples of the optical frequency of the original laser pulses [23].

Due to the high spatial coherence of high harmonics, they are well suited for coherent diffractive imaging techniques [24]. As CDI requires monochromatic illumination, the high-harmonics are typically spectrally filtered using multilayer mirrors. These mirrors also focus the light to the sample. HHG-based coherent diffractive imaging has been applied to a variety of samples in imaging systems with a very high ( $> 0.5$ ) numerical aperture, enabling sub-wavelength resolution. Recently, a spatial resolution as high as 12 nm has been reported [25], [26].



### 1.3 Multicolor microscopy

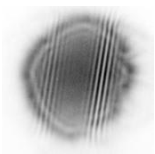
The ability to see the world in color is perhaps the most appreciated feature of the human eye. Without color, a lot of information would be lost, as shown in Fig. 1.3. This is the reason why color photography and motion pictures were pursued already in the early days of photography. Similarly, color plays an important role in visible light microscopy. For visible light, color is typically defined by how humans perceive it. More generally, color can be defined as the distribution of wavelengths present in the radiation.



Figure 1.3: **Left:** Photograph of a garden, without color. **Right:** The same photograph, with color. It is clear that the color picture contains much more information.

The x-ray part of the electromagnetic spectrum can be divided in three parts in order of decreasing wavelength and increasing photon energy: extreme ultraviolet, soft X-rays and hard X-rays. Due to the differing photon energies, these parts of the spectrum have different interactions with matter [27], [28]. Hard X-rays are those with the highest energy. These photons can only be absorbed by the most tightly bound electrons. They are therefore most sensitive to the core levels of heavier metals. Soft X-rays have a lower energy and interact with slightly weaker bound electrons. Soft X-rays were used to achieve the results presented in Fig. 1.1. Extreme ultraviolet have lower energy still and interact strongly with many materials. It is this part of the spectrum that is most relevant for this thesis.

Due on the strong wavelength dependence of X-ray interactions



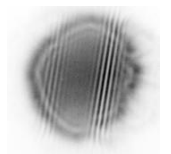
with matter, wavelength-resolved x-ray microscopy has the potential to provide high spatial resolution as well as elemental resolution, pinpointing what material is where in the object. However, like for zone plate-assisted imaging, coherent diffractive imaging requires that the illumination is monochromatic [15], [29]. Wavelength-resolved imaging then requires repeating the procedure for all wavelengths of interest.

One of the key features of high-harmonic generation is that it generates a broad extreme ultraviolet spectrum with excellent coherence. High-harmonic generation is therefore an ideal platform for wavelength-resolved high-resolution microscopy in the extreme ultraviolet and soft-X-ray domains. However, recording diffraction patterns with the full HHG spectrum simultaneously washes out many of the fine details which are crucial for image reconstruction. While lensless imaging with multiple high harmonics simultaneously has been demonstrated [30]–[32], a general wavelength-resolved alternative to coherent diffractive imaging has not been demonstrated. The goal of this thesis is therefore to develop and demonstrate wavelength resolved microscopy and metrology using high harmonics. This will be achieved through interferometry with a pair of phase-locked high-harmonic sources.

### **Fourier-transform interferometry**

Interferometry is a broad family of techniques which employ interference to measure some quantity [33]. Interference is caused by the superposition of waves, and is therefore sensitive to both the amplitude and phase of the constituting waves. There are many examples of interferometry in science, such as Young’s double slit interference, the Michelson-Morley experiment [34] and holography [35]. Particularly impressive are the gravitational wave detectors which recently enabled the discovery of gravitational waves [36]. In these detectors, interference is used to measure minute changes in the length of their arms caused by gravitational waves.

In the context of wavelength-resolved microscopy, it is useful to consider Fourier transform spectroscopy [37]. This technique is commonly used in commercial infrared spectrometers but can be applied in many situations. In general, the light to be measured is split into two equal parts. These parts are then overlapped again with a controllable delay



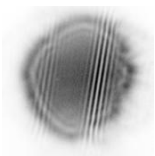
between the parts. A temporal interference pattern can be recorded by scanning the delay and measuring the total intensity. A Fourier transform then yields the spectrum. As Fourier-transform spectroscopy requires only a single intensity detector, it provides an ideal platform to measure the incident light with both spatial and spectral resolution. This can be done using a pixelated detector such as a CCD chip. This technique enables the extraction of monochromatic diffraction patterns from broadband illumination, a requirement for wavelength-resolved CDI.

Fourier transform spectroscopy requires that the light pulses are split into an equal pulse pair with a delay stability that is much better than the wavelength [37], [38]. Furthermore, for coherent diffractive imaging it is desirable that the two beams have a smooth beam profile. In Chapter 4, we demonstrate that this can be achieved using a special common-path interferometer. This enables coherent diffractive imaging with the full, octave-spanning high-harmonic spectrum and provides a unique platform for spectrally resolved metrology in the extreme ultraviolet domain.

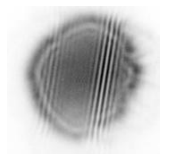
### 1.4 Outline of this thesis

This thesis is structured as follows: In Chapter 2, high-harmonic generation is introduced and the driving laser is described. Chapter 3 provides an introduction on interference, diffraction and lensless imaging. Chapter 4 details our initial results on spatially resolved Fourier transform spectroscopy, including interferometry at wavelengths as short as 17 nm. In Chapter 5, we demonstrate spectrally resolved coherent diffractive imaging through Fourier transform spectroscopy. The differences with conventional coherent diffractive imaging are also explored here. In Chapter 6, dispersion at extreme ultraviolet wavelengths is measured using Fourier transform spectroscopy. Finally, in Chapter 7, an outlook towards further wavelength-resolved lensless imaging is given.

As Roger Penrose said: *‘Sometimes it’s the detours which turn out to be the fruitful ideas.’* Chapter 8 describes such an idea. Using the diffraction of a carefully engineered mask, we measure the wavefronts



for all spectral components of a high harmonic beam. These results led to a collaboration with the group of Anne l'Huillier and Per Johnsson in Lund. Results of wavefront measurements performed on their HHG system in Lund are described in Chapter 9.





# A table-top source of coherent extreme ultraviolet light

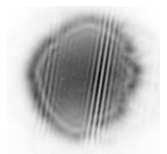
## 2.1 High-harmonic generation

### The single atom response

High harmonic generation is a strong field phenomenon. The electric field of the laser pulse driving it can not be treated as a small perturbation of the potential that is experienced by electrons in the target. The single-atom response can nevertheless be explained to reasonable accuracy with a quasi-classical model, the three-step model of high-harmonic generation [19].

The three-step model is depicted schematically in Fig. 2.1. Initially, a high intensity laser pulse, typically with a visible or infrared wavelength, is incident on an atom in its ground state. The first step is tunnel ionization: the electric field of the laser pulse is strong enough to tilt the Coulomb potential, allowing the weakest-bound electron to tunnel out. The second step is acceleration: the free electron is pushed around by the optical field. The electron is first accelerated away from the parent ion, but half an optical cycle later the electric field reverses and the electron is pushed back to the parent ion. The final step is recombination: the electron is recaptured by the ion and the electron kinetic energy is released as a high-energy photon.

The three step model provides a good qualitative explanation. Nevertheless, a full quantum model is required for an accurate modeling



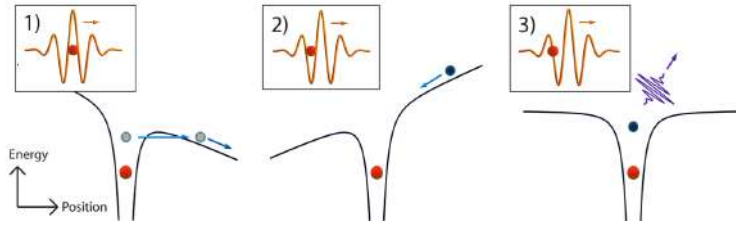


Figure 2.1: Three-panel schematic depiction of the three step model of high-harmonic generation.

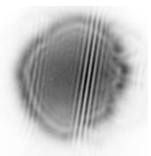
of the HHG process [39]. From a quantum mechanical viewpoint, it becomes clear that the electron is in fact never completely ionized. Rather, the laser pulse tilts the Coulomb potential and therefore allows a part of the electron wavepacket to tunnel into the continuum. There, the wavepacket evolves in the electric field of the pulse. Every half cycle, part of the ionized wavepacket overlaps with the bound wavepacket. The strength of this overlap determines the probability that the wavepacket is reabsorbed and that it emits a high energy photon. Because the wavepacket spreads out in space and time when it is outside of the atom, the probability of recombination decreases with time spent in the continuum.

The maximum achievable emitted photon energy (cut-off) is given by the sum of the ionization potential  $I_p$  and the maximum kinetic energy of the electron, which can be calculated from electrodynamics [39]. This yields

$$E_{max} = I_p + 3.17U_p = I_p + \frac{e^2 E^2}{4m\omega^2}, \quad (2.1)$$

in which  $U_p$  the ponderomotive energy, which depends on the electron mass  $m$ , charge  $e$ , the electric field strength  $E$  and frequency  $\omega$ . This formula implies that the maximum photon energy (or shortest wavelength) depends mainly on three parameters: the atomic species, the light intensity and the wavelength.

In order to generate efficient HHG at high photon energies, noble gasses such as argon, neon and helium are often used. These gasses have a high ionization potential, enabling HHG at shorter wavelengths.



This is offset by a reduction in conversion efficiency: the tightly bound electrons do not ionize easily, leading to a low conversion efficiency. Gases such as krypton and xenon can therefore be used to achieve a better conversion efficiency at longer wavelengths.

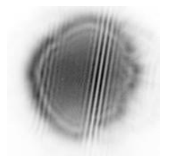
Changing the driving wavelength has proven to be a useful method to control the generated photon energy [40]–[42]. Longer wavelengths lead to higher ponderomotive energy as the electron is accelerated longer in the optical field. This leads directly to higher photon energies. There is a trade-off however, as the electron wavepacket also spreads out more for longer wavelengths. This leads to a lower recombination probability and lower HHG flux.

### Phase matching of high harmonics

One particularly useful feature of HHG which is not explained by the three step model is the high degree of spatial coherence [20], [22]. The three step model explains how a single atom responds to the strong electric field, but it does not explain why the generated extreme ultraviolet (EUV) is predominantly emitted in the direction of the laser beam. In fact, high harmonics typically have a lower divergence than the driving laser.

It is therefore necessary to consider phase matching in HHG. Phase matching is a well known concept from nonlinear optics, for example in the context of second harmonic generation [43]. In order to generate a significant amount of light through the nonlinear process, it is necessary that the generated light from different parts of the HHG interaction zone remain in phase, leading to constructive interference. For example, for second harmonic generation typically a specially selected crystal is used which has both a high nonlinear susceptibility (to generate more frequency-doubled photons), and strong birefringence. By tuning the angle of incidence on the crystal, the effective refractive index can be tuned. Because the driving and generated wavelengths have different polarizations, this can match the phase velocities and ensure phase matching.

In the case of high-harmonic generation, there are other processes which allow phase matching. There are four main contributions to the HHG phase mismatch  $\Delta k$ : the refractive index of the neutral gas, the



dispersion of the free electrons, the geometric phase and the dipole phase which the electrons accumulate during tunnel ionization [44], [45]. For a loosely focused beam, the fundamental laser can be treated as a plane wave with a flat intensity profile. The geometric phase and dipole phase are then approximately zero, and the phase mismatch is given by

$$\Delta k \approx - \underbrace{qp(1 - \eta) \frac{2\pi}{\lambda_L} (\Delta\delta + n_2)}_{\text{neutral gas}} + \underbrace{qp\eta N_a r_e \lambda_L}_{\text{free electrons}}, \quad (2.2)$$

in which  $q$  indicates the high harmonic order,  $p$  is the pressure in bar,  $\eta$  is the ionization fraction,  $\lambda_L$  is the driving laser wavelength,  $\Delta\delta$  is the difference in refractive index per bar between the fundamental and high-harmonic wavelengths,  $n_2$  is the nonlinear refractive index change due to the high intensity,  $N_a$  is the number of atoms per atmosphere and  $r_e$  is the classical electron radius [46]. The contribution due to the ions is typically a few orders of magnitude smaller and is therefore ignored. In this situation, the contributions from the neutral gas and the free electrons can cancel for a specific ionization fraction. In this situation, phase matching is then independent of the gas pressure.

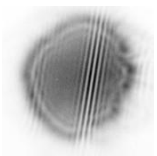
More generally, the geometric phase and dipole phase cannot be ignored. In the common tight-focusing geometry, the geometric phase is given by the Gouy phase. Along the optical axis, it is given by

$$\phi_{Gouy} = - \arctan \frac{z}{z_R}, \quad (2.3)$$

in which  $z$  is the propagation distance relative to the focus and  $z_R$  the Rayleigh range. The Gouy phase is a gradual  $\pi$  phase shift over the focus. It provides a positive contribution to Eq. 2.2 which is not dependent on pressure.

The dipole phase is accumulated by the electron between tunnel ionization and recombination. This depends on the atomic species and the local intensity of the driving laser [44], [47]. The rate of change of the dipole phase over the generation area determines the contribution to Eq. 2.2. It therefore scales with the gradient of the intensity profile.

In all cases, reabsorption of extreme ultraviolet cannot be ignored [48], [49]. Therefore it is important that there is only gas in the region



where it is also possible to achieve phase matching. This can be ensured through differential pumping using a gas cell with small entrance holes for the laser, or the HHG can be driven in a thin gas jet. In the tight-focusing geometry, typically a gas cell or jet is positioned close to the focus of the fundamental beam. Due to the combination of Gouy phase and dipole phase, phase matching is usually achieved when the gas cell is positioned slightly after the focus [47]. Exact phase matching is achieved by tuning the focus position, the gas pressure and the Rayleigh length of the focused beam [50]. The last of these is typically varied using a diaphragm in the fundamental beam close to the lens. A promising alternative solution is based on high-harmonic generation in a gas-filled waveguide [51]. In this case, the geometric phase contribution is determined by the waveguide dispersion. Such waveguides enable tuning of the phase matching, but more importantly, enable a much longer interaction length at higher pressures.

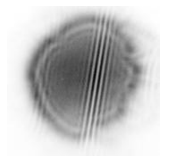
## 2.2 Ultrafast optics

High harmonic generation requires very high intensities on the order of  $10^{14}$  W/cm<sup>2</sup>. In addition, it is necessary that these intensities are achieved before too much ionization has occurred. It is a natural result that ultrafast, femtosecond laser pulses are the best driving pulses for high harmonic generation.

For the work in this thesis, we used 25 fs pulses with a center wavelength near 800 nm. That amounts to pulses of just 10 oscillations of the electric field. The temporal and spectral domain of optical pulses are related by a Fourier transform:

$$A(t)e^{i\omega_0 t} = FT\{\hat{A}(\omega)e^{i\Phi(\omega)}\}, \quad (2.4)$$

in which  $A(t)$  is the temporal envelope of the pulse and  $\omega_0$  the frequency of the underlying carrier-wave. In the spectral domain is determined by the spectral amplitude  $\hat{A}(\omega)$  and the spectral phase  $\Phi(\omega)$ . It follows that pulses that are short in the temporal domain must be broad in the spectral domain and vice versa. It is important to note that the reverse is not true: a broad spectrum can still have a non-trivial spectral phase leading to a long pulse in the temporal domain. The spectrum of our



pulses spans from 730 to 920 nm, with a center wavelength of 810 nm. Assuming an optimal flat spectral phase, this can sustain a 20 fs pulse.

For high-harmonic generation, these pulses must be amplified to the millijoule level while keeping the ultrashort pulse duration. Furthermore, the pulses will be split into a pair of pulses using an interferometer to make two identical HHG sources. In order to still have sufficient energy for HHG, it is therefore necessary to start with pulse energies of 5 to 10 mJ. This chapter provides an introduction on femtosecond pulses, including how femtosecond pulses are generated and amplified, and how the relative phase of the individual spectral components is controlled and optimized.

### Dispersion management

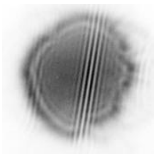
From equation 2.4, it is clear that a controlled spectral phase is a crucial component of femtosecond optical pulses. There are various factors which can influence the spectral phase. The most obvious is perhaps material dispersion, which is the modification of the spectral phase introduced by propagation through that material. The phase introduced by propagation along distance  $x$  is given by  $k(\omega)x$ , where the wavevector  $k$  depends on the radial frequency  $\omega$ , the refractive index  $n(\omega)$  and the speed of light  $c$  according to

$$k(\omega) = \frac{n(\omega)\omega}{c}. \quad (2.5)$$

It is useful to calculate a Taylor expansion of the wavevector around the carrier frequency  $\omega_0$  (see e.g. [52]):

$$\begin{aligned} k(\omega) = & k(\omega_0) + k'(\omega_0)(\omega - \omega_0) + \frac{1}{2}k''(\omega_0)(\omega - \omega_0)^2 \\ & + \frac{1}{6}k'''(\omega_0)(\omega - \omega_0)^3 + \dots \end{aligned} \quad (2.6)$$

In such an expansion, the zeroth order and first order terms are related to the phase velocity of the carrier wave and the group velocity of the pulse respectively. These terms influence the propagation speed of the pulse through materials. They introduce just a phase offset and linear spectral phase dependence, which only shifts the pulse in time, but does not alter the pulse shape.



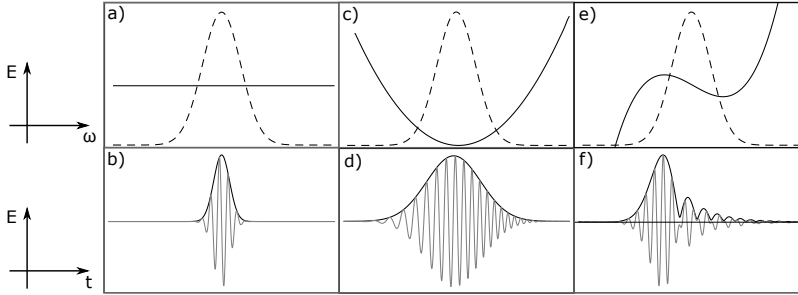
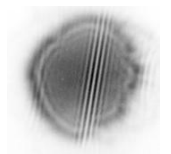


Figure 2.2: Three pulses with identical spectral intensity and different spectral phases. **a** and **b**: Spectral intensity (dashed) and phase of a Fourier transform limited pulse. This corresponds to a short pulse in time. **c** and **d**: A pulse with a quadratic spectral phase chirps the pulse and stretches it. **e** and **f**: A pulse with a third order spectral phase leads to pre- or afterpulses.

The higher order terms of the refractive index do change the pulse shape. The second order term is commonly referred to as *group velocity dispersion (GVD)*, indicating that this term causes different parts of the spectrum to have different group velocities. Group velocity dispersion stretches and chirps the pulse, as displayed in Fig. 2.2b and 2.2e. This means that the frequency of the carrier wave is not constant over the pulse.

The third order term from equation 2.6 is referred to as *third order dispersion (TOD)*. This influences the temporal pulse shape: it stretches and leads to pre- or afterpulses depending on the sign of the TOD. An example of a pulse with TOD is given in Fig. 2.2c and 2.2f. Higher-order terms of dispersion cannot always be ignored. In general, a broader spectrum means that higher-order terms will have to be taken into account.

There are various methods to manipulate the spectral phase apart from introducing dispersive material in the optical path. Gratings and prisms for example introduce angular dispersion. This causes different wavelengths to follow different paths in space. The nonlinearly-varying optical path length as function of wavelength enables the introduction or removal of large amounts of dispersion with a carefully engineered



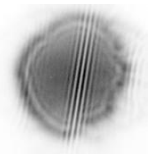
geometry [53], [54]. This will be further discussed in section 2.3. Another possibility is the use of so-called chirped mirrors [55]. These dielectric mirrors consist of a stack of thin layers with varying refractive index and thickness. Effectively, different wavelengths are reflected at nonlinearly different depths in the stack, leading to higher-order dispersion.

### Ultrafast laser systems

To reach higher power femtosecond pulses than oscillators can produce, there are two main paths. One can either try to amplify an ultra-short pulse with an amplifier that keeps the original pulse length as short as possible. Or one can amplify a longer pulse, but use nonlinear techniques to expand the spectral contents of the pulse and use that to compress the pulse to shorter duration. Recently, the second approach has been applied in many commercial systems using hollow core fibers or waveguides for spectral broadening and chirped mirrors to compress the resulting pulse to femtosecond levels [56], [57]. The pulse length reduction methods used in such systems rely on nonlinear optical effects, most notably self phase modulation [58]. Although this nonlinear pulse compression works very well, the intensity during spectral broadening must be limited to avoid the formation of multiple filaments [59]. For higher pulse energies, longer focal lengths and increasingly large setups are therefore required [60], [61]. This limits the usefulness of nonlinear compression at millijoule pulse energies.

In our laser system, we amplify femtosecond pulses from a Ti:sapphire mode locked laser. Titanium-doped sapphire is a commonly used laser gain material for ultrafast laser applications. It has a very large gain bandwidth, spanning from 650 nm to 1100 nm. It can be pumped with wavelengths around 532 nm, which are easily accessible with existing neodymium-doped YAG or vanadate lasers. This enables the generation of femtosecond pulses without the need for nonlinear pulse compression.

A broad gain profile does not mean that the oscillator will automatically operate in pulsed mode. Rather, the pulsed mode should have a larger gain per roundtrip than the continuously operating mode. The optical Kerr effect, where the refractive index changes depending



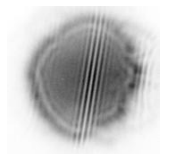
on the incident laser intensity, provides a mechanism to ensure pulsed operation [62], [63]. In the Ti:sapphire crystal, this leads to a self-focusing of the laser beam. Due to their higher intensity, short pulses are focused more strongly in the crystal than a continuous wave. This leads to a better spatial overlap with the pump beam, such that the pulsed mode gets a higher gain than the continuous mode. This is referred to as Kerr lens mode locking [64].

Kerr lens mode locking can sustain few-femtosecond pulses, but it is important that these pulses stay short in the gain medium. If dispersion elsewhere in the cavity stretches the pulses, mode locking cannot be sustained. It is therefore important that dispersion is accurately compensated. To this end, we use broadband chirped mirrors for rough dispersion compensation and a pair of thin glass wedges for fine tuning [55]. Still, the spectrum out of the oscillator is limited by the dispersion compensation and not by the gain bandwidth.

## 2.3 Amplification of femtosecond optical pulses

Out of the oscillator, the pulse energy is a few nanojoules, while the required energy level for HHG is at the millijoule scale. For our experiment, we will need several millijoules, leading to a difference of nearly seven orders of magnitude in pulse energy. In our setup, we use non-collinear optical parametric chirped pulse amplification (NOPCPA) to bridge this gap [65]–[67]. NOPCPA is ideally suited for amplification over ultrawide bandwidths and can achieve very high amplification levels.

In the NOPCPA system, the broadband femtosecond pulses (the *seed*) are overlapped with a high intensity pump pulse in a BBO crystal. Mediated by the high second-order nonlinear susceptibility of the crystal, high energy photons from the pump are converted into pairs of lower energy 'signal' and 'idler' photons. Of the lower energy photons, the signal photon matches the photons from the femtosecond pulses in energy and momentum, while the idler photon carries the excess energy and momentum. This process effectively transfers energy from the pump beam to the seed beam. A schematic overview of the process



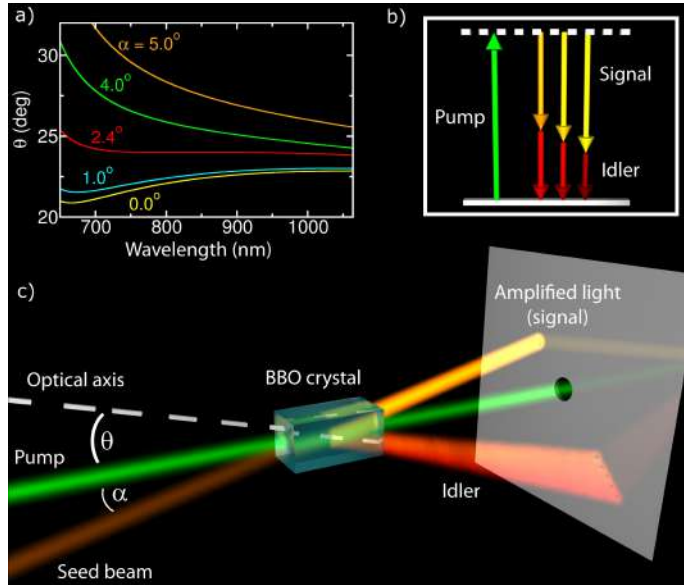
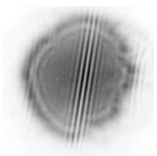


Figure 2.3: Schematic overview of optical parametric amplification, adapted from [65]. A pump and seed beam are combined in a BBO crystal (c), where 532 nm pump photons are converted to signal photons matching the seed photons and idler photons carrying the excess energy and momentum (b). The phase matching depends both on the angle relative to the optical axis and on the angle between pump and seed (a). An angle of  $2.4^\circ$  between the beams allows for an extremely wide phase matching bandwidth.

is given in Fig. 2.3.

Like other nonlinear optical processes, optical parametric amplification is an instantaneous process governed by phase matching. Fig. 2.3a shows the phase matching angle (relative to the optical axis) as a function of wavelength for various angles between the pump and seed beam. From this plot, the advantage of the non-collinear geometry is clear: for the right non-collinear angle  $\alpha$  the phase-matching angle is constant for a wide range of wavelengths, optimal for the amplification of femtosecond pulses.



## Chirped pulse amplification

Optical parametric amplification depends strongly on the pump beam intensity and typically a value around a few  $\text{GW}/\text{cm}^2$  is used. This fixes the pump intensity and limits the intensity of the amplified seed. In order to increase the total energy per pulse, it is possible to use a longer pump pulse with equal intensity. As optical parametric amplification is an instantaneous process, this means that the seed pulse will need to be stretched in duration to match the pump pulse.

In 2018, the Nobel prize in Physics was awarded partly to Gérard Mourou and Donna Strickland for their development of chirped-pulse amplification (CPA). CPA enables such a longer pulse duration for amplification while still yielding short pulses at the end of the line [68], [69]. In CPA, a controlled amount of dispersion is first added to the pulses that are to be amplified. In our system, this stretches the 20 fs pulses to several tens of picoseconds. It also enables the use of picosecond lasers as pump pulses in the NOPCPA [70], [71]. Because the influence of the amplification process on the spectral phase of the seed pulses is limited [72], NOPCPA yields powerful amplified femtosecond pulses after subtraction of the introduced dispersion.

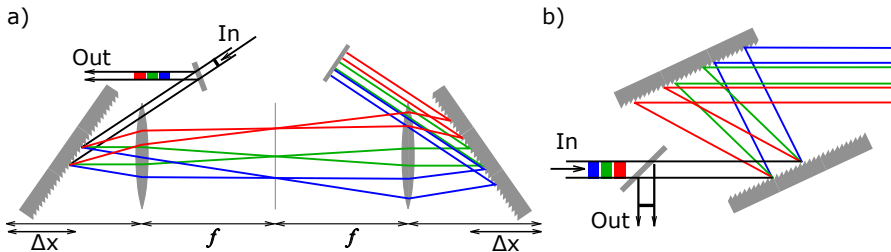
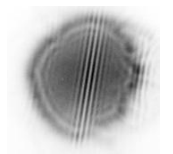


Figure 2.4: Schematic overview of the stretcher (a) and compressor (b). Image adapted from Wikipedia, original by H.K. Nienhuys.

As explained in Section 2.2, there are various methods to introduce dispersion. In our system, we use the combination of a grating-based stretcher and compressor, as shown schematically in Fig. 2.4. In these systems, the light is diffracted by a grating four times: first inducing angular dispersion to spread the wavelengths, then inducing the opposite dispersion to collimate the beam, and finally passing backwards



through the system to fully remove the spatial spread of the spectrum again. In the process, each wavelength sees a different total optical path length. From an analytic calculation of the total optical path [53], [54], [73], it follows that the total group velocity dispersion (GVD) of the stretcher is

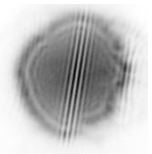
$$\frac{\delta^2\phi}{\delta\omega^2} = \frac{8\pi^2c}{\omega^3d^2} \frac{2\Delta x}{[1 - (\lambda/d - \sin\gamma)^2]^{3/2}}, \quad (2.7)$$

where  $d$  is the grating line spacing and  $\gamma$  the angle of incidence on the grating. The focal length  $f$  and the distance  $\Delta x$  between grating and the focal point are shown in Fig. 2.4. Similarly, the dispersion of the compressor can be calculated to be

$$\frac{\delta^2\phi}{\delta\omega^2} = -\frac{8\pi^2c}{\omega^3d^2} \frac{L}{[1 - (\lambda/d - \sin\gamma)^2]^{3/2}}, \quad (2.8)$$

where  $L$  is the distance between the gratings. Setting  $L$  equal to  $2\Delta x$ , it is clear that the stretcher and compressor induce exactly the opposite dispersion to the input light. Higher order dispersion terms are calculated by taking derivatives from these formulas. For a given set of gratings, the total dispersion is controlled with the alignment parameters  $L$  and  $\gamma$ . All dispersion orders scale linearly with the distance  $L$ , while the angle  $\gamma$  also changes the relative strength of the individual orders.

In general, the presence of dispersive material in the amplifier (such as BBO crystals) will change the spectral phase of the chirped pulses. This not only changes the total amount of GVD and third order dispersion (TOD), but it also changes the relative strength of these contributions. With the compressor it is possible compensate for this additional dispersion. The gratings of the compressor are placed on a rotation stage which rotates around the point of incidence on the first grating. The second grating is placed on a translation stage. This allows for easy adjustment of the angle of incidence as well as the distance between gratings. These two parameters control the GVD-to-TOD ratio and the total dispersion respectively and enable full compensation of these dispersion components [74]. This procedure does lead to a residual fourth order and higher dispersion, which can be important for the shortest pulse lengths (typically below 10 fs).



Grating-based stretchers and compressors are commonly built using gratings operating in reflection, coated with gold or a dielectric to increase reflectivity. Such gratings allow for very high diffraction efficiency when working with blazed gratings at their optimal angle of incidence. Normally, gratings are blazed for Littrow configuration, where the first diffraction order is back-reflected onto the incoming beam. This geometry can be achieved in the stretcher geometry, where the distances between optics are large. A small tilt in the plane perpendicular to diffraction is then used to separate the incoming and outgoing beams.

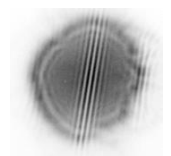
In the compressor geometry, however, the distance between the gratings is typically just a few centimeters. Moreover, the beam size is often increased to stay below the damage threshold for the optics. This means that a Littrow configuration can only be achieved using a design similar to Fig. 2.4a. Compared to the design in Fig. 2.4b, it is significantly harder to optimize the exact pulse compression in this design.

Recently, transmission gratings with high efficiency, broad bandwidth and high damage thresholds have become commercially available. For transmission gratings, the incoming and outgoing beams are automatically separated. It is therefore possible to build a compressor according to the design in Fig. 2.4 where the gratings are placed in Littrow configuration. This enables high throughput efficiency as well as more flexible adjustment of total dispersion.

#### **Typical stretcher and compressor performance**

Initially, our stretcher and compressor were based on gold-coated reflection gratings. To ensure accurate compression of the amplified pulses, the compressor was built in the compact design according to Fig. 2.4. The grating line spacing for the stretcher and compressor were 600 lines per millimeter and 1200 lines per millimeter respectively. This difference in line spacing enabled the stretcher to be built in Littrow configuration. This configuration was used for approximately half of the results presented in this thesis.

Because it was not in Littrow configuration, the total efficiency of our compressor was roughly 40%. This corresponds to a diffraction effi-



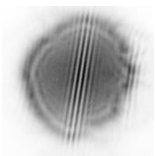
ciency of approximately 80% per grating reflection, while the efficiency of a transmission grating near Littrow configuration can be better than 90% for broad bandwidths. This means that in principle compressor efficiencies in excess of 60% are achievable.

In later experiments, transmission gratings with 1400 lines per mm produced by Lightsmyth were chosen as the starting point for a new compressor design, mainly because of the high diffraction efficiency above 94% over a broad wavelength range. The blazing angle of these gratings is  $34^\circ$ , and the distance between the gratings is set by the need to match the pulse length with the pump pulse in the amplifier. These parameters completely set the dispersion introduced in the compressor, so it is necessary to change the stretcher design to match this dispersion.

The dispersion requirement for the stretcher is given by the sum of the compressor dispersion and dispersion from other sources, such as the BBO crystals in the NOPCPA, several fused silica windows and beamsplitters and approximately ten meters propagation in air. Based on a comparison of several line spacings, the use of gratings with 1400 l/mm identical to those in the compressor was found to be the best option for the stretcher. Due to the large angular dispersion of these gratings, it was not possible to make a design based on curved mirrors, as was the case with the old stretcher. Instead, achromatic doublets optimized for near infrared radiation were used. With a focal length of 10 cm and a diameter of 5 cm, these lenses are 2 cm thick. The dispersion introduced by these lenses was estimated based on the glass thicknesses on the optical axis and included in the total dispersion budget.

### The pump laser

The NOPCPA is pumped using 100 mJ, 80 ps pulses at 532 nm with a 300 Hz repetition rate. The laser system generating these pulses was built by Daniel Noom and a detailed description can be found in Refs [75], [76]. Pulses of roughly 10 picoseconds at 1064 nm are generated at 78 MHz in a Nd:YVO<sub>4</sub> oscillator. A photodiode measuring the output of this laser provides a reference signal at 78 MHz to which the full experiment is synchronized. A delay generator (DG645,



### 2.3. Amplification of femtosecond optical pulses

Stanford Research systems) is used to divide the 78 MHz down to 300 Hz and provide triggers for the various devices in the experiment. The Ti:sapphire oscillator is locked directly to the repetition rate of the Nd:YVO<sub>4</sub> oscillator, enabling time synchronization in the NOPCPA.

There are several stages of amplification between the vanadate oscillator and the NOPCPA. Originally, the first stage of amplification was a regenerative amplifier. In this amplifier, a Pockels cell was used to lock temporarily lock a pulse in a cavity with a continuously pumped gain medium. While the total gain per pass was low, after many passes the regenerative amplifier still yielded roughly 1.5 mJ pulses at 300 Hz. Already a few years ago, it had become clear that the diode-pumped gain module was very old and increasingly unreliable. In addition, the very long beam path and an intracavity intensity near the threshold of nonlinear effects in a regenerative amplifier lead to an increased sensitivity to beam pointing fluctuations. This meant that the regenerative amplifier was a limiting factor for the output stability of the full system.

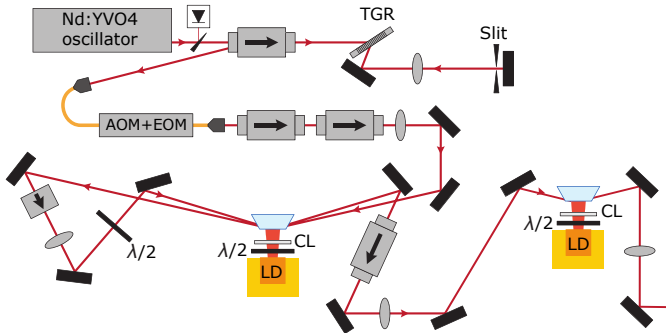
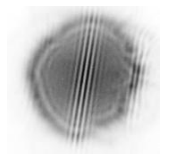


Figure 2.5: Schematic overview of the bounce amplifier including seeding oscillator. The arrows indicate optical isolators. Other components are: TGR: transmission grating,  $\lambda/2$ : half wave plate at 1064 nm, CL: cylindrical lens, LD: laser diode, AOM: acousto-optic modulator (fiber coupled), EOM: electro-optic modulator (fiber coupled)

Recently, a new type of grazing incidence amplifier has been developed by our co-workers [77]. This so-called bounce amplifier can

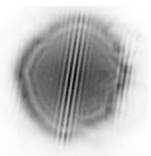


achieve very high single-pass gain and output energies on the millijoule level. This amplifier is well suited to replace the regenerative amplifier and promised a much better stability due to the shorter optical path length. The name *bounce* is derived from a total internal reflection of the laser pulse in the gain medium [78]. In such a geometry, the seed pulse can travel very close to the surface of the gain crystal without loss of beam quality. Furthermore, inhomogeneity of the gain profile perpendicular to the crystal surface is integrated out. Therefore, bounce amplifiers can be pumped at high intensity, leading to very high single pass gain.

A schematic overview of the bounce amplifier is given in Fig. 2.5. Before amplification, there is a stage of spectral clipping and pulse selection. A pulse length of approximately 80 ps is desired to limit the peak intensity in the post-amplifier while the oscillator provides 10 ps pulses. Therefore, the oscillator spectrum is dispersed using a transmission grating, after which a slit is used to reduce the width of the spectrum, effectively stretching the pulses. The slit can be adjusted in width and position, changing pulse length and wavelength respectively. This is optimized for performance in the last amplification stages and in the NOPCPA. After the slit, the light is back-reflected.

The spectrally clipped pulses are rejected by the optical isolator directly between the oscillator and transmission grating, and coupled into a single mode fiber. A combination of a fiber-coupled acousto-optic modulator (AOM) and electro-optic modulator (EOM) is used to select individual pulses at 300 Hz with high contrast. After the EOM, the light is coupled to free space and passes through a pair of optical isolators.

The spectrally clipped 300 Hz pulse train is amplified in three bounce amplifier stages, which are protected from back-reflections by optical isolators. The first two stages use the same gain module, which is equipped with a  $2 \times 4 \times 20 \text{ mm}^3$ , 1 at.-%-doped Nd:YVO<sub>4</sub> crystal. For third pass, a larger  $4 \times 6 \times 20 \text{ mm}^3$  module is used to achieve a larger energy extraction. For each amplification stage, the pulses are loosely focused in the gain module. Both gain modules are pumped to saturation of the population inversion at a wavelength of 880 nm by a bar of pulsed diodes with 140 W output power for 120  $\mu\text{s}$ . The 880 nm diode radiation is collimated with a cylindrical lens and rotated



in polarization by a half-wave plate for optimal performance.

After the bounce amplifier, the pulses are passed through a Pockels cell, a quarter-wave plate, a half-wave plate and an isolator (Fig. 2.6). The Pockels cell is operated in half-wave mode, with 11 kV pulses of roughly 10 ns duration. This assembly separates the pulse from a low, microseconds long pedestal of amplified spontaneous emission. After the isolator, the bounce amplifier delivers 1.3 mJ pulses with a Gaussian beam profile of approximately one millimeter in diameter.

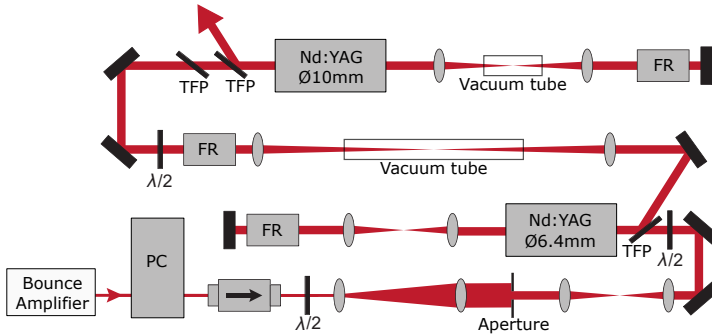
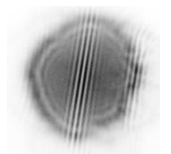


Figure 2.6: Schematic overview of the post amplifier. PC: Pockels cell, FR: Faraday rotator,  $\lambda/2$ : half wave plate, TFP: thin film polarizer.

These pulses will be further amplified in a 'post-amp' (depicted in Fig. 2.6), based on a pair of high-power diode-pumped Nd:YAG amplifiers (REA series by Northrop Grumman) [75]. The gain media in these amplifiers are long circular rods with diameters 6.35 mm and 10 mm, pumped from the side by five arrays of pulsed diode bars. Before the first amplifier module, the seed beam is expanded to a 12 millimeter diameter and passed through a 5 mm aperture. This yields a top-hat beam profile that more efficiently extracts energy from the amplifier modules. In addition, the top-hat profile will lead to a homogeneous gain profile in the NOPCPA.

A top-hat beam profile is not constant with beam propagation. Just a few centimeters after the 5 mm aperture, diffraction rings can be observed which increase in visibility further along the beam. Therefore, a telescope is used to image the aperture to the first gain module. From this point on the pump beam line for the NOPCPA is continuously relay



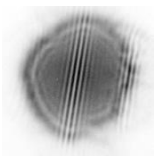
imaged, ensuring good beam quality in the amplification stages. With the exception of the first two relay imaging stages, the intermediate foci are all placed in vacuum tubes to prevent loss of beam quality due to laser breakdown in air.

There is a significant thermal load on the both gain modules in the post amp. The first module with 6.35 mm diameter Nd:YAG rod is pumped at 75 A, 240 V for 240  $\mu$ s, while the 10 mm diameter Nd:YAG rod is pumped at 90 A, 240 V for 270  $\mu$ s. This leads to a small-signal gain of approximately 30 in the first module and 10 in the second module, with a stored energy in the second module of nearly 1 J. While these currents are still well below the specified maximum, significant heat is dissipated in the gain modules. This leads to strong thermally-induced lensing and birefringence in the gain modules. For the first module the thermally induced lens has a focal length of roughly 50 cm. The relay imaging system is therefore set up to compensate for this lensing.

To compensate for thermally-induced birefringence, the modules are double passed [79], [80]. In between the passes, the pulses are relay imaged to a Faraday rotator, which rotates the polarization by 45° irrespective of original polarization. The light is then relay imaged back to the exact same position on the gain module. In this configuration, and with the polarization rotated 90 degrees due to the second pass through the Faraday rotator, the thermal birefringence of the second pass cancels that of the first pass. As the polarization is rotated by 90° relative to the input, a thin-film polarizer can be used to separate the input and output beams.

The spatially-clipped beam into the first module has an energy per pulse of roughly 0.2 mJ. After two passes of the first module, the pulses are amplified to approximately 15 mJ. The second module amplifies this to 150 mJ in two passes. The output of the second module is relay imaged to a BBO crystal for frequency doubling. The resulting 532 nm pulses typically have 100 mJ energy per pulse.

Due to the very high gain of the full post amplifier, a small back reflection can lead to parasitic lasing in the amplifier. As such an event could easily lead to damage, all transmissive optics are tilted with respect to the beam. To prevent significant astigmatism from the tilted lenses, pairs of lenses are always tilted in orthogonal directions.



The lens alignment was optimized using a commercial Shack-Hartmann wavefront sensor. Between the amplifier modules, an optical isolator is incorporated. Finally, to sufficiently reduce back-reflected light out of the second module, a second thin-film polarizer is used.

### Non-collinear optical parametric chirped pulse amplification

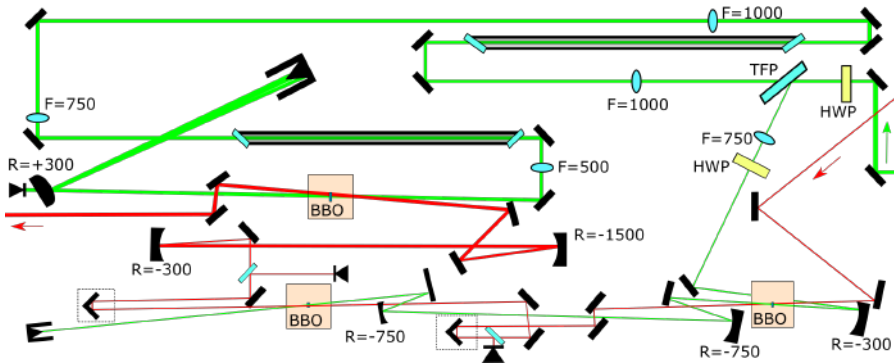
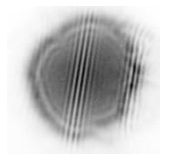


Figure 2.7: Schematic overview of the three-stage NOPCPA amplifier.

In the NOPCPA, the pump beam is split into two components: a 12 mJ beam which is used to pre-amplify the stretched femtosecond laser pulses to the millijoule level, and the remaining 90 mJ which is used to amplify the stretched pulses to maximum power. The power splitting is done using a thin-film polarizer and half-wave plate combination, allowing for easy power adjustment. After the split, the pre-amplifier pump beam is demagnified to a beam diameter of roughly 2 mm using a relay-imaging system.

The pre-amplification is done in two stages with 5x5x5 mm BBO crystals. These crystals are placed in heated holders, with indium foil between the crystal and holder to facilitate a good thermal contact. The crystals are placed on rotation stages to optimize the phase matching angle. The crystal temperature is kept at 40° to avoid crystal degradation due to water absorption.



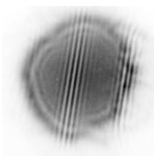
The alignment of all three NOPCPA stages is optimized similarly: a rotation stage is used to optimize the phase matching angle, the infrared beam is aligned with a pair of mirrors to optimize overlap with the pump beam in addition to the non-collinear angle, and the temporal pulse overlap is optimized using a delay stage.



Figure 2.8: Photo of the NOPCPA amplifier in action. The left side of the image shows the first two amplification stages of the NOPCPA, the bright spot in the center shows the final amplification stage and the right part shows the relay imaging system of the pump beam for the final amplification stage.

In the first two NOPCPA stages, the infrared pulses are amplified from a nanojoule per pulse to a approximately a millijoule per pulse. Such high gains are possible due to the optical parametric process: the change in seed intensity is proportional to the intensities of both the pump and the seed beam. This leads to an exponential increase in amplified seed power in the small signal limit [67].

After the second stage, the pre-amplifier pump beam is dumped while the amplified seed is expanded to roughly 8 mm beam diameter. It is then overlapped with the 7 mm main pump beam in the final amplification stage. The BBO crystal in the last stage is 10 by 10 mm wide and 5 mm thick. The typical output power of the final amplification stage is 6 W, at 20 mJ per pulse. A typical amplified spectrum is shown in Fig. 2.9. The amplified seed beam shows a ringlike structure due to a slight inhomogeneity of the pump beam profile.



After the final NOPCPA stage, the amplified beam is spatially filtered using a relay imaging stage with a pinhole at the focus. The pinhole is a 0.2 mm hole drilled in a 5 mm boron nitride disk. It should be noted that the pinhole gradually grows in size with prolonged use. The spatial filter reduces the output power by roughly 10%.

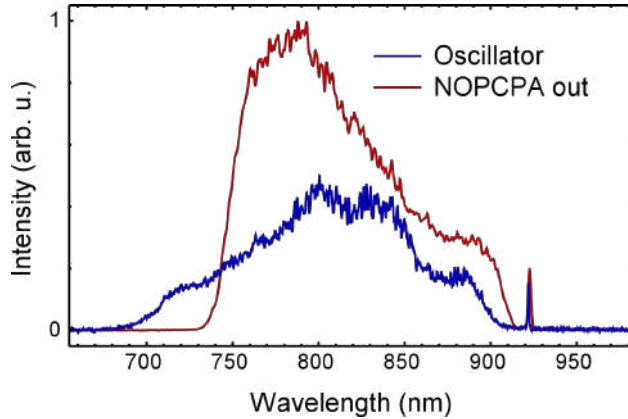
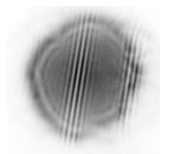


Figure 2.9: Spectra as measured out of the Ti:sapphire oscillator (blue) and out of the amplifier (red).

After the spatial filter, the beam is passed to the pulse compressor. In order to accommodate the large beam, 5 by 5 centimeter gratings are used in the compressor. To optimize the grating efficiency, the polarization is rotated to horizontal using a polarization rotating periscope. Instead of a back reflecting mirror like in Fig. 2.4b, a small retro-reflecting periscope is used at the end of the compressor, vertically separating the output beam from the input beam. Using frequency-resolved optical gating (FROG), the compressed pulses were measured to be near Fourier-transform limited at 25 femtoseconds. The useable output power after compression is typically 10 mJ, which is more than sufficient for our applications.

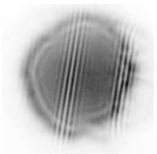
It should be noted that the numbers in this section describe the current state of the NOPCPA, after exchanging the reflective gratings in stretcher and compressor for transmissive gratings and significant work on optimizing the NOPCPA alignment. While the amplified pulse duration has stayed mostly constant during my research project, the



## 2. A TABLE-TOP SOURCE OF COHERENT EUV LIGHT

---

output power has increased over time. This has also led to an increase in extreme ultraviolet flux.



# Interference and diffraction

## 3.1 Waves

In classical optics, light is well described by traveling plane waves. The electric component of a plane wave at a given point in space and time  $(\vec{r}, t)$  may be written as

$$E(\vec{r}, t) = \Re\{Ae^{i(\vec{k}\cdot\vec{r}-\omega t)}\} = A \cos(\vec{k} \cdot \vec{r} - \omega t + \phi), \quad (3.1)$$

where  $A$  is the wave amplitude,  $\vec{k}$  the wave vector indicating the propagation direction,  $\omega$  the angular frequency at which the wave oscillates in time and  $\phi$  a global phase factor. The wave vector and frequency are related to the wavelength  $\lambda$  and the speed of light  $c$  through

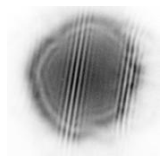
$$|k| = \frac{n\omega}{c} = \frac{2\pi n}{\lambda}, \quad (3.2)$$

where the refractive index of the medium in which the wave travels is given by  $n$ . Unless specifically stated, we will assume that the wave propagates in vacuum, and therefore set  $n$  equal to 1. It is often convenient to write the electric field simply as

$$Ae^{i(\vec{k}\cdot\vec{r}-\omega t)}. \quad (3.3)$$

This simplifies the mathematics, while the electric field amplitude at a given point can always be retrieved by taking the real part.

The electric field is only a component of the full light wave. Light is an electromagnetic wave described by Maxwell's equations [81]. These



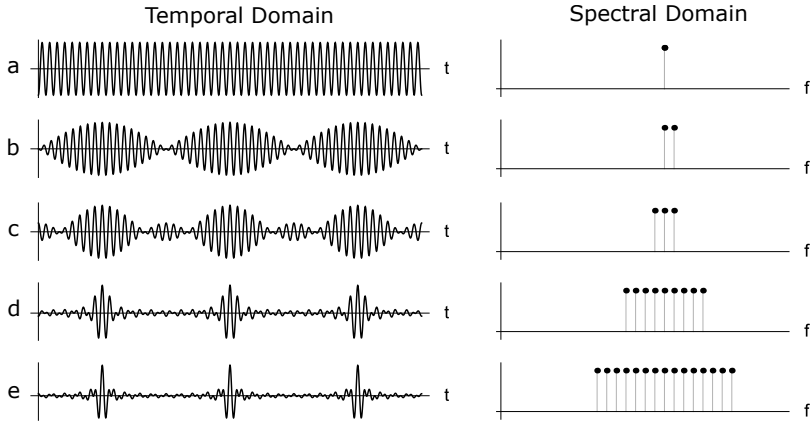


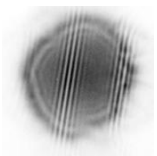
Figure 3.1: Time domain interference of several waves with different frequencies, normalized to the maximum field strength.

equations state that a change in electric field is always accompanied by a magnetic field. The amplitude  $B$  of the magnetic field is given by  $E/c$ . As the magnetic field is much weaker than the electric field and can be directly calculated from the electric field, it is usually ignored in the calculations.

Plane waves can be added together to form more complex light waves. It was already mentioned in section 2.2 that a broad spectrum of waves with different frequency can add up to a short pulse. In Fig. 3.1, it is demonstrated how waves of several different frequencies add up in the time domain.

Just a single frequency component gives a wave of constant amplitude, the base component (Fig. 3.1a). When a second frequency component is added (Fig. 3.1b), these will interfere. In the time domain, this leads to regions of constructive interference where the waves are in phase, increasing the total amplitude and regions of destructive interference where the waves are out of phase, decreasing the total amplitude. For visibility reasons, the increase in amplitude due to the constructive interference is not shown in Fig. 3.1.

In the case of two interfering waves, the interference leads to an oscillating amplitude modulation that is periodic with the difference



in frequency between the two waves. Adding a third frequency component leads to a more complex amplitude modulation. Adding even more frequency components leads to a stronger amplitude modulation forming shorter pulses. In general, a broader spectrum leads to shorter pulses in the time domain.

In the example in Fig. 3.1, the spectral phase was set to zero. This means that there is a point in time where all frequency components are in phase, leading to maximal constructive interference. In reality, there is often a non-trivial phase relation between the frequency components. Such a spectral phase can have dramatic effects on the resulting wave in the time domain. A few examples of common spectral phases distorting the pulse shape are discussed in section 2.2. More extremely, if the spectral phase would be completely scrambled, the wave in the time domain would be similarly random.

Plane waves form a complete set of solutions to the optical wave equation. It is not just possible to combine several waves to a pulse train, rather any waveform can be decomposed in constituent plane waves. This is known as Fourier analysis and performed using the Fourier transform

$$\hat{E}(\omega) = \int E(t)e^{i\omega t} dt \quad (3.4)$$

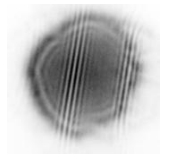
and inverse Fourier transform

$$E(t) = \frac{1}{2\pi} \int \hat{E}(\omega)e^{-i\omega t} d\omega. \quad (3.5)$$

These formulas relate the time-dependent electric field  $E(t)$  and the spectrum  $\hat{E}(\omega)$ . As the plane wave (Eq. 3.3) is a wave both in the temporal and spatial domain, also two-dimensional spatial Fourier transform can be defined as

$$\hat{E}(k_x, k_y) = \iint E(x, y)e^{i(k_x x + k_y y)} dx dy. \quad (3.6)$$

In this definition,  $k_x$  and  $k_y$  correspond to the components of the wave vector  $\vec{k}$  in the  $x$  and  $y$  direction, respectively.



### Fourier transform spectroscopy

Figure 3.1 demonstrates how interference between waves leads to amplitude modulations in the temporal domain. Similarly, plane waves overlapping in space will yield an interference pattern that depends on the propagation directions of the base waves. Interference is in fact a very common phenomenon, only requiring some degree of coherence: there should be a well-defined phase relation between the constituent waves, both in the spatial and spectral domains.

As interference is highly phase-sensitive and results in well measurable intensity modulations, it is a crucial component of many sensitive optical measurements. One such interferometric technique, particularly important for this thesis, is Fourier transform spectroscopy (FTS) [37]. In FTS, the total intensity of two pulses overlapping in time with a controllable delay  $\delta t$  is measured. Since the intensity measurement is very slow compared to the oscillation of the electric field, the measured signal  $S$  is the intensity integrated over time. For two pulses  $E_1$  and  $E_2$ , the signal is

$$S = \int |E_1(t) + E_2(t + \delta t)|^2 dt, \quad (3.7)$$

which can be expanded to

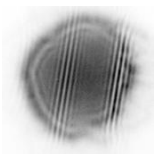
$$S(\delta t) = \int [ |E_1(t)|^2 + |E_2(t + \delta t)|^2 + E_1^*(t)E_2(t + \delta t) + c.c. ] dt. \quad (3.8)$$

The first two terms of this integral yield constants given by the total energy in each pulse. It is instructive to consider two identical simple pulses

$$E_1(t) = E_2(t) = A(t)e^{i\omega_0 t}, \quad (3.9)$$

where  $A(t)$  is the envelope of the pulse and  $\omega_0$  the carrier frequency. The signal then reduces to

$$\begin{aligned} S(\delta t) &= 2\langle A^2 \rangle + \int A(t)A(t + \delta t) \left( e^{i\omega_0 \delta t} + c.c. \right) dt \\ &= 2\langle A^2 \rangle + 2 \cos \omega_0 \delta t \int A(t)A(t + \delta t) dt. \end{aligned} \quad (3.10)$$



In this situation, the signal consists of an oscillation at frequency  $\omega_0$  on top of a constant background given by twice the time-integrated intensity  $\langle A^2 \rangle$  of the individual pulses. The amplitude of the oscillation is given by the autocorrelation of the pulse envelope.

In the more general case of non-identical pulses, the total signal is hard to calculate in the time domain. As the third term of equation 3.8 and its complex conjugate are the convolution of the two electric fields, we can apply the convolution theorem. This theorem states that a convolution in the time domain is a multiplication in the spectral domain. Ignoring the constant terms  $\langle A_1^2 \rangle$  and  $\langle A_2^2 \rangle$ , the Fourier transform of the signal can then be written as

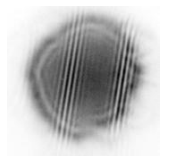
$$\hat{S}(\omega) = \hat{A}_1(\omega)\hat{A}_2(\omega)e^{i(\Phi_2(\omega)-\Phi_1(\omega))} + \hat{A}_1(-\omega)\hat{A}_2(-\omega)e^{i(\Phi_2(-\omega)-\Phi_1(-\omega))}, \quad (3.11)$$

where  $\hat{A}(\omega)$  and  $\Phi(\omega)$  are the spectral amplitude and phase respectively. The negative frequencies at  $-\omega$  follow from the Fourier transform of a conjugated signal.

Equation 3.11 explains clearly why this kind of two-pulse interferometry is referred to as *Fourier transform spectroscopy*. The signal is obtained from an intensity measurement as a function of delay  $\delta t$  using a Fourier transform. If the pulses are identical, or if the spectrum of either one is known, FTS provides a direct measurement of the unknown spectrum. As an additional benefit, the phase difference between the pulses is measured. This makes it possible to measure the full complex spectrum of an unknown pulse using a well-known reference pulse.

## 3.2 Diffraction

In a coherent diffractive imaging experiment, the objective is to reconstruct an image of the object based on the measured diffraction pattern. To achieve this, it is necessary to understand how the light propagates from the object towards the camera. For this, it is instructive to consider an electric field propagating along the  $z$ -axis [82]. Starting from the electric field  $E(x, y, z = 0)$  we will calculate the electric field after a distance  $z$ . The electric field can be written as the Fourier



transform of its angular spectrum  $\hat{E}$ , giving

$$E(x, y, z) = \frac{1}{4\pi^2} \iint \hat{E}(k_x, k_y, z) e^{-i(k_x x + k_y y)} dk_x dk_y. \quad (3.12)$$

The angular spectrum at position  $z$  can be calculated from the angular spectrum at position  $z = 0$  with

$$A(k_x, k_y, z) = A(k_x, k_y, 0) e^{i\Phi(k_x, k_y, z)}, \quad (3.13)$$

where  $\Phi(k_x, k_y, z)$  is the propagation phase  $k_z z$  accumulated by each plane wave component. As

$$|k| = \sqrt{k_x^2 + k_y^2 + k_z^2}, \quad (3.14)$$

this phase can be calculated to be

$$k_z z = |k| z \sqrt{1 - k_x^2/|k|^2 - k_y^2/|k|^2}. \quad (3.15)$$

This yields the general expression

$$E(x, y, z) = \frac{1}{4\pi^2} \iint \hat{E}(k_x, k_y, 0) e^{-i|k|z \sqrt{1 - k_x^2/|k|^2 - k_y^2/|k|^2}} dk_x dk_y \quad (3.16)$$

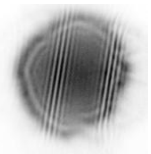
for the electric field after some propagation.

The resolution limit in optical imaging also follows from equation 3.16. If there are very sharp features in the electric field at  $z = 0$ , those features would correspond to high angular frequency components. If it is the case that

$$\sqrt{k_x^2 + k_y^2} > \frac{2\pi}{\lambda} \quad (3.17)$$

the propagation phase becomes imaginary. In this case, these high angular frequency will be suppressed in equation 3.16, and for large enough propagation distance, they are gone completely. The sharpest features in an electric field after propagation are therefore limited by the wavelength, with shorter wavelengths yielding sharper features.

Propagation of the angular spectrum provides a generally applicable method to calculate diffraction of an electromagnetic wave. Two other approximations for electric field propagation are often useful, which are



*Fresnel diffraction* and *Fraunhofer diffraction*. The Fresnel diffraction integral states that

$$E(x, y) = \frac{e^{ikz}}{i\lambda z} \iint E(x', y') e^{i\frac{k}{2z}[(x-x')^2 + (y-y')^2]} dx' dy', \quad (3.18)$$

where  $(x', y')$  are the coordinates in the plane of origin. This result is closely related to the angular spectrum method. It can be shown that these approaches are the same if a first order Taylor expansion of the angular phase factor is made [82]. As this expansion is valid if the angles  $k_x$  and  $k_y$  are small, the Fresnel diffraction integral is a small angle approximation. From the Fresnel diffraction integral, it can be shown that for very large propagation distances, the propagated electric field reduces to a scaled Fourier transform of the original field. This is referred to as *Fraunhofer diffraction*. It is the simplest, most limiting case for electric field propagation. Nevertheless, there are many situations where this approximation is valid.

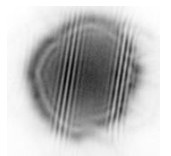
In order to estimate which of these approximations is applicable to calculate the diffraction pattern, the Fresnel number is a useful figure of merit:

$$F = \frac{a^2}{L\lambda}. \quad (3.19)$$

It depends on the characteristic size  $a$  of the object, the distance of propagation  $L$  and the wavelength  $\lambda$ . In order of increasing propagation distance, there are three regimes, given by  $F \gg 1$ ,  $F \approx 1$  and  $F \ll 1$ . For the *near field* situation, the Fresnel number is larger than one, and the angular spectrum method must be used for propagation. In the *far field*, the Fresnel number is much smaller than one and simple Fraunhofer diffraction suffices. The Fresnel diffraction integral is valid in the intermediate and far field regimes.

### Coherent diffractive imaging: phase retrieval methods

In a coherent diffractive imaging experiment (such as shown in Fig. 1.2), a camera is used to directly capture the diffraction pattern arising from a sample [8]. There are no objects in between the sample and the camera, and so the optical propagation can be calculated in a single step. If the electric field at the camera were known, this would directly



enable reconstruction of the light wave emerging from the sample. For sufficiently smooth illumination, this yields an image of the object. However, cameras and photodiodes alike provide a measurement of the field intensity. From this, the electric field amplitude can be calculated, but the phase remains unknown. The diffraction pattern still provides valuable information, and in many cases the phase profile can be reconstructed using iterative phase retrieval techniques [9]. Typically, some degree of additional information is required for successful phase retrieval. For example, a useful additional constraint is that the object is isolated and that it has a finite size [10], [11].

X-ray and extreme ultraviolet coherent diffractive imaging is usually performed in the far field. This means that Fraunhofer diffraction can be assumed, which is relatively fast to calculate by means of a single Fourier transform. The camera measures the angular spectrum of the electric field, with the lowest angular frequency in the center of the camera. The highest measured angular frequency depends on the size of the camera and its distance to the object. Similarly, the size of the object determines the size of the features in the diffraction pattern. These features must be oversampled by the camera in order to enable image reconstruction [12]. That is to say, features in the diffraction pattern should not be smaller than 2x2 pixels of the detector. This can be ensured by placing the camera far enough away or by using a camera with small enough pixels [14], [83].

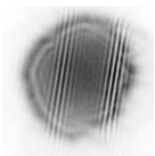
A commonly used phase retrieval algorithm is the *error reduction (ER)* method. This is an alternating projections algorithm in which constraints in the object plane and camera are applied consecutively. A schematic overview of the algorithm is given in Fig. 3.2. Steps 2 and 4 are referred to as the support constraint and the modulus constraint, respectively. These can be written as

$$P_S(E(x, y)) = S(x, y) \cdot E(x, y), \quad (3.20)$$

and

$$P_M(\hat{E}(k_x, k_y)) = \frac{\sqrt{I(k_x, k_y)}}{|\hat{E}(k_x, k_y)|} \hat{E}(k_x, k_y), \quad (3.21)$$

where  $S$  is an intensity mask corresponding to the support and  $I(k_x, k_y)$  the measured diffraction pattern intensity. The  $n^{\text{th}}$  guess of the electric



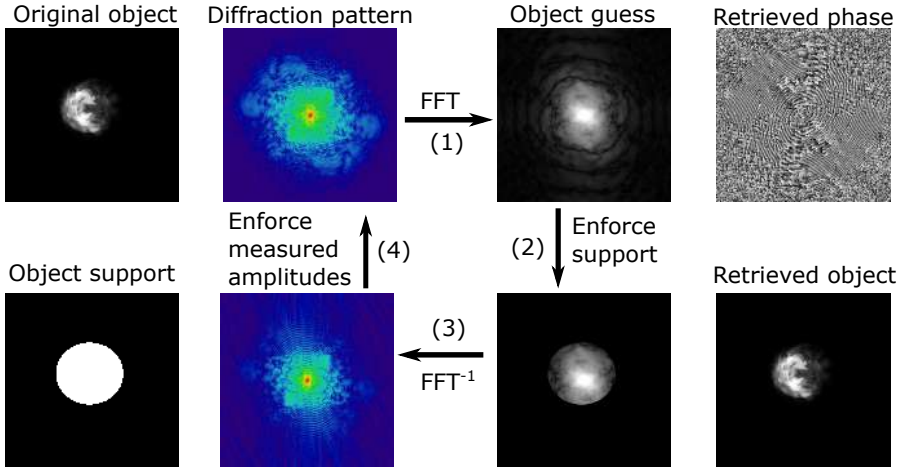


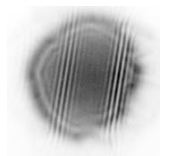
Figure 3.2: Schematic overview of the commonly used error reduction algorithm for phase retrieval. From an original object, a diffraction pattern is measured. A matching object support is determined based on prior knowledge. In the algorithm, a single iteration is given by the following four steps: **1**: a guess of the electric field at the camera is propagated by Fourier transform to the object plane. **2**: the object is matched to the support: all values outside the support are set to zero. **3**: the resulting electric field is propagated back to the camera plane by inverse Fourier transform. **4**: in the camera plane, the electric field amplitude is matched to that of the measurement. With the correct support and a sufficient number of iterations, the phase converges to the correct values and an image of the object is retrieved.

field in error reduction is given by

$$E_{n+1} = P_S(P_M(E_n)), \quad (3.22)$$

where the necessary propagation steps have been left out for compactness.

The accuracy of the phase retrieval process depends strongly on the validity of the support constraint. A good support constraint can be derived from a lower resolution microscopy image of the object. If such a low resolution image is not available, it is also possible to



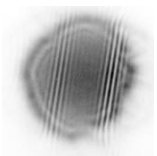
determine the support with a 'shrinkwrap' routine [84]. In this method, an initial support is guessed based on the diffraction pattern. This guess is refined after a number of iterations. Repeating this for several times enables image reconstruction from a diffraction pattern while only assuming that the object has some unknown finite support.

The ER algorithm will converge to a solution, but the accuracy of the solution depends strongly on the quality of the measured diffraction pattern and the chosen support constraint. Especially in situations where the support is not yet optimal, error reduction tends to get stuck in a local minimum, yielding a wrong solution. There are many different phase retrieval algorithms which seek to improve the accuracy and speed of the image reconstruction. An approach which is often used is the hybrid input-output (HIO) algorithm [85]. In HIO, the support constraint is applied as follows:

$$E_{n+1} = S \cdot P_M(E_n) + (1 - S)(E_n - \beta P_M(E_n)), \quad (3.23)$$

in which  $\beta$  is a numerical constant, often chosen to be 0.9. HIO differs from error reduction outside of the support. Here, rather than setting the electric field to zero, the electric field is a linear combination of the new and old guesses of the electric field. This causes the HIO algorithm to be less likely to get stuck in a local minimum [85]. HIO is often used in combination with ER and shrinkwrap. A set of ER iterations adapts the solution quickly to the current support. This is then followed by a set of HIO iterations. From these iterations, it is often possible to determine a better support by thresholding the current guess of the image. This process is then repeated for a few times.

It should be noted that the phase retrieval step in coherent diffractive imaging is a complicated process and it may be difficult to verify the accuracy of the retrieved image. However, there are more extended methods which perform remarkably well. In this respect a particularly promising branch of coherent diffractive imaging is ptychography [86], [87]. In ptychography, many diffraction patterns are recorded by shifting a small illumination probe over a larger sample. While this complicates the measurement setup with respect to standard CDI, there are several advantages to this approach. Because every part



of the sample is illuminated multiple times, image reconstruction in ptychography is particularly robust. Because ptychography enables the reconstruction of probe and object separately, it is better suited to deal with instability in the probe beam and it can handle extended samples [88]–[91].

## Holography

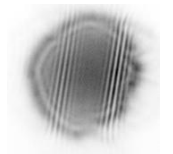
Rather than iteratively reconstructing the phase profile of a diffraction pattern, it is also possible to encode the phase profile into the measured intensity through holography [35]. This phase encoding is done by interfering an unknown electric field with a known reference wave. The result is a characteristic interference pattern which can be analyzed to yield the unknown electric field without the need for iterative phase retrieval.

There are many implementations of holography. Here, I mainly focus on Fourier transform holography (FTH) as this technique can often be applied in the same situations where coherent diffractive imaging is applied [92]–[94]. In FTH, a spherical wave from a spatially separated point source acts as the reference wave. In many cases, the spherical wave emerges from a pinhole in the same mask that also contains the object of interest. A simple example is given in Fig. 3.3a.

A FTH measurement is performed in the far field. The electric field at the sample and at the camera are therefore related by a Fourier transform. The measured diffraction pattern is given by

$$\begin{aligned} I(\vec{k}) &= |\hat{E}_{obj}(\vec{k}) + \hat{E}_{ref}(\vec{k})|^2 \\ &= |\hat{E}_{obj}(\vec{k})|^2 + |\hat{E}_{ref}(\vec{k})|^2 + \hat{E}_{obj}^*(\vec{k})\hat{E}_{ref}(\vec{k}) + \hat{E}_{obj}(\vec{k})\hat{E}_{ref}^*(\vec{k}), \end{aligned} \quad (3.24)$$

in which  $\hat{E}_{obj}$  and  $\hat{E}_{ref}$  are the object and reference wave respectively. This expression contains the cross terms  $\hat{E}_{obj}^*\hat{E}_{ref}$  and  $\hat{E}_{ref}^*\hat{E}_{obj}$ , which encode the phase difference between the two waves. The convolution theorem states that a multiplication in one domain is equivalent to a convolution in the conjugate domain. Therefore, a Fourier transform of the signal  $I(\vec{k})$  yields the convolution  $E_{obj}(\vec{r}) * E_{ref}^*(\vec{r})$ , in addition to its complex conjugate  $E_{obj}^*(\vec{r}) * E_{ref}(\vec{r})$  and the autocorrelations  $E_{obj}(\vec{r}) *$



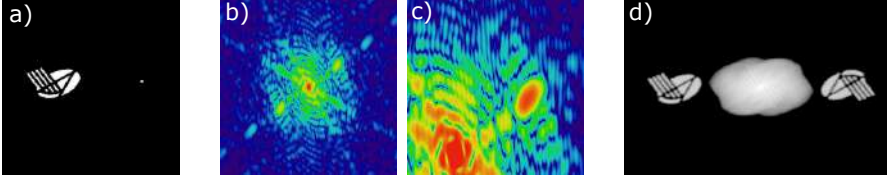
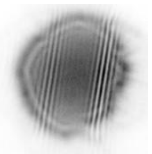


Figure 3.3: Schematic overview of Fourier transform holography. **a:** A typical sample for FTH consists of the object (here the ARCNL logo) and a reference aperture, separated in space. **b:** Far-field diffraction pattern arising from the combined object. **c:** A zoom-in of the diffraction pattern shows fine vertical fringes arising from interference between the object and reference. This encodes the phase of the diffraction pattern. **d:** A Fourier transform of the diffraction pattern yields two identical images of the object as well as the autocorrelation of the object.

$E_{obj}^*(\vec{r})$  and  $E_{ref}(\vec{r}) * E_{ref}^*(\vec{r})$ . In the limit where the reference wave  $E_{ref}(\vec{r})$  is very small compared to the object, it can be approximated by a delta function. The convolutions then yield a direct image of the object wave. An example result of FTH is shown in Fig. 3.3d. The position of the convolution, which is the final image produced in FTH, depends on the separation between the object and the reference structure. For a separations larger than the object size, the image is fully separated from the object autocorrelation.

FTH provides a single-step image reconstruction based on a single intensity measurement, which is beneficial in many situations. As the image is the convolution of the object and reference wave, the resolution in FTH is limited by the reference size. A smaller reference will provide a higher resolution. The signal strength is also directly related to the reference size. The intensity of the reference, and thus of the signal, scales with the area of the reference pinhole. Doubling the resolution by reducing the pinhole size leads to a fourfold reduction in signal strength. This trade-off is an important limitation of FTH which can only partly be circumvented through the use of multiple reference structures [95], [96].



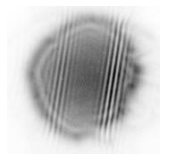
### Monochromaticity as a requirement for CDI

Up until now, we have only considered diffraction of perfectly monochromatic waves. In general, the illumination in a CDI or holography experiment is not fully monochromatic. Because optical propagation depends strongly on wavelength, the full spectrum has to be considered. This can be done by describing the spectrum as a set of mutually incoherent components with different wavelengths. The total intensity after optical propagation is acquired by summing the intensities of the propagated individual components.

In the case of far-field diffraction, the difference in propagation between wavelengths reduces to a simple scaling of the diffraction pattern with the wavelength. This leads to a blurring in the radial direction which increases with scattering angle and width of the spectrum. An extreme example of this is shown in Fig. 3.4. In this example, the relative width of the spectrum  $\Delta\lambda/\lambda$  was larger than  $1/2$ . As a result, all the fine structure of the diffraction pattern is washed out. Accurate phase retrieval from such a diffraction pattern will be extremely difficult, if not impossible. For less extreme bandwidths, it has been demonstrated that the radial blurring can be incorporated into the phase retrieval model if the illumination spectrum is known [15].

The situation where  $\Delta\lambda/\lambda$  is very large is especially relevant for high harmonic generation-driven CDI. HHG typically produces harmonics spanning an extremely wide spectral range. Fig. 3.4 illustrates how a similarly broad spectrum can influence the measured diffraction pattern. It is clear that the HHG spectrum must be monochromatized before a CDI experiment can be performed.

There are various approaches to spectral filtering in the extreme ultraviolet domain. For example, a diffraction grating can be used to spatially disperse the individual wavelengths (see, for example, [97]). After the grating a simple slit can then be used to select the desired wavelength. Another commonly used approach is the use of multilayer-coated mirrors. Such mirrors can have high reflectivity over a narrow bandwidth, and allow for easy-to-align spectral filtering without changing the beam profile. In addition, these mirrors can be produced with a finite curvature such that the beam is focused on the sample.



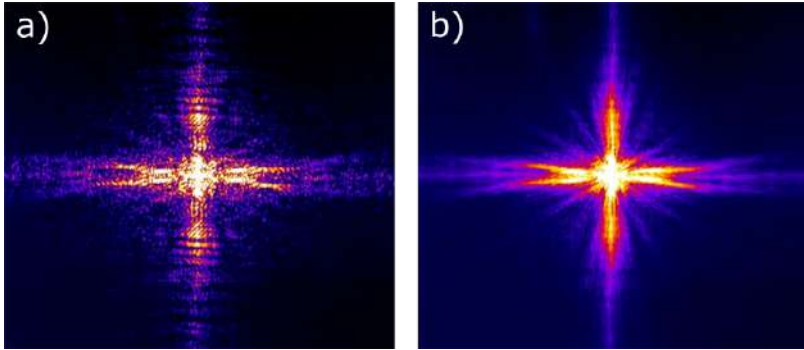
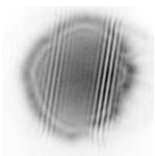


Figure 3.4: **a**: Diffraction pattern from monochromatic light, obtained with a Ti:sapphire laser operating in narrow-band continuous wave mode. **b**: Diffraction pattern from broadband light, obtained with the same Ti:Sapphire laser operating in pulsed mode. The sample used was a USAF resolution target.

It is important to consider the acceptable bandwidth after spectral filtering. This is determined by the expected level of radial blurring, which can be calculated based on the object size, distance to the camera and the camera pixel size [29]. This calculation then yields the requirements for the spectral filtering procedure.

When using high harmonics, the requirements on the monochromator can often be relaxed. This is because HHG can generate a 'comb' of narrow-band high harmonics. The spectral range covered by the full comb is determined by phase matching properties and can be very large, but the individual high harmonics may have a very narrow bandwidth. This is related to the pulse length of the driver pulse in combination with the phase matching conditions. If these properties combine in such a way that efficient high harmonics are generated over an extended time window, very narrow high harmonics can be produced. Such a situation is beneficial, because the spectral filtering can then be optimized for power throughput while ensuring that the filtering is just strong enough to transmit a single harmonic.

Spectral filtering of HHG sources provides suitable source parameters for coherent diffractive imaging experiments, and has led to sev-



eral groundbreaking results in EUV microscopy [24], [25], [97], [98]. Nevertheless, the resulting images are always monochromatic as a consequence of the monochromaticity requirement in CDI. It would be beneficial to extend CDI with spectral resolution. This is possible by sequentially measuring at different wavelengths, but for HHG sources this means exchanging mirrors or adjustment of a grating-based monochromator. The low throughput of typical monochromator solutions and the high sensitivity of CDI to alignment mean that this would be a difficult and time-consuming experiment.

The goal in the following chapters is to demonstrate coherent diffractive imaging with spectral resolution using the full bandwidth of HHG sources. High harmonics are especially promising for spectroscopic imaging applications because of their high spatial coherence in combination with a broad EUV spectrum. In order to resolve the contributions of individual wavelengths, we will employ Fourier transform spectroscopy with HHG sources. How this can be done is described in the next chapter.





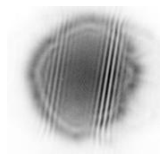
# Spatially Resolved Fourier Transform Spectroscopy in the Extreme Ultraviolet

## Abstract

Coherent extreme ultraviolet (XUV) radiation produced by tabletop high-harmonic generation (HHG) sources provides a wealth of possibilities in research areas ranging from attosecond physics to high resolution coherent diffractive imaging. However, it remains challenging to fully exploit the coherence of such sources for interferometry and Fourier transform spectroscopy (FTS). This is due to the need for a measurement system that is stable at the level of a wavelength fraction, yet allowing a controlled scanning of time delays. Here we demonstrate XUV interferometry and FTS in the 17-55 nm wavelength range using an ultrastable common-path interferometer suitable for high-intensity laser pulses that drive the HHG process. This approach enables the generation of fully coherent XUV pulse pairs with sub-attosecond timing variation, tunable time delay and a clean Gaussian spatial mode profile. We demonstrate the capabilities of our XUV interferometer by performing spatially resolved FTS on a thin film composed of titanium and silicon nitride.

---

This chapter is based on: G. S. M. Jansen, D. Rudolf, L. Freisem, K. S. E. Eikema and S. Witte, *Spatially Resolved Fourier Transform Spectroscopy in the Extreme Ultraviolet*, *Optica* **3**(10), 1122-1125(2016).

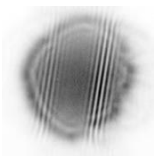


## 4.1 Introduction

A well-known feature of high-harmonic generation (HHG) is broadband spectra in the XUV and soft X-ray regions [39], [99], [100]. This radiation is typically emitted in a train of attosecond pulses with excellent spatial and temporal coherence, as shown in various interferometric and spectroscopic measurements [20], [21], [101]–[107]. As a result, interferometry with high harmonics found important applications in e.g. Molecular Orbital Tomography [108], in wavefront reconstruction [109] and electric field characterization [110] of high harmonics.

Recently, interferometry with high harmonics provided added value to coherent diffractive imaging (CDI) [107], [111] using the full high harmonics bandwidth and photon flux. However, in the extreme ultraviolet (XUV) spectral range, interferometry and Fourier transform spectroscopy (FTS) are challenging due to the high stability requirements of the interferometer itself. Two main types of HHG interferometers have been devised. In one scheme, the near-infrared fundamental driving pulse is split into two phase-locked pulses with an adjustable time delay, and this pulse pair is subsequently used for HHG [21], [102]–[104]. Although this method has been successfully used it is typically limited by the stability of the optical interferometer. The other scheme is based on wavefront division, whereby one HHG beam is divided into two phase-locked sources by a piezo-mounted split mirror. This configuration allows more stable interferometry [105], [112]–[115], but results in two beams with different spatial profiles and strong diffraction effects due to the hard edge of the split mirror. Wavefront division interferometry is also less flexible when one would like to change the intensity ratio between the two beams.

In this chapter we present XUV interferometry using a novel ultra-stable common-path interferometer with a timing stability better than 0.8 attoseconds (as) between two phase-locked high-harmonic sources. We characterize high-harmonic spectra from argon and neon, and perform Fourier transform spectroscopy on a thin titanium/silicon nitride bilayer. Our approach combines the flexibility of near infrared (NIR) interferometers with the stability of common-path techniques. Because no XUV optics are involved the only bandwidth limitation is the phase-matching bandwidth of the HHG process, which can span



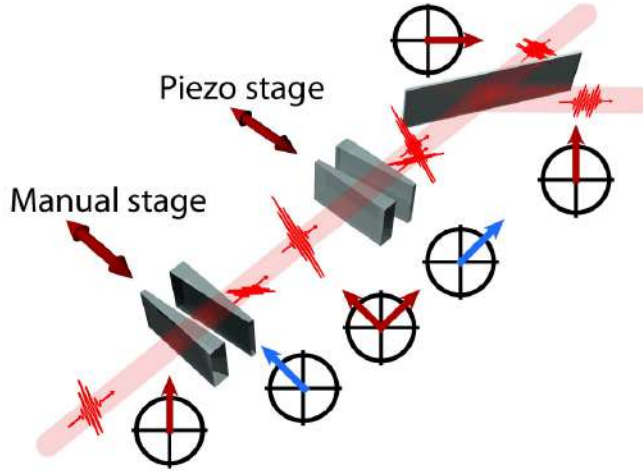
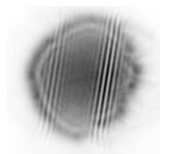


Figure 4.1: Schematic overview of the common-path, birefringent wedge-based interferometer. The polarization diagrams depict the polarization (in red) at various positions in the interferometer. The fast axes of the birefringent wedges are indicated using blue arrows. A manual translation stage is used to control the total optical path length through the first wedge pair, while a piezo-driven stage controls the position of the second pair.

more than an octave [100].

## 4.2 Experimental setup

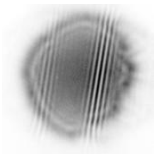
In our experiments we use a Ti:Sapphire-seeded noncollinear optical parametric chirped-pulse amplifier (NOPCPA) [65]. The pump laser for this system delivers 80 mJ, 532 nm pulses with a duration of 64 ps at 300 Hz [75]. The output of the NOPCPA is compressed to pulses of approximately 20 fs duration and an energy of 5 mJ. These pulses are then directed into our common-path interferometer, which is schematically displayed in Fig. 4.1. The phase-locked pulse pair is produced in birefringent wedges, where the optical axis is oriented at  $45^\circ$  with respect to the input polarization [116], [117]. This pair of wedges splits the input pulse into two parts of equal intensity but with



orthogonal polarization, and introduces a delay of several picoseconds between the two electric field components. The second pair of wedges has its optical axis perpendicular to the first pair, thus providing an opposite delay compared to the first pair of wedges. The exact remaining delay can be controlled by moving one of the wedges perpendicular to the beam. The final delay depends linearly on the wedge displacement and can be tuned with sub-attosecond resolution. Behind the second pair of wedges we use an ultrabroadband thin-film polarizer to project the pulses onto the same polarization axis. The resulting pulse pair is vertically polarized and contains up to 1 mJ per pulse. The intensity ratio between the beams can be controlled by tuning the input polarization state with a half-wave plate.

Behind the interferometer, the pulses are focused into a gas jet for HHG, as shown in Fig. 4.2(a). By tilting the last wedge of the interferometer, we ensure that the focal spots of the two pulses are separated by  $280\ \mu\text{m}$  in the focal plane, which is several times the focused beam diameter ( $60\ \mu\text{m}$   $1/e^2$ -diameter). This separation ensures that the two pulses generate high harmonics independently, as any partial overlap could lead to delay-dependent interference effects between the pulses, which in turn would affect ionization and phase matching. Even for this large separation, however, the remaining field strength between the beams still leads to small modulations of the interferogram at the fundamental frequency.

Behind the HHG chamber we use an aluminum filter in combination with a 1 mm diameter aperture to separate the XUV from the driving NIR radiation. The XUV beams overlap and interfere in the far field, where we use an XUV-sensitive CCD camera (Andor iKon-L) to record the interference patterns. Examples of the measured interference patterns are given in Figs. 4.2(b,c). The beams interfere at an apex angle of 0.4 mrad, leading to multiple zones of straight fringes with a high visibility. The spatial mode profile of the individual HHG beams has a smooth Gaussian shape. Some slight diffraction features can be observed at the edges caused by the aperture in the beam path. For more details about the interferometer and HHG see the supplementary information in Section 4.6.



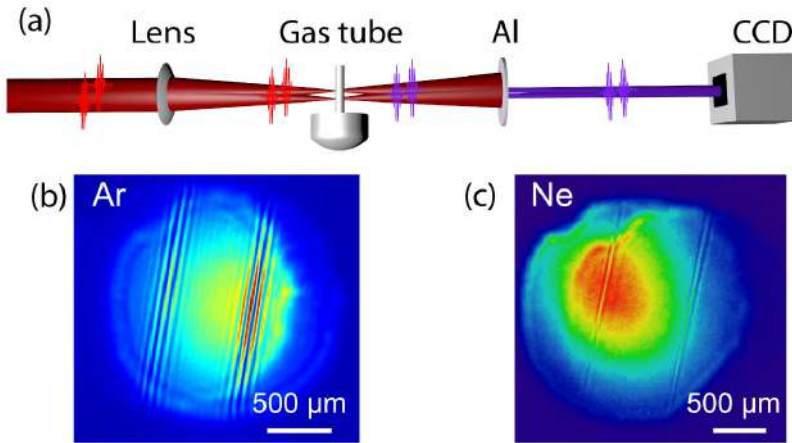
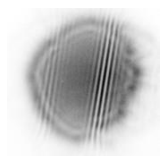


Figure 4.2: **a**: Schematic overview of the setup for high-harmonic generation. A lens ( $f = 25$  cm) focuses the input pulses in the gas jet. A thin tube (inner diameter 1.4 mm) is used to guide the gas from a pulsed nozzle to the interaction region 8 mm behind the nozzle. A 1 mm aperture (not shown) blocks the near-infrared light just before the aluminum film (Al), while transmitting the high harmonics. **b**, **c**: Spatial interference patterns for high harmonics generated in argon and neon, respectively. A movie displaying the full time-delay scan from which **b** can be found online in the supplementary information to the original paper. A part of this delay scan is reproduced as a flip book in this thesis in the bottom left and right corners of the page.

## 4.3 Extreme ultraviolet interference: results and analysis

### Spatial interference

A *spatial* Fourier transform of an interference pattern at a fixed delay directly yields an HHG spectrum [118], as shown in the inset in Fig. 4.3(a), which is possible because of the near-diffraction-limited beam profile of the individual HHG beams. Although this spectrum is limited in resolution due to the small angle, the individual harmonics are still clearly resolved. This spatial transform is useful as a single-

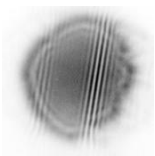


shot diagnostic of the high harmonics spectrum. A further advantage is that these individual harmonic peaks contain information on the delay between the pulses. The change in delay between two images can be calibrated from these measurements by evaluating the phase delay of the individual harmonic peaks as a function of time delay.

The extracted phase for a single harmonic vs. stage position is shown in Fig. 4.3(a), and confirms the scan linearity of our interferometer. In addition, the intensity of the particularly selected harmonic extracted from the interferogram is also plotted. By calculating the phase delay per stage step and dividing by the central angular frequency of the harmonic, we obtain the time delay per step (Fig. 4.3(b)), as well as a measurement of the interferometer stability. Analyzing the data for the high-amplitude range of the scan between  $60\ \mu\text{m}$  and  $95\ \mu\text{m}$ , we find an upper limit to the timing stability of 0.8 attoseconds (standard deviation) or, equivalently, 0.25 nm optical path length stability (Fig. 4.3(c)), with a measurement accuracy limited by the precision of the phase determination in the spatial Fourier transform. It is worth noting that this upper limit includes the effects of possible differential phase shifts between the two separated HHG zones. Small intensity variations could in principle lead to phase shifts between the harmonic beams if the driving pulses are not identical [21], but the present measurement shows that this effect does not limit the applicability of HHG-based FTS for the current spectral range. With the achieved stability, simulations show that FTS is feasible even at wavelengths well below 10 nm [111].

### Temporal interference

By scanning the time delay between the pulses, an accurate measurement of the HHG spectrum can be obtained using FTS. We recorded such Fourier scans of high harmonics generated in argon and neon. In FTS, the step size should be less than half of the shortest wavelength in the source spectrum, and the obtained spectral resolution is determined by the length of the scan. We typically record up to a thousand images with a step size of 15 as. To remove the influence of intensity fluctuations in the recorded interference patterns (caused by laser power or beam pointing variations) and subsequently improve the



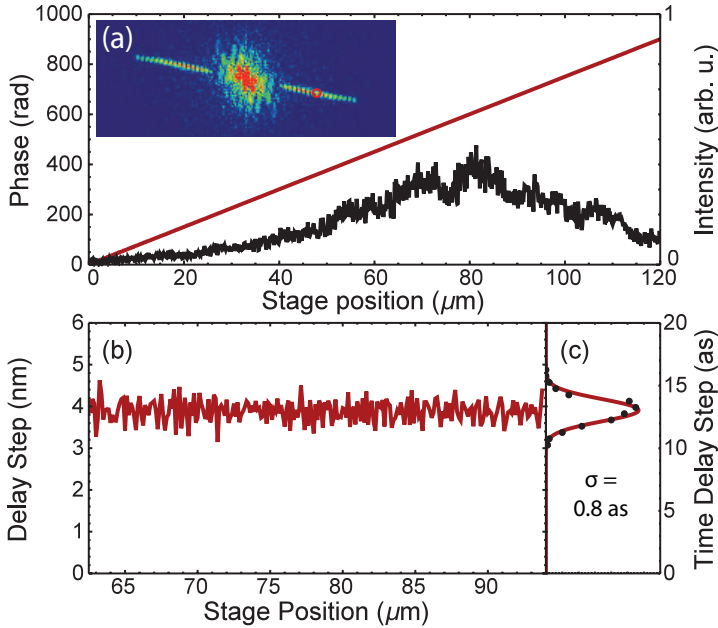
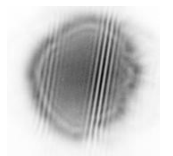


Figure 4.3: **a:** Inset: spatial Fourier transform of the interference pattern of HHG in neon (enlarged version in Fig. 4.6). Phase (red) and amplitude (black) of the 33<sup>rd</sup> harmonic (red circle in the inset) as a function of piezo stage position. **b:** Consecutive step sizes retrieved from the measured phase. **c:** Step size distribution averaged over all harmonics has a standard deviation of 0.25 nm or 0.8 as.

signal-to-noise ratio, we normalized the spatial interference patterns to a selected local area in the beam.

Finally, a spectrum for every pixel is acquired by Fourier transforming the measured data along the time axis. Fig. 4.4 shows temporal interferograms for single pixels and the corresponding HHG spectra. As the interference pattern will only show those spectral components that are present in both beams, both driving pulses should produce identical HHG spectra, which has been confirmed using a grazing-incidence grating XUV spectrometer. The interferograms in Figs. 4.4(a,b) and Figs. 4.4(d,e) contain two clear timescales, corresponding to the auto-correlation widths of the individual attosecond pulses and the coher-



#### 4. SPATIALLY RESOLVED FOURIER TRANSFORM SPECTROSCOPY

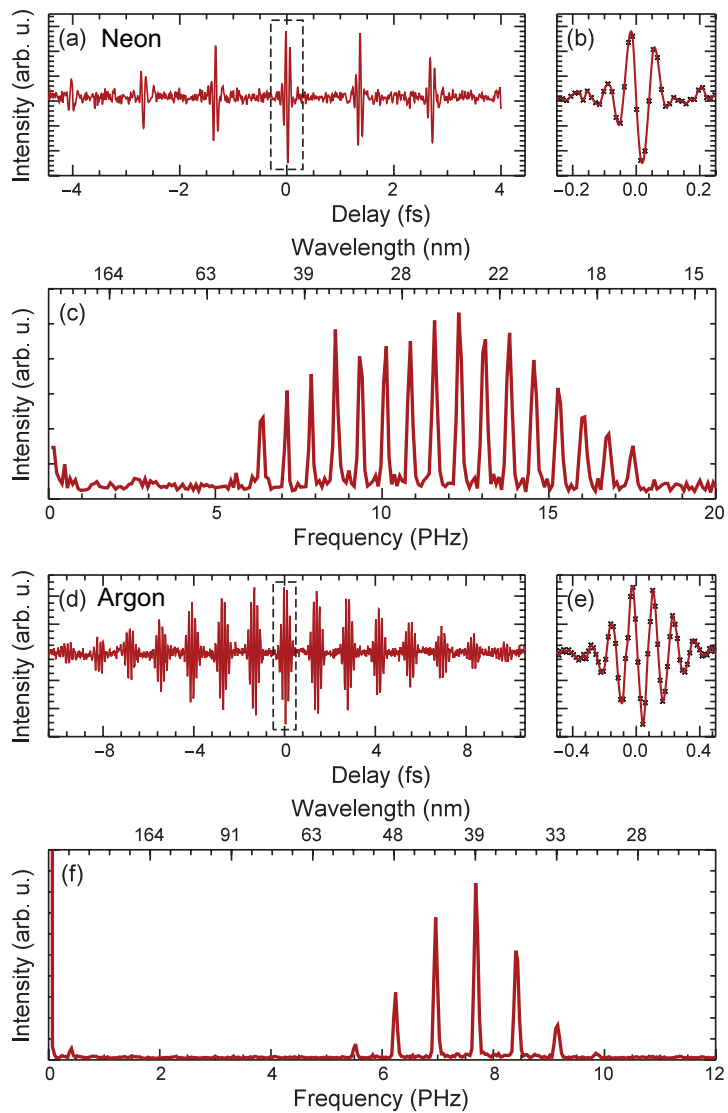
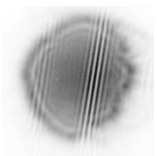


Figure 4.4: Interferograms from a single pixel for high harmonics produced in neon (a) and argon (d) with a magnified view of the central part (b,e). A Fourier transform of the interferograms yields the neon (c) and argon (f) spectra.



ence time of the attosecond pulse train, respectively.

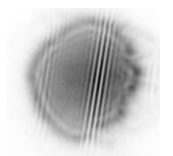
For the autocorrelation widths, we obtain  $(396 \pm 10)$  as (Ar) and  $(115 \pm 6)$  as (Ne), which reflects the about 3.5 times broader spectrum of HHG from Ne compared to Ar. On the other hand, the coherence times are  $(11.9 \pm 0.3)$  fs (Ar) and  $(6.0 \pm 0.6)$  fs (Ne) indicating that high harmonics in Ne are produced by the most intense temporal part of the laser pulse. The measured autocorrelation width for Ne is slightly increased by the limited transmission spectrum of the Al filter.s

In contrast to a grating spectrometer, the frequency resolution in FTS is constant over the full spectrum, which amounts to 80 THz for the example shown in Fig. 4.4(c). Expressed as a fraction of the wavelength, this means a resolution of 1 in 200 for the highest harmonic orders versus 1 in 100 for the longer wavelengths. In our current interferometer we can scan up to 50 fs in time delay, which corresponds to a potential resolution of 1 in 900 for the highest harmonic orders. This scan range can easily be extended by increasing the travel range of the piezo stage and the size of the wedges. This flexibility of the spectral range and resolution are clear advantages of FTS as a spectroscopic technique.

## 4.4 Spatially resolved spectroscopy

In addition to the spectral and spatial characterization of the HHG beam itself, our method can also be applied to perform spectroscopy on spatially complex samples. We explore this option by measuring the transmission spectrum of a 20 nm thin titanium film grown by electron beam evaporation on a 15 nm thin silicon nitride membrane. The membrane contains a 100  $\mu\text{m}$  diameter aperture near one side (Fig. 4.5(a)). With spatially resolved FTS we can simultaneously measure the XUV spectrum transmitted through the bilayer and through the aperture, a measurement that would be challenging to perform with grating-based spectrometers. We used the spectrum transmitted through the aperture as a reference for a direct determination of the relative absorption spectrum of the bilayer.

The titanium sample was positioned in the XUV beam ensuring that both XUV pulses were overlapping on the sample. A typical trans-



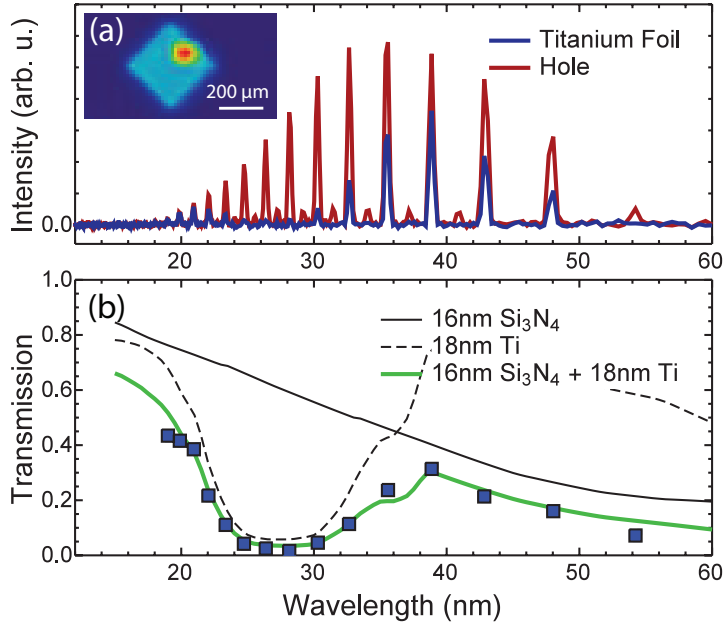
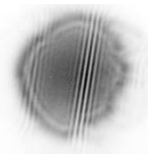


Figure 4.5: Spatially dependent spectrum of a thin titanium/silicon nitride bilayer with an aperture. **a:** Retrieved spectra for both the aperture and the bilayer from a single Fourier scan. In the bilayer spectrum the Ti absorption band is clearly visible. The inset shows a transmission image of the bilayer with the hole at the top right side. **b:** The spectral transmission of the bilayer (blue squares) matches with the expected transmission of 18 nm Ti on 16 nm silicon nitride [119].

mission spectrum is given in Fig. 4.5(a). A single Fourier scan yields spectra for the transmission of both the aperture and the titanium thin film (Fig. 4.5(b)). The spectrum transmitted by the bilayer shows a clear dip around 25 nm matching with the corresponding absorption band of titanium. Comparing the strength of the harmonics in both spectra yields the spectral transmission of the combined titanium and silicon nitride layer, as shown in Fig. 4.5(b). The measured transmission matches with the expected transmission of an 18 nm titanium layer on top of a 16 nm layer of silicon nitride [119]. Potentially, there could be a thin titanium oxide layer on top of the titanium film, but



given the small difference in XUV absorption this distinction cannot be made.

## 4.5 Conclusion

In summary, we have demonstrated XUV interferometry and Fourier transform spectroscopy without the need for XUV optics. Using a birefringence-based common-path interferometer, we achieve sub-atto-second timing stability and a high spectral resolution. With two HHG pulses from neon gas, we measure more than octave-spanning spectra down to 17 nm wavelength and find that the HHG process adds less than 0.8 as relative timing jitter under our experimental conditions. We demonstrate that our FTS method can be used to measure the absorption spectrum of a spatially inhomogeneous thin film sample. For future experiments it is particularly promising to combine this method with CDI on nanostructures composed of multiple materials.

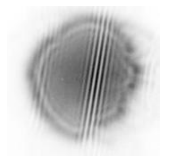
## 4.6 Supplementary material

### Birefringent wedge-based interferometer

In the interferometer, a piezo linear stage (Physik Instrumente GmbH, model number P-625.1CD) is used to displace one of the birefringent wedges. The stage has a travel range of 500  $\mu\text{m}$ , a resolution of 1.4 nm and a repeatability of approximately 5 nm.

The final delay introduced by the wedge-based interferometer depends linearly on the wedge displacement  $\Delta x$  and is given by  $\Delta t = (\Delta n \Delta x / c) \tan \varphi$ , where  $\Delta n = n_e - n_o$  is the difference in refractive index for the extraordinary and ordinary polarization states,  $c$  is the speed of light in vacuum and  $\varphi = 15^\circ$  is the apex angle of the wedges. We use  $\alpha$ -BBO crystals in the interferometer because of their strong birefringence ( $\Delta n = 0.11$  at 800 nm) and low nonlinear susceptibility. Behind the second pair of wedges we use an ultrabroadband thin-film polarizer to project the pulses onto the same polarization axis.

The apex angle of the birefringent wedges was chosen to be 15 degrees, leading to a full scan range of 50 fs. Based on the speci-



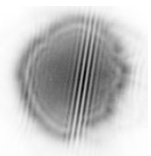
fications of the piezo stage and the refractive indices of  $\alpha$ -BBO, the resolution and repeatability of the interferometer are 0.14 as and 0.5 as, respectively. The  $\alpha$ -BBO wedges are mounted using KM100CL rectangular mounts (Thorlabs) at a height of 8 centimeters above the baseplate. This baseplate is bolted directly to the optical table. Care was taken to keep the optical components on low and stable posts to minimize potential vibrations.

To minimize vibrations caused by the vacuum system influencing the HHG we employ low-vibration turbomolecular pumps (Pfeiffer HiPace 700), while the scroll pump (Edwards XDS10) used for backing the turbos is connected using flexible bellows wrapped in vibration-damping foam.

### High-harmonic generation geometry

Behind the interferometer, a lens ( $f = 25$  cm) focuses the pulses into a gas jet for high-harmonic generation. The gas is supplied by a pulsed piezo valve (developed by M.H.M. Janssen, Vrije Universiteit Amsterdam) and guided through a thin tube towards the interaction region with near-infrared pulses. To ensure that both near-infrared pulses generate XUV independently, we separate the foci by  $280 \mu\text{m}$ . In the chosen geometry this means that one pulse is focused slightly closer to the gas nozzle than the other pulse. We focus the pulse pair into the gas jet at a fairly large distance of about 8 mm with respect to the nozzle. Simulations of supersonic gas expansion show that the pressure difference between the two focal spots at this nozzle distance is sufficiently small to ensure similar phase matching conditions between the two beams. In addition, for gas confinement we use a thin stainless steel tube with an inner diameter of 1.4 mm to guide the gas from the nozzle to the interaction region. The near-infrared laser pulses are focused through a 0.5 mm aperture drilled perpendicular to the tube axis.

To confirm that the phase matching conditions are similar for both pulses, we used a grazing incidence XUV grating spectrometer to measure the HHG spectrum of the individual pulses. The XUV spectrometer, equipped with a 600 lines/mm grating, is designed for a spectral range between 5 nm and 40 nm and was operated at a resolution



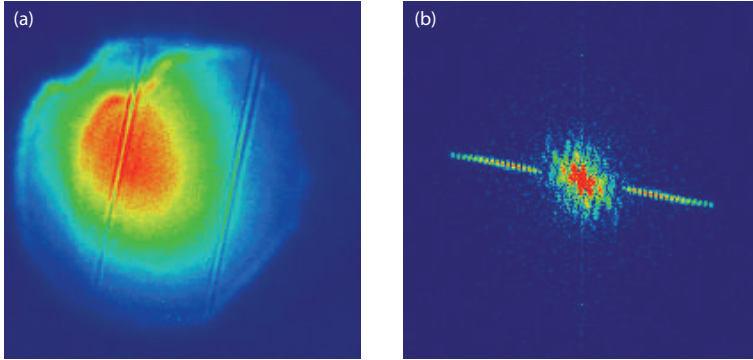


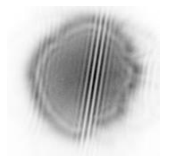
Figure 4.6: **a:** Typical spatial interference pattern as recorded for a fixed time delay using high harmonics generated in Neon gas. **b:** Amplitude of the two-dimensional Fourier transform of the example interference pattern in (a).

of  $\lambda/\Delta\lambda = 250$  at 20 nm wavelength. As for single high harmonic beams, we observed the spectra to be identical. Furthermore, the HHG spectrum observed for both simultaneously present beams did not change, confirming that the pulses did not influence each other significantly.

While the chosen geometry worked well and was experimentally convenient to realize, a geometry where the two pulses are displaced orthogonally with respect to the gas jet direction can potentially lead to slightly better phase matching conditions. Such a geometry, however, does require precise knowledge of the transverse pressure profile in the gas jet, and a sufficiently wide jet compared to the focal spot separation.

### Single-shot Fourier Transform interferometry

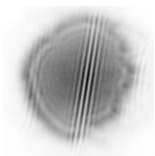
The generated XUV beams overlap with an apex angle of approximately 0.4 milliradians. Therefore, for each harmonic a fringe pattern in close analogy to the Young's double slit experiment is formed. The period of these fringe patterns is proportional to the wavelength of the respective harmonic, while the phase of the fringe is determined by the



delay between the two pulses. The fringe patterns for all harmonics then add up coherently to form the interference pattern as measured on the camera. In Fig. 4.6(a), the plane spanned by the k-vectors of the two beams (interference plane) is rotated with respect to the horizontal plane, which results in a slightly tilted interference pattern with respect to the vertical axis of the camera image.

The raw camera images can be decomposed into the contributions of the individual harmonics by a two-dimensional Fourier transform of the raw image. For a fixed angle between the beams, every harmonic wavelength corresponds to a specific spatial frequency in the Fourier transform image. Therefore, the individual harmonics appear spatially separated in the Fourier transform data. The center of the image corresponds to zero spatial frequency, and increasing spatial frequencies are positioned radially outward. This yields a set of peaks corresponding to the individual harmonics lying on a line perpendicular to the original fringe direction, as shown in Fig. 4.6(b). The phase of the individual peaks in this spectrum directly yields the phase of the corresponding monochromatic fringe pattern.

Due to the symmetry of the Fourier transform for real data, each harmonic gives rise to two peaks, at both positive and negative spatial frequency. Comparing the phase between two measurements yields a value that is proportional to the change in delay between these measurements. If the wavelength of the harmonic is known, this can be used to extract the exact change in delay.





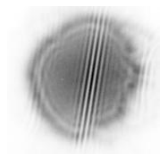
# Diffractive shear interferometry for extreme ultraviolet high-resolution lensless imaging

## Abstract

We demonstrate a novel imaging approach and associated reconstruction algorithm for far-field coherent diffractive imaging, based on the measurement of a pair of laterally sheared diffraction patterns. The differential phase profile retrieved from such a measurement leads to improved reconstruction accuracy, increased robustness against noise, and faster convergence compared to traditional coherent diffractive imaging methods. We measure laterally sheared diffraction patterns using Fourier-transform spectroscopy with two phase-locked pulse pairs from a high-harmonic source. Using this approach, we demonstrate spectrally resolved imaging at extreme ultraviolet wavelengths between 28 and 35 nm.

---

This chapter is based on: G. S. M. Jansen, A. de Beurs, X. Liu, K. S. E. Eikema, and S. Witte, *Diffractive shear interferometry for extreme ultraviolet high-resolution lensless imaging*, Opt. Express 26, 12479-12489 (2018)

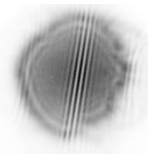


## 5.1 Introduction

In recent years, coherent diffractive imaging (CDI) has enabled vast progress in high-resolution microscopy [8], [25], [120]–[122]. Contrary to traditional microscopy, CDI does not rely on lenses to form an image from scattered light emerging from a sample. Instead, CDI employs numerical phase retrieval algorithms to reconstruct an image based on the recorded diffraction pattern [13], [85]. As the image resolution in CDI is not limited by focusing optics, it is well suited for microscopy using x-rays [9], extreme ultraviolet (EUV) radiation [25], [122] or electrons [123]. Despite the high-resolution results, the quality of the reconstructed intensity and phase of the images depends strongly on the signal-to-noise of the diffraction pattern [124]. Furthermore, other constraints such as finite support, positivity or atomicity are often required for convergence. This has led to the development of ptychography [32], [86], [87], which eliminates the need for strong constraints by taking much more data in a systematic manner.

The central challenge in CDI is to acquire knowledge of the phase of the recorded field. Performing a direct measurement of the phase is therefore beneficial, but typically does come at the cost of increased measurement complexity. The main example of such an approach is Fourier transform holography, in which the interference between a reference wave and a diffraction pattern is recorded [35], [93], [94], [125], [126]. Holography allows for a simple image reconstruction which does not rely on iterative algorithms, but the image resolution and support are typically limited by the numerical aperture and wavefront of the reference wave.

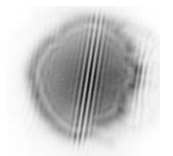
Spatial phase determination of optical fields is a challenge that has been addressed in other areas as well. A specific approach that has shown promise in the context of CDI is lateral shearing interferometry (LSI) [109], [127], a technique that is used to reconstruct the wavefront - or phase profile - of a beam by interfering it with a sheared copy of itself. This results in an interference pattern that depends on the spatial derivative of the wavefront, which can be retrieved by spatial Fourier filtering. The wavefront can then be reconstructed by integration of the measured phase derivative. As a single LSI measurement only yields the one-dimensional derivative of the phase along the shear direction,



several measurements with different shears are in principle necessary to retrieve the full 2D wavefront. Furthermore, accurate phase determination is only possible if the individual beams have smooth intensity profiles. The LSI phase profile can also be measured by phase shifting one of the beams and measuring the interference pattern for several phases. Isolation of the oscillating interference term then allows for direct determination of the interference phase. Such a measurement allows for measurement of much more complex interference patterns. It has been shown that a collection of shear interference patterns for varying shears allows for the full reconstruction of the original electric field [128]. Simple numerical propagation of the electric field then enables phase contrast microscopy in various geometries.

In this article, we build upon the concept of lateral shearing interferometry to acquire differential phase information of diffraction patterns recorded with extreme ultraviolet radiation. The resulting diffraction intensity and differential phase information are then used as input for an iterative algorithm, that can reconstruct the full electric field based on a single laterally sheared diffraction pattern. The measurement and reconstruction of these diffraction patterns can be summarized as diffractive shear interferometry (DSI). In comparison with traditional coherent diffractive imaging methods, we find that our approach provides an improved reconstruction accuracy and convergence. For an experimental demonstration of the DSI approach, we measure laterally sheared diffraction patterns at several extreme ultraviolet wavelengths and numerically reconstruct high-resolution images from them.

To achieve spectral resolution, we employ spatially-resolved Fourier-transform spectroscopy (FTS) with a pair of phase-locked high-harmonic generation (HHG) sources [129]. A previous limitation of this FTS approach for HHG-based imaging has been the fact that the HHG beams need to be spatially displaced to avoid cross-talk in the HHG process [111]. The DSI approach presented here uses this sheared beam geometry in a natural way, even allowing improved reconstruction accuracy and robustness compared to single-beam experiments. From our results we find that our algorithm is able to accurately reconstruct complex electric fields even in the presence of significant noise. Coherent diffractive imaging with HHG sources has great potential for nanoscale imaging [25], [122]. Furthermore, elements often possess dis-



tinct absorption features at EUV wavelengths. Therefore, the present work forms a step towards EUV imaging with element-specific contrast.

## 5.2 Spatial shearing interferometry of diffraction patterns

### Interference of diffraction patterns

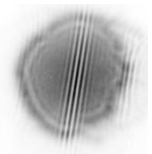
In traditional CDI, the object is illuminated using a single beam of coherent, monochromatic light. The transmitted or reflected light scatters from the object and forms a diffraction pattern which is captured using a camera. In order to combine CDI with lateral shearing interferometry, we use two identical, mutually coherent beams to illuminate the object at slightly differing angles, as schematically depicted in Fig. 5.1. For a thin, single-scattering object, the electric fields of the beams can then be written as the electric field of the illumination multiplied by the object transfer function. If  $dk$  is the wavevector corresponding to the half angle  $\alpha/2$  between the two beams and  $x$  the transverse position in the object plane, the electric field corresponding to a single beam appearing directly after the object can be written

$$E_{\pm} = \tilde{A}(x) \exp[i(\tilde{\Phi}(x) \pm dkx)] \exp(-i\omega t_{\pm}), \quad (5.1)$$

where "+" and "-" correspond to the individual beams as indicated by Fig. 5.1. Effectively, the fields in Eq. (5.1) consist of the amplitude  $\tilde{A}(x)$  and phase  $\tilde{\Phi}(x)$  of the electric field transmitted by the object, multiplied by a linear phase ramp  $\exp(\pm idkx)$  that distinguishes the two individual beams. Finally, there is a global phase term  $\exp(i\omega t_{\pm})$ . This electric field propagates towards the detector where the interference between  $E_+$  and  $E_-$  is detected. In the case of far-field diffraction, the electric field can be described by the Fourier transform of the electric field in the object plane. The detected intensity can then be written as

$$I(k) = A(k + dk)^2 + A(k - dk)^2 + A(k + dk)A(k - dk)e^{i[\Phi(k+dk) - \Phi(k-dk) + \omega T]} + c.c., \quad (5.2)$$

where the combined amplitude and phase  $A(k) \exp[i\Phi(k)]$  at the camera is related by Fourier transform to the combined amplitude and



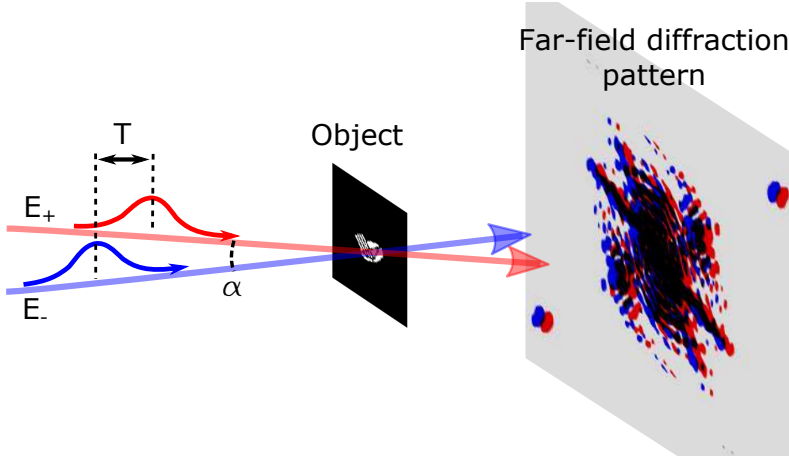
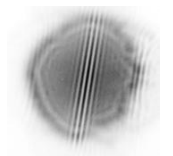


Figure 5.1: Schematic overview of lensless imaging by diffractive shear interferometry. Two identical and coherent beams,  $E_+$  and  $E_-$ , illuminate a transmissive object such that the angle between the beams is  $\alpha$ . This results in two far-field diffraction patterns on the camera which are slightly displaced relative to each other. The black region on the screen indicates where the diffraction patterns overlap and interfere.

phase  $\tilde{A}(x) \exp[i\tilde{\Phi}(x)]$  at the object. For simplicity, the time difference between the beams is written as  $T$ . Compared to single-beam CDI, the detected intensity in DSI contains more information as it encodes the phase shear in the interference term. This will naturally lead to a more stringent camera-space constraint that can be expected to aid convergence of phase retrieval algorithms [130]. Yet the available information can be exploited more effectively by separating the amplitude and phase terms in the interference term  $A(k + dk)A(k - dk) \exp i[\Phi(k + dk) - \Phi(k - dk)]$ . This can be achieved by performing measurements at multiple time delays  $T$ , as the interference is the only term in Eq. (5.2) that oscillates at frequency  $\omega$ . Going one step further, taking a series of measurements as a function of  $T$  is equivalent to Fourier transform spectroscopy, and can even be used to extract interference terms for all frequencies present in the case



of broadband illumination. Therefore, the proposed DSI approach is intrinsically compatible with polychromatic or broadband light sources such as high-harmonic generation, and can be used for spectrally resolved imaging at extreme ultraviolet wavelengths [111].

### Image reconstruction

To reconstruct an image of the object, retrieval of the full electric field  $A(k) \exp[i\Phi(k)]$  is required. Starting with the isolated interference term from Eq. (5.2), we will use an iterative algorithm to reconstruct the electric field. This algorithm relies on a set of constraints to the electric field, applied in different planes connected by free-space optical propagation [8], [13], [85]. The first constraint is provided by the measured data: the electric field at the camera plane should be consistent with the measured result. For our second constraint we will use a finite support; the electric field in the object plane is only non-zero in a certain limited window.

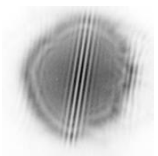
In traditional CDI, the most used camera plane operator is the modulus constraint: the amplitudes of the electric-field estimate are set to the measured values, while the estimated phases are preserved. However, in DSI the modulus constraint is not the most suitable operator for reconstructing interferometrically sheared diffraction patterns. This is because the measured intensity pattern  $A(k + dk)A(k - dk)$  is not equal to the intensity  $A(k)^2$  of the electric field to be reconstructed. Even though a modulus constraint based on Eq. (5.2) may be envisaged, it does not take into account the available phase information in an optimal way. We therefore derive a new camera plane operator that makes more efficient use of the amplitude and phase information available in DSI.

Starting with the  $n^{\text{th}}$  guess of the electric field

$$E_n(k) = A_n(k) \exp[i\Phi_n(k)] \quad (5.3)$$

at the camera and the complex measured interference pattern

$$M(k) = A(k + dk)A(k - dk) \exp\{i(\Phi(k + dk) - \Phi(k - dk))\}, \quad (5.4)$$



it can be seen that division of the measured data by a sheared copy of the electric field guess yields a new electric field guess

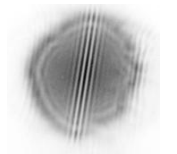
$$E_{n+1}(k + dk) = \frac{M(k)}{E_n^*(k - dk)}. \quad (5.5)$$

If the original guess of the electric field is accurate, the new electric field guess is in fact equal to a shifted version of the electric field. Therefore, division of the measured data by a negatively sheared electric field guess yields a positively sheared electric field guess. This operation forms the basis of a useful camera-space constraint for interferometrically sheared diffraction pattern reconstruction. A general camera-space constraint can be written as

$$\begin{aligned} E_{n+1}(k) = & (1 - \beta)E_n(k) \\ & + \frac{\beta}{2} \frac{M(k - dk)E_n(k - 2dk)}{|E_n(k - 2dk)|^2 + \alpha^2} \\ & + \frac{\beta}{2} \frac{M^*(k + dk)E_n(k + 2dk)}{|E_n(k + 2dk)|^2 + \alpha^2}, \end{aligned} \quad (5.6)$$

which is a linear combination of the old guess and the average of the new guesses for the positively and negatively sheared electric fields. The numerical constant  $\beta$  determines the strength of the correction to the electric field guess and is typically set to 0.9. Instead of a direct division by the electric field  $E$ , we multiply by  $E^*/(|E|^2 + \alpha^2)$ , where  $\alpha$  is a regularization constant that prevents errors arising from division by zero. For noisy data, we expect that the best results will be obtained when  $\alpha$  is comparable to the noise floor.

In combination with a finite object support, the presented novel camera-space constraint is sufficient for retrieval of the full electric field. A basic approach to include a support constraint in the algorithm is using the error-reduction method, where all values outside of the support are set to zero. The output-output algorithm and hybrid input-output algorithms provide two alternatives which have been shown to provide different convergence properties [85], [131].

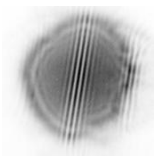


### Comparison between DSI and single-beam CDI

To investigate the efficiency of the proposed phase-retrieval algorithm, we performed simulations comparing DSI to traditional single-beam CDI methods. Example datasets for CDI are produced by simulating far-field diffraction patterns with Poisson noise. We simulated several diffraction patterns with varying signal-to-noise ratio (SNR) by adjusting the total number of collected photons. To account for camera readout noise, we added Gaussian background noise with a standard deviation of 10 counts. Starting with a wide initial support, we reconstructed the image using both hybrid input-output and error-reduction in an alternating fashion. The shrinkwrap procedure was used to adaptively update the support [84]. The results of these simulations can be seen the first two columns of Fig. 5.2. In this figure, each row has a different SNR. The top row is simulated such that we get  $10^8$  counts in the brightest pixel, leading to a SNR of  $10^4$  in the center of the diffraction pattern. The second and third row have SNRs of  $1.8 \cdot 10^3$  and  $0.6 \cdot 10^3$  respectively.

For DSI, we simulated several datasets with noise levels similar to the CDI simulations. This was achieved by adding Poisson noise and a Gaussian background to the shear interferometry signal. To also account for noise in the phase of the simulated interference pattern, we multiplied the simulated noise with a random phase pattern before addition to the noise-free diffraction pattern. The amplitude and phase of the simulated diffraction patterns can be seen in the third and fourth columns of Fig. 5.2 respectively. We verified that this method leads to realistic interference signals by comparing the simulated diffraction patterns to the result of a full simulated Fourier transform scan. Furthermore, we compared the simulated data to real measured EUV shearing interferometry data (section 5.3).

Reconstructions of the simulated DSI signals are shown in the fifth column of Fig. 5.2. These reconstructions were obtained by combining the algorithm presented in section 5.2 with a shrinkwrap procedure to find the support of the image. In order to compare these results to those obtained from the CDI simulations, we calculate the accuracy of the reconstructions. This is defined as the RMS difference between the reconstruction and input image, averaged over the number of pixels

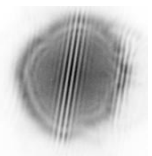




and only calculated for the pixels in the direct vicinity of the original object. This calculation is corrected for spatial shifts and a global phase offset, which are free parameters for CDI. For DSI, we find that there is a limited number of spatial shifts and phase offsets compatible with the measured data. This is directly related to the phase information in the recorded diffraction pattern, as a shift of the object translates to a phase tilt in the far-field diffraction pattern. After shearing according to formula 5.4, this phase tilt reduces to a phase offset in the measured data. Reversing the process shows that a phase offset in the measured data leads to a shift of the reconstructed object, and any image reconstruction has to match this constraint.

From the reconstruction accuracy comparison in the sixth column of Fig. 5.2, it is clear that DSI consistently leads to a better solution than single-beam CDI. In addition, the reconstruction of DSI patterns appears to converge slightly faster than the reconstruction of single-beam CDI patterns. There are various parameters which influence the performance of DSI reconstruction, of which the value of the shear is the most critical. For the simulations presented in Fig. 5.2, we assumed that the shear was known accurately. For real measurements, accurate initial knowledge of the shear may not be possible, especially in cases where the shear has to be known with sub-pixel accuracy. In such cases, it is possible to extend the phase retrieval algorithm with a shear optimization step. As will be mentioned in section 5.3, for our present reconstructions we have used a manual search to find the correct shear.

Furthermore, the value of the shear has a strong influence on the measured signal and therefore on the retrieval process. If the shear is reduced to zero, the shear interferometry signal reduces to the single-beam far-field diffraction pattern and the phase information is reduced to zero. As the shear is increased, both the intensity of the diffraction pattern and the phase information become more complex-structured. Finally, very large shears lead to a reduced overlap between the diffraction patterns, leading to a weaker signal that is more sensitive to noise. We simulated several measurements with different shears, and found that larger shears lead to slightly better results and faster convergence, provided that the SNR remained sufficiently high. The shear used in Fig. 5.2 was approximately equal to one speckle of the diffraction pattern (the inverse of the object size), which is found to be a good



compromise between signal strength and noise sensitivity.

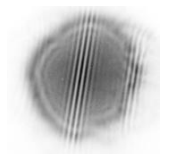
## 5.3 Experimental demonstration of diffractive shear interferometry using high-harmonics

As already noted in section 5.2, a promising approach to measuring DSI signals is through the use of a setup for Fourier-transform spectroscopy. Such a measurement enables coherent diffractive imaging using all wavelengths present in the illumination. We implement this scheme by employing a phase-locked pair of high-harmonic generation (HHG) sources to perform wavelength-resolved microscopy at EUV wavelengths. The phase-locked EUV pulse pair is produced by HHG upconversion of tightly phase-locked pairs of infrared driving pulses that have been produced by an ultrastable common-path interferometer [129]. Typical parameters of these infrared pulses are a central wavelength of 800 nm, a pulse energy of 1 mJ in each of the beams, a 300 Hz repetition rate and a pulse duration of 25 femtoseconds. A basic layout of the setup used for HHG and subsequent DSI imaging of samples in a transmission geometry is presented in Fig. 5.3(a). A typical EUV spectrum generated in Argon is also shown in Fig. 5.3(b). It is important to note that the HHG spectrum can change significantly due to small changes in the driving laser alignment.

The Fourier transform spectroscopy settings must be adapted to the HHG source spectrum. In practice, this means recording a few hundred time steps, spanning an optical path difference of at least two optical cycles of the driver in steps smaller than half the wavelength of the shortest harmonic [111], [129]. These settings depend strongly on the on-sample illumination spectrum. For monochromatic illumination, just four time steps would suffice.

### Fourier-transform holography

As a first experiment, we used focused ion-beam milling to fabricate the sample shown in Fig. 5.4(a). The sample consists of our institute logo and in addition three circular apertures with diameters 12, 4 and 1  $\mu\text{m}$ , respectively. The apertures act as references for Fourier-transform



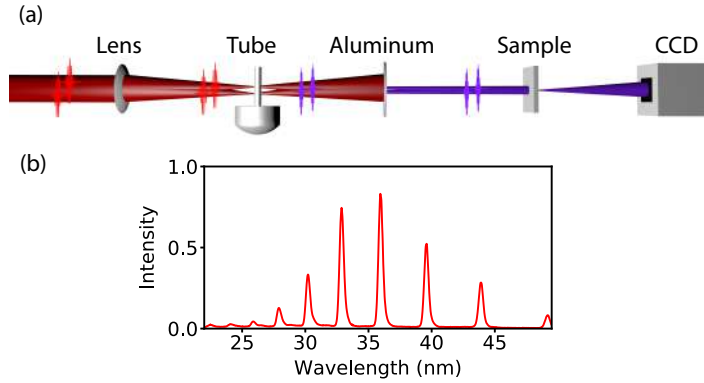
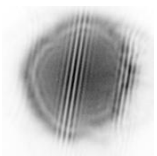


Figure 5.3: (a) Schematic overview of the setup used for EUV Fourier-transform interferometry. The output of a common-path interferometer is focused by the lens into a gas jet confined to tube. The resulting EUV pulse pair is separated from the infrared using an Aluminum filter and detected using an Andor Ikon-L CCD camera. A transmissive object can be positioned between the Aluminum filter and the camera using a remotely controlled translation stage. (b) Typical high-harmonic spectrum generated in Argon, measured through Fourier-transform spectroscopy in the same setup without an object in the beam.

holography (FTH) by providing a spherical wave which interferes with the diffraction pattern arising from the logo [93]. For such a sample, a spatial Fourier-transform of the far-field diffraction pattern directly yields multiple images of the sample. The resolution of these images is determined by the diameter of the associated reference aperture. Therefore, FTH can provide an initial low-resolution guess of the image from which it is possible to determine the support. It is then possible to use phase-retrieval methods to improve the image resolution and contrast [125], [132].

The results obtained using only FTH are shown in Fig. 5.4. We used Fourier-transform spectroscopy to retrieve monochromatic shear interferometry signals for several individual high-harmonics. Every image of the Fourier transform spectroscopy measurement consists of



### 5.3. Experimental demonstration of DSI using high-harmonics

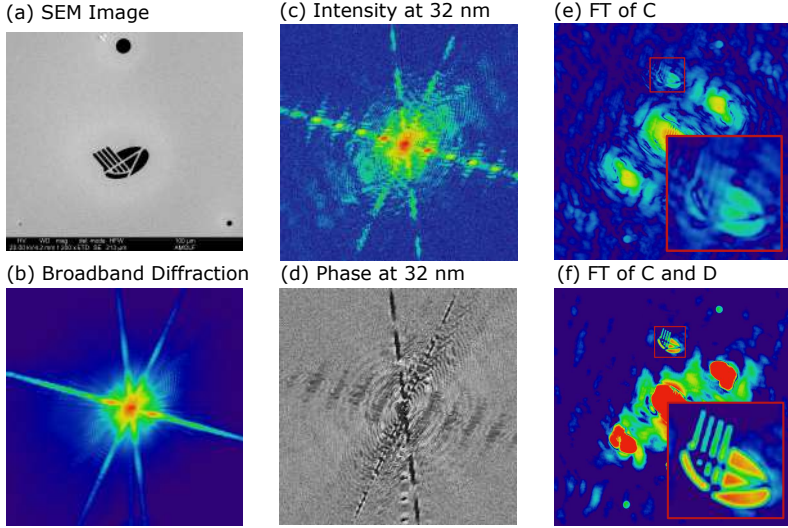
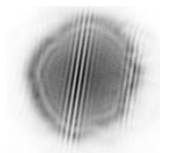


Figure 5.4: Extreme ultraviolet DSI of a transmissive sample with multiple holographic references. (a) Scanning electron microscope image of the sample used for the initial measurements at EUV wavelengths. The sample consists of our institute logo and three circular apertures with diameters 12, 4 and 1  $\mu\text{m}$  respectively acting as holographic references. (b) Broadband EUV transmission of the sample. (c) Intensity at 32 nm retrieved from the FTS-scan. (d) Phase of the signal at 32 nm. (e) Hologram acquired using just the intensity at 32 nm as shown in (c). (f) Hologram acquired using both intensity and phase information at 32 nm. The inset show the hologram arising from interference with the 4  $\mu\text{m}$  aperture.

a 10 second exposure, a 1 second exposure and a 0.1 second exposure to acquire the high dynamic range necessary for high-resolution CDI. The spectral resolution in this experiment is 96 THz, providing an effective bandwidth  $\Delta\lambda/\lambda$  of approximately 1/100 for the retrieved shear interferometry signals around 30 nm wavelength. As an example, we show the amplitude and phase of the shear interferometry signal for the 25th harmonic at 32 nm in Fig. 5.4(c) and (d) respectively. To illustrate the importance of the phase pattern, Fig. 5.4(e) shows



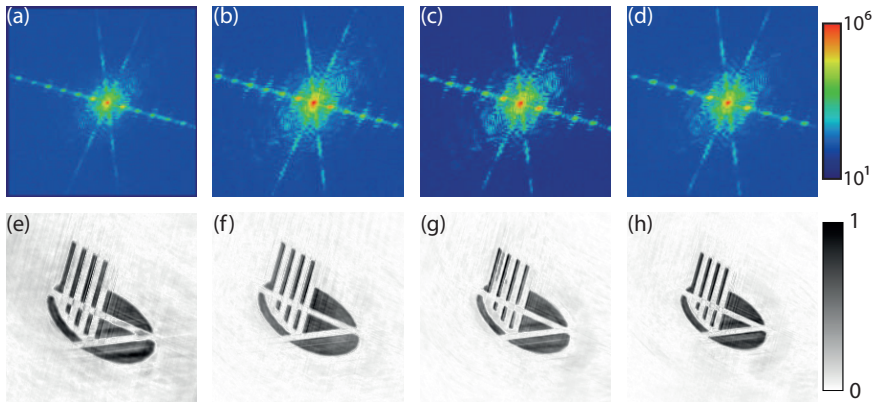
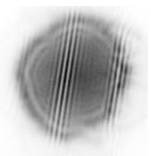


Figure 5.5: DSI reconstruction results of the multi-wavelength data presented in Fig. 5.4. (a-d) for the ARCNL research center logo. Measured amplitude of the DSI patterns for the 29th, 27th, 25th and 23rd harmonics with wavelengths 28 nm, 30 nm, 32 nm and 35 nm respectively, shown on a logarithmic color scale. (e-h) Reconstructed images for the 29th to 23rd harmonics respectively, show on a linear grayscale. The images all have a height and width of 200 pixels, while the sample has a width of 40  $\mu\text{m}$ . The difference in magnification follows directly from the differences in wavelength between the images.

the hologram calculated from the amplitude data alone, which has low contrast and contains clear distortions. We find that it is possible to retrieve a good-quality hologram from the shear interferometry signal if both measured amplitude and phase are used to calculate the hologram, as shown in Fig. 5.4(f). Note that the holograms arising from the 1  $\mu\text{m}$  aperture are not visible, which is probably due to limited signal-to-noise.

### DSI reconstruction

The holography results provide a decent starting point for electric field reconstruction using DSI. For this reconstruction the holography result is used to determine an initial support. The determination

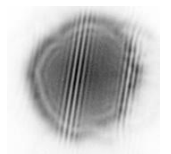


of the initial support is slightly complicated by the presence of the reference apertures, as it is important to position the supports for the apertures at the correct positions relative to each other and to the main object. To accommodate for slight errors in this process, we start the image reconstruction with an object support that is larger than the image obtained through holography. The object support is determined from the hologram by thresholding and expanding the result by a few pixels. We found that applying the object support using a linear combination of error reduction and hybrid input-output leads to the best convergence.

As with the DSI simulations, we combine the image reconstruction with a shrinkwrap routine. In addition, we performed a manual parameter search to find the optimal value for the shear. A simple search algorithm was used to find the phase offset in the measured data. These steps are performed by comparing the convergence over several hundred iterations for various values of the shear and phase offset. Typically, a retrieval sequence to reconstruct an image with known shear and offset phase is as follows: Using the initial support, 600 iterations of DSI with HIO and ER are performed, such that every object space operation is a linear combination of 10% HIO and 90% ER. During these iterations, the value for the regularization constant  $\alpha$  is ramped down from 80 to 40. Then we perform six rounds of shrinkwrap followed by 200 DSI+ER+HIO iterations with constant  $\alpha$ . As shown in Fig. 5.5, we were able to reconstruct high-quality images using this approach for four individual high-harmonics between 28 and 35 nm from a single measurement.

#### DSI imaging of complex objects

To verify that DSI also works for more complicated physical data, we fabricated another sample, shown in Fig. 5.6(a). It was produced by focused ion-beam (FIB) milling in a 100 nm gold layer on top of a freestanding 15 nm silicon nitride film. The settings of the FIB caused it to strip most of the gold while leaving a fine and irregular silicon nitride mesh. As the mesh is partially transparent to EUV radiation, this yields a sample that has a complicated pattern of transmission levels. Furthermore, the sample did not contain holographic reference



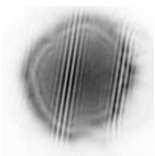
apertures.

Similar to the measurement of the holography sample, we are able to obtain monochromatic interference patterns for several wavelengths through an FTS scan. In this case, each time step of the FTS scan consists of a 4 second exposure and two shorter ones. This lead to a 7 second measurement time per time step and a total measurement time of 50 minutes. As an example, Fig. 5.6(c) shows the amplitude and phase of the DSI pattern obtained for the 25th harmonic at 34 nm. In this case, the spectral resolution was 81 THz, yielding an effective bandwidth of 1/109 at 34 nm wavelength.

For the reconstruction, the initial object support was now retrieved from the autocorrelation of the sample. This provides a larger initial support and eliminates the need for a fine determination of the offset phase. We did perform a new shear optimization, as the experimental geometry changed slightly in this measurement. With the optimal shear, we perform 2100 DSI iterations combined with 75% ER and 25% HIO, using shrinkwrap every 75 iterations. The reconstruction is finished using 1400 DSI iterations combined with 90% ER and 10% HIO, using shrinkwrap every 25 iterations. During the full reconstruction,  $\alpha$  is ramped down smoothly from 1000 to 10. The final result is shown in Fig. 5.6(b). By calculating the phase-retrieval transfer function, we find that the final result has a resolution of approximately 0.27  $\mu\text{m}$ . This resolution corresponds to the diffraction limit of the captured data. Comparing the SEM and DSI images, it is clear that DSI is able to reconstruct the full complexity of the sample including the partial transmission of the silicon nitride mesh. This demonstrates that DSI is a promising technique to image complex isolated samples.

## 5.4 Conclusions

In conclusion, we have developed the method of diffractive shear imaging, in which the full electric field of a diffraction pattern is reconstructed based on the measurement of a single sheared diffraction pattern. Comparing the algorithm to standard phase retrieval methods for traditional CDI, we find that our method consistently yields more accurate results. In addition, the phase retrieval process converges



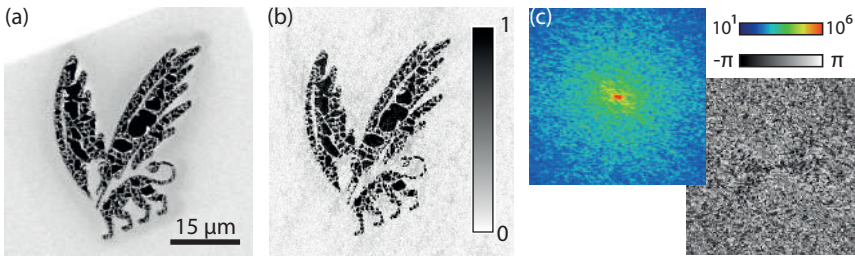
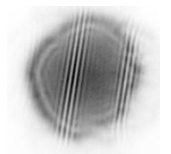


Figure 5.6: Results obtained for a complex ‘griffin’ sample without holographic references. (a) SEM image of the sample as described in section 5.3. (b) DSI reconstruction of the sample at 34 nm wavelength, shown on a linear colorscale. (c) Measured amplitude (logarithmic false color) and phase (gray) of the DSI pattern used to obtain (b).

slightly faster than traditional approaches. As DSI signals can be easily measured using spatially-resolved Fourier-transform spectroscopy, this approach is ideally suited for multi-wavelength coherent diffractive imaging [111]. In particular, this approach is interesting for CDI using high-harmonic generation sources, which produce a broad range of narrowband harmonics at extreme ultraviolet wavelengths. We have demonstrated high-resolution microscopy on two different samples using several high-harmonics at wavelengths between 28 and 35 nm. There are several possible extensions which may lead to an even more versatile imaging technique. For example, rotation of the sample enables the measurement of shear interferometry signals at different effective shears. A set of these measurements can greatly enhance the image retrieval, and reduce the need for a well-defined object support. Furthermore, combining diffractive shear interferometry with ptychographic techniques can lead to a greater field of view while still preserving spectral sensitivity.

## 5.5 Appendix: Holography in a DSI setting

In the published part of this chapter, we have used Fig. 5.4e,f to demonstrate that the phase measured through Fourier transform spectroscopy



is relevant for spectrally resolved coherent diffractive imaging. The influence of this phase can be made more explicit through a straightforward calculation which is presented in this Appendix.

In Fourier transform holography (FTH), the electric field in the detector plane can be written as the sum of the object electric field  $E_{obj}$  and the reference electric field  $E_{ref}$ :

$$E_{\pm}(k) = E_{obj}(k \pm dk) + E_{ref}(k \pm dk). \quad (5.7)$$

In the DSI measurement geometry, we can distinguish two copies of this electric field, displaced by  $+dk$  and  $-dk$  respectively. For simplicity, we will consider only a single spectral component. The signal measured in DSI is given by

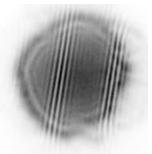
$$M(k) = E_{+}^{*}(k)E_{-}(k), \quad (5.8)$$

which is equivalent to Eq. 5.4 if we substitute  $E(k) \rightarrow A(k)e^{-i\Phi(k)}$ . Combining Eq. 5.7 and Eq. 5.8, and expanding the terms, the signal can be written as

$$\begin{aligned} M(k) = & E_{obj}^{*}(k + dk)E_{obj}(k - dk) + E_{ref}^{*}(k + dk)E_{ref}(k - dk) \\ & + E_{ref}^{*}(k + dk)E_{obj}(k - dk) + E_{obj}^{*}(k + dk)E_{ref}(k - dk). \end{aligned} \quad (5.9)$$

The last two terms of this signal are the product of a reference wave with an object wave. Using the convolution theorem, it is then easy to see that a Fourier transform of the full signal will yield two separate holograms: one where the reference wave from  $E_{+}$  is convolved with the object wave from  $E_{-}$ , and one where the reference wave from  $E_{-}$  is convolved with the object wave from  $E_{+}$ . Thus, in order to extract the FTH hologram in DSI, the full complex measured signal  $M(k)$  must be Fourier transformed, and not just the amplitude.

A striking difference with traditional FTH is the fact that the two holograms are not identical. This is indeed also observed experimentally, as close inspection of the data for Fig. 5.4 shows significant differences between the holograms. These differences are more clearly visible in the enlarged images shown in Fig. 5.7. These differences can be traced back to the illumination of the sample.  $E_{+}$  and  $E_{-}$  are derived from separate HHG beams illuminating the sample. There can



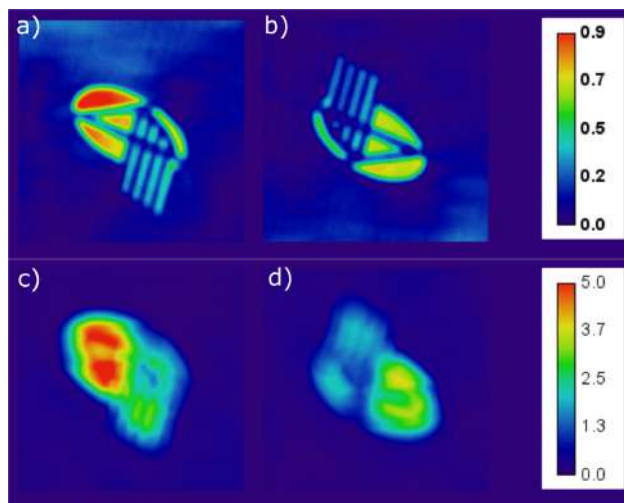
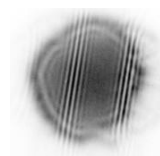


Figure 5.7: Hologram pairs as retrieved from DSI-FTH for the 23<sup>rd</sup> harmonic at 35 nm, as achieved with a 4  $\mu\text{m}$  pinhole (a and b) and with a 12  $\mu\text{m}$  pinhole (c and d). The differences between left and right are explained by the unique properties of the DSI measurement.

therefore be intensity and phase differences in the object and reference waves transmitted by the sample. In an extreme case, one of the beams could have zero intensity at the reference aperture. In that case, the hologram for that aperture and beam combination disappears, while the other hologram is unaffected.





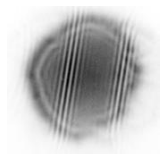
# Broadband extreme ultraviolet dispersion measurements using a high-harmonic source

## Abstract

We demonstrate direct dispersion measurements of various thin films at extreme ultraviolet (EUV) wavelengths, using a table-top laser-driven high-harmonic generation (HHG) source. In this method, spatially separated identical EUV pulses are generated through HHG with a pair of phase-locked infrared pulses. The EUV pulses are re-imaged to a sample plane using a single toroidal mirror, such that one pulse illuminates the target thin film while the other pulse passes through a reference aperture. By comparing the EUV interference with and without sample, we are able to extract the dispersion properties of the sample, integrated over the full film thickness. We have measured thin films of titanium, nickel, copper and silicon nitride, demonstrating that this technique can be applied to a wide range of materials, only requiring a film thin enough for sufficient EUV transmission.

---

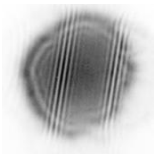
This chapter is based on: G. S. M. Jansen, X. Liu, K. S. E. Eikema, and S. Witte, *Broadband extreme ultraviolet dispersion measurements using a high-harmonic source*, Opt. Lett. **44**, 3625-3628 (2019).



## 6.1 Introduction

Accurate knowledge of dielectric constants is crucial for the determination of the optical response of materials. Recently, the development of extreme ultraviolet (EUV) lithography and the widespread availability of EUV light sources for scientific and technological purposes have sparked an increased interest in dielectric constants at EUV wavelengths [133]–[135]. A major source of dielectric constants and related material properties is the X-ray database compiled by the Center for X-Ray Optics (CXRO), which is based on work of Henke *et al.* [28]. In this database, atomic scattering factors are used to derive optical properties such as the refractive index, absorption length and reflection coefficient. While this provides excellent results for a large part of the spectrum, it is somewhat limited in the EUV range (10 - 124 eV, 124 - 10 nm). In particular, being purely atomic scattering data, it does not account for any structural or molecular effects which may be relevant for these low energies, leading to possible discrepancies [136]. Furthermore, the real part of the atomic scattering factor has not been tabulated below 30 eV, so that optical properties of materials in that wavelength range remain undetermined.

There have been several efforts towards the measurement of dielectric constants in the extreme ultraviolet regime, typically using a synchrotron or high-harmonic generation (HHG) sources of EUV light. For example, in angle-resolved reflectometry, the reflectance from a thin film is measured for a range of angles [137]–[140]. Film parameters such as the complex refractive index, density, thickness and roughness can then be retrieved by fitting the data to a suitable model. This measurement is typically performed for many incident photon energies. A similar approach has been used to retrieve the refractive index from the forward scattering or diffraction of nanoparticles [141]. Another approach to measure the complex refractive index employs the Kramers-Kronig relationship. Based on an accurate measurement of the energy-dependent absorption, these relations can be used to calculate the full refractive index [142]–[144]. A more direct approach to measure the refractive index and absorption of a material is based on interferometry [145]. In such experiments, the transmission of a thin film is made to interfere with a reference wave. The refractive

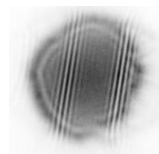


index and absorption can be retrieved directly from the interference phase and amplitude respectively.

In this Letter, we present a novel implementation of an ultra-broad-band interferometric EUV dispersion measurement, based on Fourier-transform spectroscopy (FTS). To this end we use two independently generated, but phase-locked, sources of HHG that function as a probe and reference. We ensure sub-attosecond accurate timing (and therefore phase) control through the use of a birefringence-based common-path interferometer [129]. By scanning the relative phase between the sources, we are able to measure the wavelength-dependence of the sample-induced phase over the full HHG spectrum in a single measurement. The measurement geometry is simple and versatile, and the setup is of table-top size. The presented approach directly measures the optical path length through the sample. It is therefore much more robust against surface effects such as roughness or oxidation compared to reflection-based measurements [139], [140]. It does not require variation of the angle-of-incidence and it works independent of the EUV spectrum produced by the HHG source.

## 6.2 Experimental setup

For our experiments, we use the output of a Titanium-sapphire seeded non-collinear optical chirped pulse amplifier (NOPCPA). This system provides 8 mJ pulses with a 25 fs duration, has a spectrum centered around 840 nm wavelength, and has a repetition rate of 300 Hz. These pulses are split into pairs of identical pulses with a controllable and intrinsically stable delay, using an interferometer based on birefringent wedges [129]. After the interferometer, the pulse pairs are focused in a gas jet for high-harmonic generation. In the gas jet, the individual pulses are spatially separated by approximately 300  $\mu\text{m}$  by applying a small tilt to the final wedge in the interferometer. This ensures that both pulses generate high-harmonic independently. In order to get a spectrum covering the EUV regime, we generate high-harmonics in neon gas. We use a 200 nm thick, free-standing aluminum filter to separate the EUV from the driving infrared radiation. Behind the filter, we observe a spectrum of the 17<sup>th</sup> up to 49<sup>th</sup> harmonic, spanning



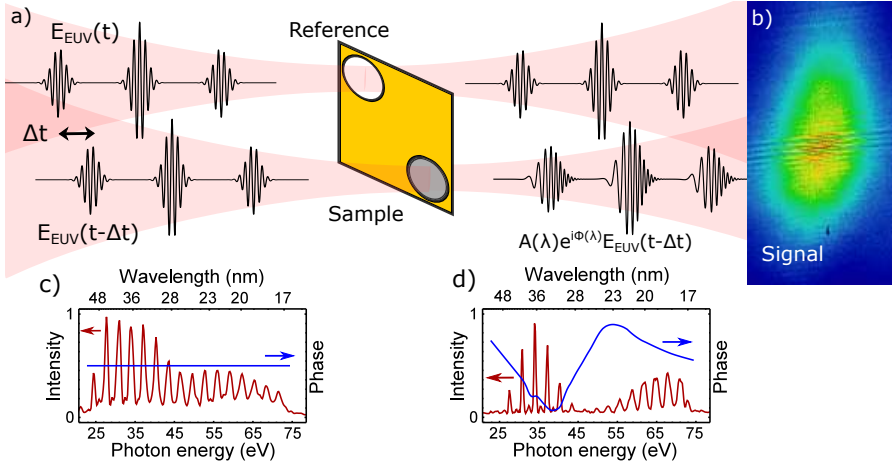
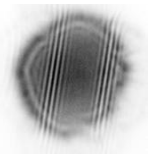


Figure 6.1: Schematic overview of the extreme ultraviolet interferometry for dispersion measurements. **a**: From the left, two identical EUV pulses are imaged to a mask with a reference aperture and sample aperture. The sample modulates the incident pulse in phase and amplitude, which is visible in the far-field interference on the camera (**b**). By scanning the delay between the beams, we perform Fourier-transform spectroscopy. Typical spectral intensities (red) and relative phase between the pulses (blue) as measured without a sample are shown in (**c**) and a spectrum as measured with 30 nm thick titanium sample is shown in (**d**)

from 50 to 17 nm (25-72 eV).

After the high-harmonic generation the two EUV beams diverge, so that they overlap and interfere in the far field. In order to separate probe and reference for the refractive index measurement, we use a boron-carbide ( $\text{B}_4\text{C}$ ) coated toroidal mirror with a  $7.5^\circ$  grazing incidence angle and a 25 cm focal length to re-image the HHG sources to the sample plane. At this grazing incidence angle, the boron-carbide is expected to have a high reflectivity of up to 80% without a strong wavelength-dependence. The spectra observed after the toroidal mirror agree with this expectation.

In the sample plane (Fig. 6.1a), we use a three-dimensional piezo-



driven translation and rotation stage (SmarAct) to position a mask with a sample and a reference aperture. This mask consists of a 15 nm thin, 250 by 250  $\mu\text{m}$  wide silicon nitride membrane. The membrane is partially coated with a 100 nm gold layer, ensuring that it is opaque for EUV radiation, except for one corner of the membrane which is not coated with gold. We then deposited a thin layer of the material to be investigated over the full membrane, so that in the corner without gold only the material under investigation is deposited, while the rest of the membrane is opaque due to the gold layer. Finally, we used focused ion-beam milling (FIB) to clear an aperture in the opposite corner of the membrane. The mask therefore consists of two transmitting regions:

1. the sample corner, consisting of either 15 nm or 50 nm silicon nitride and for example 25 nm of titanium.
2. a reference aperture, typically a circular hole of 10  $\mu\text{m}$  diameter.

### 6.3 Analysis

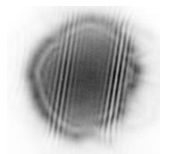
After the sample, the beams diverge again and overlap in the far-field. There, the detected signal at position  $\vec{r}$  on the detector  $S(\vec{r}, \lambda, \Delta t)$  consists of the coherent addition of the probe  $E_p$  and reference  $E_r$  beam:

$$S(\vec{r}, \lambda, \Delta t) = \int |E_p(\vec{r}, \lambda, t) + E_r(\vec{r}, \lambda, t - \Delta t)|^2 dt \quad (6.1)$$

As the detector receives the full source spectrum, a measured interference pattern at a given time delay  $\Delta t$  is the integral of (6.1) over all wavelengths  $\lambda$  present in the illumination. Note that in this letter, we write  $\lambda$  for the wavelength in vacuum. Integrating (6.1) over time, the signal for a single wavelength  $\lambda$  can be written as

$$S(\vec{r}, \lambda, \Delta t) = |A_p(\vec{r})|^2 + |A_r(\vec{r})|^2 + A_p(\vec{r})A_r(\vec{r}) \exp[i(2\pi c\Delta t/\lambda + \Delta\Phi(\vec{r}, \lambda))] + c.c., \quad (6.2)$$

where  $A_p$  and  $A_r$  are the amplitudes of the probe and reference beams respectively and  $\Delta\Phi$  is the phase difference between the beams. A Fourier-transform spectroscopy (FTS) measurement consists of a series of intensity measurements over a range of delays. As the contribution



for every wavelength  $\lambda$  oscillates at its characteristic frequency  $2\pi c/\lambda$ , a Fourier transform over the time domain can be used to extract the relevant part of the measured signal

$$M(\vec{r}, \lambda) = A_p(\vec{r})A_r(\vec{r}) \exp(i\Delta\Phi(\vec{r}, \lambda)). \quad (6.3)$$

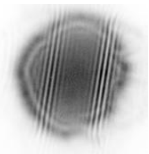
The settings for the FTS scan are optimized for the characteristics of the HHG spectrum. As the shortest wavelength is 17 nm, the delay step between measurements must at least be smaller than 8.5 nm. Typically, a delay step of 5 nm was used. The length of the delay scan is set by the desired spectral resolution. We typically used a scan length of 3.1 fs, which provides sufficient spectral resolution to resolve the individual high-harmonics while still keeping the total measurement time relatively short at 15 minutes per delay scan.

The phase difference between the probe and reference contains several contributions. In general, the phase difference  $\Delta\Phi$  is the sum of the sample-induced phase  $\Phi_{sample}$ , a geometry-related phase  $\Phi_{geo}$  and any phase variation  $\Phi_{HHG}$  arising from the high-harmonic generation itself. For a simple multilayer sample, we approximate the sample phase as the sum of the optical path length differences induced by the materials:

$$\Phi_{sample}(\lambda) = \sum_i \frac{n_i(\lambda)d_i}{\lambda} \quad (6.4)$$

which contain the individual wavelength-dependent refractive indices  $n_i(\lambda)$  and thicknesses  $d_i$ . For such thin films care should be taken that possible multilayer interference effects are properly taken into account: we have also performed simulations using Fresnel theory and found that for our simple, strongly absorbing layer structures the approximation of (6.4) is accurate to within a few mrad. For our planar samples the sample-induced phase has no transverse spatial dependence  $\vec{r}$ .

The geometric phase is determined by the optical path length difference between the beams, arising from the source geometry and refocusing optics, and does not depend on the presence of a sample. As the two EUV beams are generated in separated spots, the geometric phase is dominated by a linear phase ramp leading to a Young's double slit-type interference pattern (Fig. 6.1b). In addition to the linear phase ramp, the geometric phase also contains a higher-order spatial



structure originating from the toroidal mirror aberrations. The two EUV beams have a slightly differing incidence angle on the toroidal mirror, which leads to a difference in astigmatism between the beams. Such aberrations can be reduced using a pair of toroidal mirrors [146], but in our experiment all geometry-induced phase effects are removed through a calibration measurement, as detailed below.

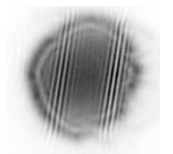
Finally, it is possible that there are phase differences arising from the high-harmonic generation. While the two HHG sources are optimized to be identical, slight differences cannot be excluded. In particular, differences in gas pressure and spatial and temporal chirp of the driving pulses may lead to a phase difference depending on position and wavelength. A systematic offset between the two sources can be removed similar to the geometric phase, but variations during the measurements can be a source of fluctuations in the retrieved phase signal.

In order to extract the sample induced phase, we perform a series of three measurements: 1) a reference measurement  $M_{ref}$  without a sample in either beam, 2) a measurement  $M_{sample}$  with the sample in one of the beams, and 3) an 'inverse' measurement with the sample rotated by  $180^\circ$ , interchanging the role of sample and reference beams. By multiplying the result of the sample measurement with that of the conjugate reference measurement, we get

$$M_{sample}(\vec{r})M_{ref}^*(\vec{r}) = A_r^3(\vec{r})A_p(\vec{r})\exp(i\Phi_{sample}(\lambda)), \quad (6.5)$$

which subtracts the geometric and HHG phase from the measurement. We then apply an intensity threshold, ensuring that only those pixels and wavelengths with sufficient signal-to-noise ratio are included in the final phase determination. Finally, we extract the phase as a function of wavelength, integrated over position to improve the signal-to-noise ratio. This analysis procedure is performed for the rotated sample geometry as well, after which the average of the analysis results for both geometries is taken, to eliminate the influence of possible differences between the EUV beams.

Presently, the reproducibility of the interferometer used in the FTS scans forms the main technical limitation to the experimental accuracy. We typically observe slight variations of the absolute interferometer arm lengths between individual scans, resulting in an arbitrary time



## 6. BROADBAND EUV DISPERSION MEASUREMENTS

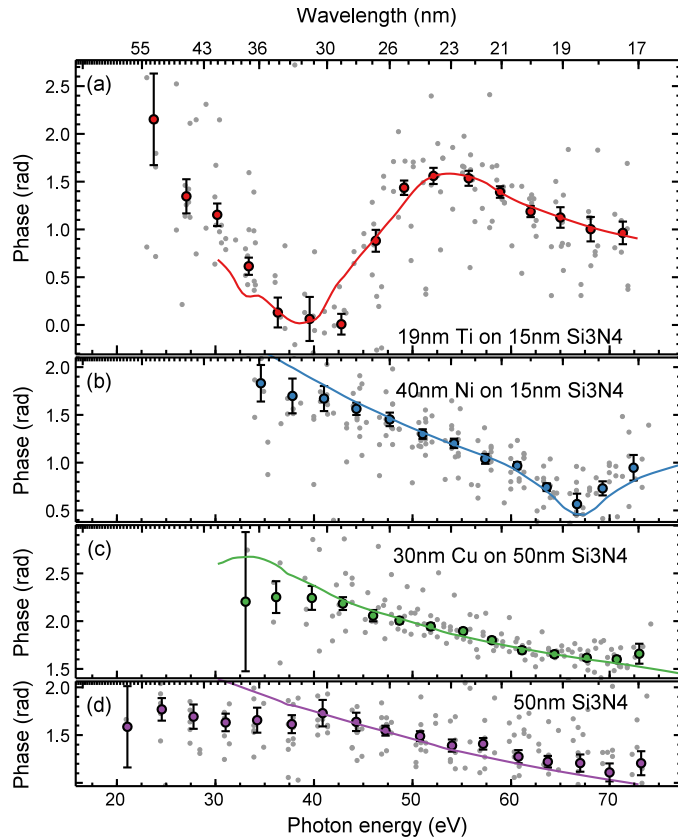
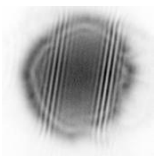


Figure 6.2: Measured phase induced by various metal films on silicon nitride: (a) Titanium, (b) Nickel, (c) Copper, and (d) bare Si<sub>3</sub>N<sub>4</sub>. Individual measurement points are shown in grey, while the colored points show the mean phase and standard deviation of the mean for each harmonic. The lines show the prediction for 30 eV and higher energies based on CXRO values for the refractive index. For titanium, the thickness was determined to be  $19.0 \pm 1.6$  nm titanium on 15 nm silicon nitride based on a fit of the data. For nickel and copper, the transmission at energies below 35 eV was insufficient for a phase measurement. No CXRO data is available for photon energies below 30 eV.

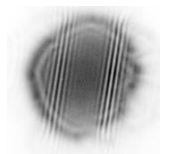


delay variation of  $\sim 100$  as from one scan to the next. After the analysis described above using (6.5), such a variation corresponds to 30 nm in optical path length and 0.1 rad/PHz in phase slope. As this variation is random, the measurement accuracy can be further improved by averaging multiple measurements. In our present system this procedure results in an expected accuracy for the phase slope at the  $10^{-2}$  rad/PHz level, but hampers the retrieval of the absolute phase delay introduced by the sample for a sufficiently accurate refractive index determination. Nevertheless, with a better translation stage in the FTS scan this would become possible. As this was not available, we have instead focused on the relative phase influence and determined the group-delay dispersion from it.

## 6.4 Experimental results and discussion

We have measured the sample-induced phase for four different samples: a 25 nm titanium film, a 40 nm nickel film, both sputter coated on 15 nm silicon nitride membranes, a 30 nm copper film on a 50 nm silicon nitride membrane and a bare 50 nm silicon nitride membrane. For every sample we performed several measurement series. The results from these measurements and comparisons with the expected phase delay from CXRO data are shown in Fig. 6.2. We performed the sample and reference measurements sequentially, consisting of FTS scans with and without sample. These measured dispersion data are corrected for the global phase offset arising from the uncertainty in the absolute timing between the beams. We do this by adding a constant phase to the measured phase curves shown in Fig. 6.2, to facilitate a comparison of the measured data with the CXRO expectation.

The observed spectral phase dependence follows the reported literature curves to within the measurement accuracy, and our measurements extend the dispersion data for Ti and  $\text{Si}_3\text{N}_4$  down to 20 eV photon energy. For the titanium data set, we found that the measured phase had a smaller wavelength-dependent variation than initially expected based on the assumption that the titanium film was 25 nm thick, hinting to a lower film thickness. We therefore performed a least-squares fit of the data to the CXRO model using the Titanium



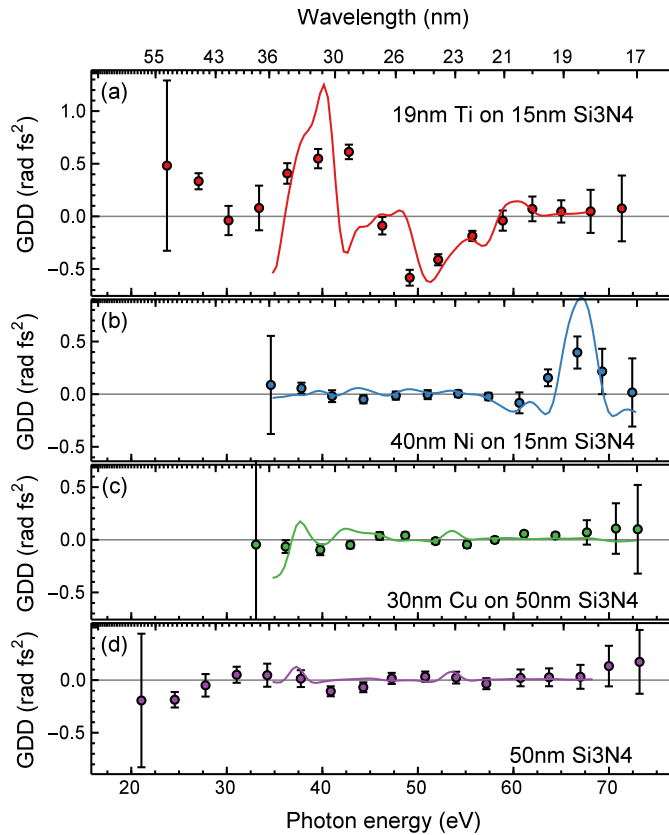
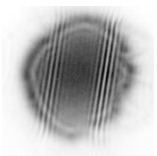


Figure 6.3: Group delay dispersion retrieved from the data of Fig 6.2 for (a) Titanium, (b) Nickel, (c) Copper, and (d) bare Si<sub>3</sub>N<sub>4</sub> (filled points), along with the GDD as calculated from CXRO reference data (solid lines).

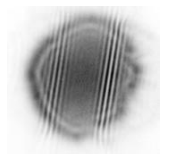


layer thickness as a free parameter. This fit resulted in a layer thickness of  $19.0 \pm 1.6$  nm, which is within the uncertainty range and calibration accuracy of the fabrication process. Similar agreement between measurement and expectation is found for nickel, copper and silicon nitride, although the linear component of the phase slightly differs from the expectation. For silicon nitride, where this difference is the largest, the deviation is roughly 0.04 rad/PHz, which is still in the range of expected variation due to the interferometer repeatability. Both nickel and copper suffer from strong absorption at low photon energy, which limited the observable interference to the 35 to 72 eV spectral region and results in increased error bars towards lower energy.

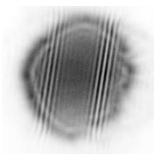
Higher-order dispersion properties are not influenced by the absolute timing uncertainty in the measurement, and can therefore be determined in an absolute sense. Figure 6.3 shows the group delay dispersion across the full spectral range as retrieved from the measured data. The results mostly agree with reference data within the statistical measurement accuracy of typically 0.1 rad fs<sup>2</sup>, with some deviations at the positions of strong spectral variation, which may be improved by denser spectral sampling.

As discussed above, the main error source in these measurements comes from the interferometer reproducibility between sample and reference measurements. Improving the absolute timing reproducibility between the interferometer arms to 5 as would enable a determination of the optical path length of a sample with 1.5 nm accuracy from a single scan. That corresponds to an absolute phase accuracy of 5% at 30 nm wavelength and an accuracy for the group delay of 5 mrad/PHz, which goes beyond any other method for dispersion measurements in this soft-X-ray wavelength range, and would enable full complex refractive index determination.

In this experiment, we measured dispersion averaged over the spatial domain for thin films. Furthermore, this approach can be combined with Fourier-transform holography [94], enabling dispersion mapping with nanometer-scale spatial resolution. Another potential application is the characterization of EUV multilayer mirrors, which can be used to control the spectral phase of high harmonics [147]. The spectral range was determined by the HHG source and the Al filter, but the FTS-based interferometry approach is compatible with more complex



and even continuous EUV source spectra. Therefore, the method can readily be extended in spectral range through the combination with e.g. few-cycle driving pulses [148], mid-IR-drivers [100] or optical gating [149] combined with different filters.



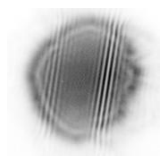
## Outlook on quantitative lensless imaging

The previous chapters describe the development spectrally and spatially resolved metrology using high harmonics. In chapter 4, Fourier transform spectroscopy is introduced a practical approach to acquire both spatial and spectral resolution. Fourier-transform spectroscopy (FTS) is demonstrated to be viable at wavelengths as short as 17 nm. Furthermore, stability measurements indicate that this method can be extended to much shorter wavelengths, even covering the water window between 2 and 4 nm, a range particularly interesting for microscopy due to the reduced absorption of water.

In chapter 5, the possibility of spectrally resolved coherent diffractive imaging (CDI) in this unique measurement geometry is investigated. It follows that the monochromatic diffraction patterns obtained through FTS are fundamentally different from traditional diffraction patterns. Effectively, the measured pattern is the interference of two sheared diffraction patterns, hence the name *diffractive shear interferometry*. These measurements allow for high-resolution CDI, if a custom iterative reconstruction algorithm is used.

Finally, in chapter 6, Fourier-transform spectroscopy is applied to measure the optical path length of thin films. This provides a direct measurement of the sample group velocity dispersion at EUV wavelengths, and it can be extended to a full refractive index measurement.

With these three chapters, it is clear that FTS with high harmonics provides a powerful and flexible quantitative microscopy technique.



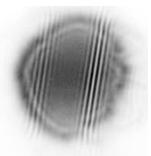
Nevertheless, there are still various possible extensions to the presented technique. In particular, spectrally-resolved coherent diffractive imaging has not been demonstrated for samples with a significant wavelength dependence. Interesting samples could include thin metal films with varying thickness or structured multilayer films. With diffractive shear interferometry, the spatially varying absorption and optical path length difference of the sample can be measured. From these parameters, it is possible to determine the elemental composition and thickness.

## 7.1 Spectral resolution with a wide field of view

Diffractive shear interferometry has only been demonstrated for small isolated samples. This situation greatly simplifies the image reconstruction. The two illuminating high-harmonic beams can be assumed to have identical beam profiles over the sample, such that the only difference between the diffracted waves is a wavefront tilt. It therefore suffices to reconstruct a single electric field. Furthermore, the small isolated sample enables the use of a tight support constraint.

However, there is a large class of samples which are not isolated. Recently, ptychography has proven itself as a lensless imaging approach for large extended samples. This is achieved by scanning a small illumination probe over the sample [86], [98]. Another benefit of ptychography is the ability to reconstruct object and probe separately [89]. This allows for determination of object parameters such as absorption, without prior knowledge of the probe.

A promising prospective is the combination of scanning illumination and high-harmonic Fourier-transform spectroscopy. In this situation, FTS provides monochromatic diffraction patterns from which an image can be reconstructed, while the scanning illumination enables that image to be extended to a larger field of view. It has already been demonstrated that ptychographic algorithms can reconstruct data recorded with multiple wavelengths simultaneously [32], [150], or illumination which fluctuates in time [98]. Similar reconstruction algorithms could be applied to the raw data as measured in a combined ptychography



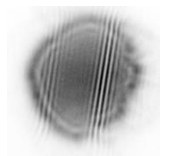
and FTS measurement.

As an alternative solution, ptychographic reconstruction using the measurement constraint from DSI can be applied to the monochromatic data retrieved from FTS. In DSI, it is necessary that the illuminating beams have identical beam profiles over the sample. Based on the HHG geometry for Fourier transform spectroscopy, this only happens far away from the EUV focus, leading to a relatively low illumination intensity on the sample. If the EUV beams are refocused, the two beams focus to two spatially separated spots. It is therefore not possible to perform DSI in or close to the focus. Due to this requirement, the sample is usually placed further downstream, where large portion of the generated EUV flux does not illuminate the sample. This results in longer acquisition times.

It may however be possible to overcome this limitation with a scanning illumination approach using refocused high harmonics. After refocusing the high harmonics, there is a region where the two beams are partially overlapping and confined to a small area. Depending on the exact position and refocusing, this area can be a few tens of micrometers in diameter. This enables the measurement of well-sampled diffraction patterns even with extended samples. It allows for the use of the full refocused HHG flux for spectrally-resolved coherent diffractive imaging. Because the two beams are displaced relative to each other, they probe different parts of the sample and produce different diffraction patterns. Furthermore, aberration of the focusing optics can lead to different beam profiles for the two beams. The monochromatic far field diffraction pattern for a single time step  $dt$  and illumination position  $x_0$  is therefore given by the coherent sum of the two diffraction patterns,

$$I(k) = \left| FT\{P_1(x)O(x - x_0) + P_2(x + dx)O(x - x_0)e^{-i\omega dt}\} \right|^2, \quad (7.1)$$

in which  $P_1$  and  $P_2$  are the two probes and  $O$  the sample transmission function,  $dx$  is the displacement between the beams and  $x_0$  is the position of the sample. The phase difference between the beams is determined by the time delay  $dt$ . It is important to note that interference does not depend on spatial overlap of the probes on the sample but rather on overlap in the far field. The detected broadband diffraction

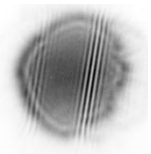


pattern can be calculated by summing this expression over all present wavelengths. To acquire a full ptychographic measurement set, the position  $x_0$  is scanned such that there is significant overlap between adjacent illuminations. At each position, a range of time steps  $dt$  is measured, effectively performing Fourier transform spectroscopy for every position.

In the absence of time scanning, the recorded dataset is identical to a ptychographic dataset resulting from multiple mutually incoherent modes corresponding to the various wavelengths. This data can be reconstructed using existing ptychographic algorithms with modal decomposition [32], [91], [150]. It follows that just position scanning is enough to enable spectrally-resolved imaging in ptychography. The accuracy and efficiency of the image reconstruction in multi-wavelength ptychography depends strongly on the width of the spectrum and the position step size during the measurement. For broader spectra, a higher degree of overlap between illuminations will be necessary [32]. Furthermore, ptychography with the full high-harmonic spectrum has not been demonstrated. It is in this situation that Fourier-transform interferometry can provide crucial additional information.

As for the exact implementation of time-scanning in ptychography, there are two scenarios. The first approach would be to perform a full FTS measurement, such as is done in DSI. In this case, the time step is set small enough to resolve fringes of the shortest harmonic, while the scan length is made long enough to achieve sufficient spectral resolution. In ptychography, the required spectral resolution depends on the probe beam size and the numerical aperture of the detector [29]. This leads to a long delay scan, from which monochromatic diffraction patterns can be extracted. In this situation, the maximal amount of information is extracted from the delay scan.

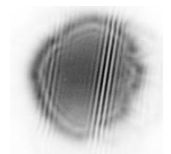
A promising alternative to the full FTS measurement is to use a much shorter delay scan. Because the rough HHG spectrum is known in advance, there is no need to achieve high spectral resolution. The spectral resolution can then be reduced simply by measuring less time steps. In situations like this, where only a limited number of spectral components is expected to be non-zero, compressed sensing can also provide a faster measurement with little loss in the quality of the final signal [151]. Based on compressed sensing techniques, a small, carefully



## 7.1. Spectral resolution with a wide field of view

---

chosen, subset of the measurements in the full FTS scan can provide sufficient spectral information. The reduced measurement time this provides is especially beneficial since scanning illumination requires a time scan at many positions.





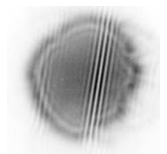
# Spectrally resolved single-shot wavefront sensing of broadband high-harmonic sources

## Abstract

Wavefront sensors are an important tool to characterize coherent beams of extreme ultraviolet radiation. However, conventional Hartmann-type sensors do not allow for independent wavefront characterization of different spectral components that may be present in a beam, which limits their applicability for intrinsically broadband high-harmonic generation (HHG) sources. Here we introduce a wavefront sensor that measures the wavefronts of all the harmonics in a HHG beam in a single camera exposure. By replacing the mask apertures with transmission gratings at different orientations, we simultaneously detect harmonic wavefronts and spectra, and obtain sensitivity to spatiotemporal structure such as pulse front tilt as well. We demonstrate the capabilities of the sensor through a parallel measurement of the wavefronts of 9 harmonics in a wavelength range between 25 and 49 nm, with up to  $\lambda/32$  precision.

---

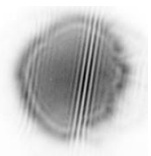
This chapter is based on: L. Freisem, G. S. M. Jansen, D. Rudolf, K. S. E. Eikema, and S. Witte, *Spectrally resolved single-shot wavefront sensing of broadband high-harmonic sources*, Opt. Express 26, 6860-6871 (2018).



## 8.1 Introduction

Accurate measurements in imaging and optical metrology often rely on a precise knowledge of the incident beam parameters. The Hartmann wavefront sensor, first introduced in the year 1900 to calibrate telescopes [152], quickly became a standard tool to characterize optical wavefronts. The sensor consists of an opaque plate containing a structured array of apertures, and the wavefront information is retrieved by measuring the propagation of light transmitted through the holes. Detecting the positions of the aperture transmission with respect to a known reference provides amplitude and local phase tilts of a monochromatic wavefront simultaneously, from which the wavefront is then reconstructed. A widely used modification to increase the sensitivity of Hartmann sensors is the lenslet array introduced by Platt and Shack [153] in 1971. In the regime of extreme ultraviolet (EUV) radiation, where lens arrays are challenging, the traditional hole array was shown to be a useful approach for the characterization of monochromatic synchrotron beams [154] and high-harmonic generation (HHG) sources [155].

High-harmonic generation sources [22], [100], [156] are becoming a mature table-top source of coherent EUV radiation, used in many applications such as nanoscale imaging [25], [98], [122], soft-X-ray spectroscopy [157] and attosecond physics [99], [158], [159]. However, a significant limitation of Hartmann sensors is their inability to provide spectral sensitivity. This is particularly important for the characterization of HHG beams, as it is known that the wavefronts of different harmonics can be substantially different [20]. Spectral wavefront variations in HHG may arise as a result of the phase matching geometry [160], [161], and can convey information about quantum path interferences in the HHG process [162]. Introducing a controlled spectrally dependent wavefront tilt actually is the basis for the attosecond lighthouse effect, which can be used to produce isolated attosecond pulses [163], [164]. To extract spectrally resolved wavefront information, several methods have been demonstrated, such as slit scanning combined with grating-based spectrometry [165], [166], and lateral shearing interferometry [109], [167]. While these methods retrieve spectrally resolved wavefront information, they all depend on some



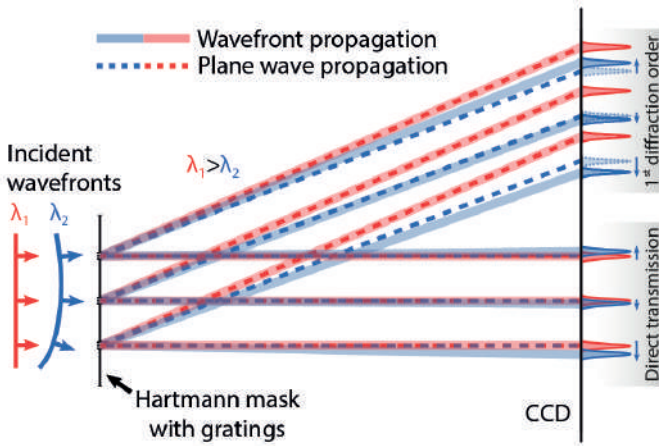
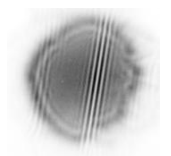


Figure 8.1: Diffraction scheme of the multi-wavelength Hartmann sensor. The direct transmission spots of all spectral components overlap and cannot be distinguished. In contrast, in the first diffraction order the different spectral components are spatially separated, while still containing the wavefront information through the displacement of the spots with respect to a set of reference positions.

form of mechanical scanning in obtaining a complete dataset, and therefore can only measure average wavefronts over many pulses. Due to the nonlinear nature of the HHG process, the influence of small driving pulse variations on the phase matching process can lead to wavefront fluctuations on a shot-by-shot basis. Such fluctuations may in turn have consequences in experiments where knowledge of the input parameters typically limits the achievable accuracy, such as EUV scatterometry [135] and coherent diffractive imaging [168].

In this article we introduce a novel wavefront sensor concept called a Spectroscopic Hartmann Mask (SHM), that provides wavefront data for multiple spectral components directly in a single camera exposure. We replace the apertures of the Hartmann mask by transmission gratings which, in addition to the regular Hartmann spot pattern, produce replicas of this spot pattern at the  $\pm 1^{\text{st}}$  diffraction orders as shown schematically in Fig. 8.1. These diffracted beams have similar



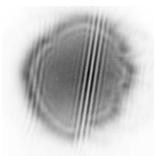
sensitivity to local wavefront tilts at each aperture, while the different harmonics can be clearly separated in the image. The use of both positive and negative diffraction orders makes it possible to distinguish shifts due to wavefront from shifts due to wavelength. This approach enables the isolation and analysis of Hartmann spot patterns for the individual wavelengths of all harmonics in a HHG beam simultaneously from a single camera recording. The SHM wavefront sensor concept enables fast characterization of full HHG beams, even on a single-pulse basis for sufficiently bright beams, providing a unique tool for characterization of broadband short-wavelength sources and sensing of the underlying physics of the HHG process.

## 8.2 Spectrally resolved wavefront characterization

### Spectroscopic Hartmann mask design

A scanning electron microscope image of the SHM is displayed in Fig. 8.2, along with insets that show the individual gratings in more detail. To ensure clear separation of the spot patterns for the different harmonics, the mask design and the distance to the camera are important parameters. If the SHM-to-camera distance is too small, the first-order diffraction spots are not spread out sufficiently, leading to overlapping signal on the detector. Conversely, if the distance is too large, diffraction resulting from the apertures leads to larger spot sizes, resulting in overlapping spots of neighboring apertures. Using Fresnel diffraction theory to simulate the detected intensity patterns, it is readily possible to find designs that satisfy the requirements for different HHG spectra. The SHM design shown in Fig. 8.2 enables wavefront measurements for all harmonics produced in argon using a fundamental wavelength of 810 nm. Moreover, there is some flexibility for measurements at both longer and shorter wavelengths by changing the distance between mask and camera.

Compared to conventional Hartmann masks, the sampling density of the apertures in the SHM design is an even more important design parameter. This complexity stems from the fact that each aperture



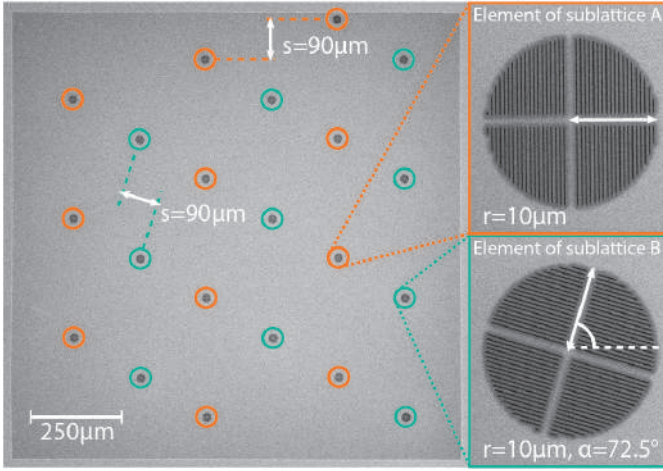
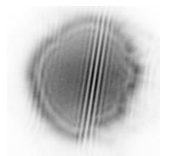


Figure 8.2: Scanning electron microscope image of the sample, with two insets showing magnified examples of the two main grating alignment groups. The gratings of one subset are rotated by an angle  $\alpha = 72.5^\circ$ , ensuring that the diffraction does not overlap with the diffraction of the other grating group. To improve the structural stability of the  $d = 0.5 \mu\text{m}$  pitch gratings, additional  $1 \mu\text{m}$ -wide support bars are used, forming a cross through their center.

now leads to a multitude of diffraction spots for the different harmonics, which all need to be spatially separated in order to retrieve accurate wavefront data. The total number of apertures is then limited by the maximum window size, which in our case was  $1 \times 1 \text{ mm}$ . However, the sampling density and number of apertures in the presented design still allows wavefront characterization up to the fourth-order Zernike polynomials, which is sufficient for many practical purposes. Optimized designs with increased sampling density can be envisaged with more modelling efforts.

The SHM is fabricated by milling holes into a  $200 \text{ nm}$  thick,  $1 \times 1 \text{ mm}$  sized silicon nitride membrane, covered with  $5 \text{ nm}$  chromium and  $27 \text{ nm}$  gold, using the focused ion-beam technique. The individual apertures are circular with a radius  $r = 10 \mu\text{m}$ , and contain a transmission grating with a pitch  $d = 0.5 \mu\text{m}$ . With this design, positioning the SHM

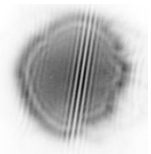


at 3 cm from the camera ensures clear separation of high harmonics in the 20-60 nm wavelength range generated using 810 nm fundamental wavelength, while diffraction from the circular apertures themselves remains limited. To avoid overlap between the diffraction from adjacent apertures, the gratings are tilted at  $17.5^\circ$  with respect to the row of apertures, which ensures that the rows of diffraction spots are separated by  $90\ \mu\text{m}$  on the camera. In addition, we orient the gratings in two different directions. Having multiple diffraction directions allows a higher spatial sampling density of the beam while avoiding overlapping spots on the camera. Furthermore, it enables detection of systematic effects (more detail given below), reducing the sensitivity to angular misalignment and making the sensor essentially self-referencing.

### Measuring HHG wavefront data

To demonstrate spectrally resolved wavefront measurements of high-harmonic beams, we use the output of a Ti:sapphire-seeded non-collinear optical parametric chirped-pulse amplifier (NOPCPA). The 1 mJ, 25 fs, 810 nm laser pulses are focused with an  $f = 25$  cm lens into a pulsed gas jet, resulting in harmonics produced in argon or krypton covering the 25 – 56 nm wavelength range. We use an adjustable iris to optimize HHG phase matching, leading to a Gaussian EUV beam. A 200 nm thick aluminum foil is used to block the infrared radiation. An EUV-sensitive CCD-camera (Andor Ikon-L) is used to detect the radiation at approximately 63 cm away from the HHG source. The SHM is mounted on a translation stage and positioned in the beam at 3 cm before the camera.

A camera recording of the SHM diffraction pattern is shown in Fig. 8.3. Each aperture leads to an array of diffraction spots in the direction perpendicular to the grating lines, corresponding to the individual harmonics. As a guide to the eye, the diffraction from two apertures with different grating orientations are highlighted by the dashed boxes (note that the color coding corresponds to Fig. 8.2). In addition to the normal Hartmann spot pattern from the direct transmission in the center of the image, the individual harmonics produce clearly separated diffraction spots in the  $\pm 1^{\text{st}}$  diffraction orders, of which the positions can be determined accurately by a standard two-dimensional Gaussian



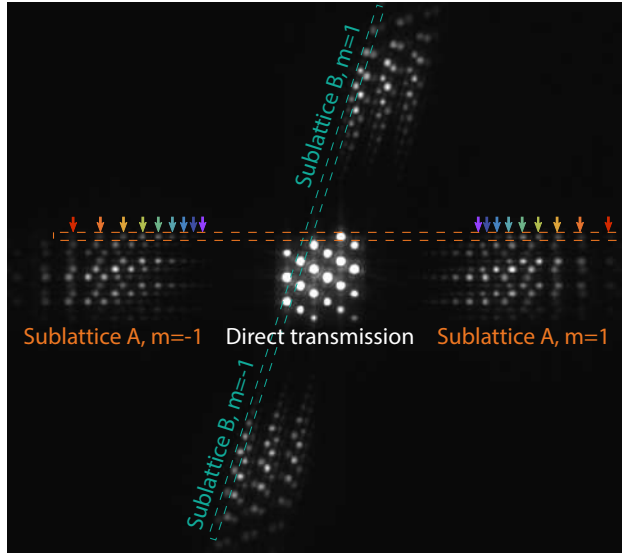
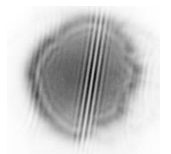


Figure 8.3: Diffraction pattern of the spectroscopic Hartmann mask, obtained using high harmonics generated in argon. This image was taken using a one second exposure. In addition to the central group of spots from direct transmission, there are four groups of diffraction spots, which correspond to the  $\pm 1^{\text{st}}$  diffraction orders of the different gratings. All these spots are distributed along the two main diffraction directions, corresponding to the grating orientations as pointed out in Fig. 8.2. As a guide to the eye, the diffraction spots corresponding to one horizontal and one vertical grating are highlighted by orange and green boxes. For all apertures, the individual harmonics are spatially separated in the first diffraction orders, enabling wavefront reconstruction.



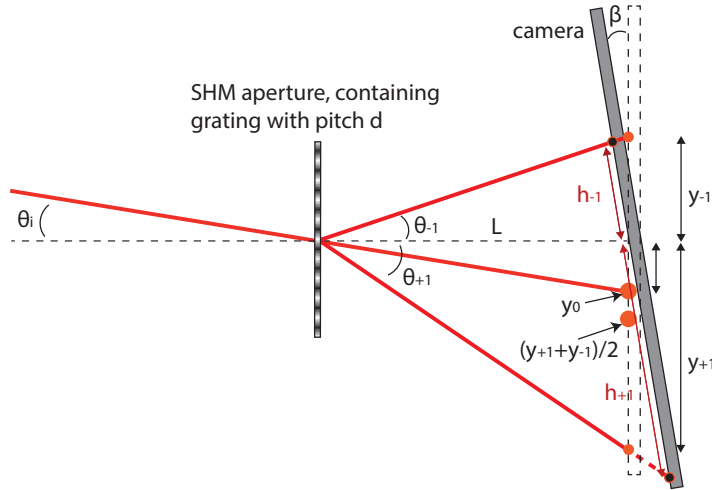
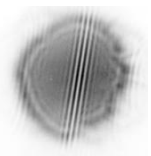


Figure 8.4: Schematic overview of the transmission of a single spectroscopic Hartmann aperture. The center of mass of the  $+1^{\text{st}}$  and  $-1^{\text{st}}$  diffraction orders approximates the position of the direct transmission. The quality of this approximation depends on the incident wavefront tilt as well as the angle between camera and wavefront sensor.

fitting procedure. As schematically depicted already in Fig. 8.1, these first-order diffraction spots are sensitive to the local wavefront tilts. Therefore they can be used to do wavefront reconstruction, for all harmonic orders simultaneously. In the present experiment up to nine harmonics are observed: the wavefronts of all the individual harmonics can be reconstructed from the single camera image of Fig. 8.3. To increase the accuracy of the spot determination further, we recorded images with exposure times up to 5 seconds in argon, and 10 seconds in krypton for the results described in section 8.3. To further improve spot position determination, an interesting possibility would be the use of higher diffraction orders, which have lower efficiency but are better separated along the diffraction direction.



### SHM diffraction pattern analysis

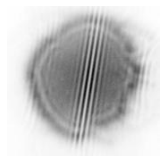
Once the respective positions of all diffraction spots corresponding to each wavelength have been determined, all the required information for reconstructing the wavefronts is in principle available. Because of the diffraction geometry, there are some subtle differences compared to the traditional Hartmann mask analysis. A schematic overview of the diffraction geometry for a single aperture is drawn in Fig. 8.4. At a distance  $L$  behind the SHM, the  $\pm 1^{\text{st}}$  diffraction orders appear at positions  $y_{\pm 1}$ . The main principle of the SHM is that a nonzero wavefront tilt angle  $\theta_i$  leads to a shift of the  $\pm 1^{\text{st}}$  diffraction orders that is similar to the shift in the direct transmission position  $y_0$ . Therefore, the center of mass  $(y_{+1} + y_{-1})/2$  of these diffraction positions can be used as input for the wavefront reconstruction algorithm. However, as indicated in Fig. 8.4, there are two additional effects that need to be taken into account. First of all, for a non-zero  $\theta_i$ , the shift of the  $\pm 1^{\text{st}}$  diffraction orders is not perfectly symmetric, leading to an offset between their combined center of mass position and  $y_0$ . Secondly, there may be a finite angle  $\beta$  of the camera with respect to the SHM. In this case, the measured positions of the diffraction spots are given by  $h_{\pm 1}$ , which are related to the expected positions as  $h_{\pm 1} = y_{\pm 1} \cos \theta_{\pm 1} / \cos(\theta_{\pm 1} \mp \beta)$ . Overall, the position of the measured spot position for the  $m^{\text{th}}$  diffraction order at a wavelength  $\lambda$  can be written as:

$$h_m = \frac{L(m\lambda - d \sin(\theta_i))}{d \sin(\beta + \arccos(\frac{m\lambda}{d} - \sin(\theta_i)))}, \quad (8.1)$$

where  $d$  is the grating pitch and  $L$  is the distance between SHM and camera.

Starting from Eq. 8.1 and using a Taylor approximation to quantify the effect of small variations in  $\theta_i$  and  $\beta$ , we find an expression for the center of mass position:

$$\begin{aligned} (h_{-1} + h_1)/2 \approx h_0 + \frac{L\lambda^2}{\lambda^2 - d^2} \beta \\ + \left( L - \frac{Ld^3 \sqrt{d^2 - \lambda^2}}{(d^2 - \lambda^2)^2} \right) \theta_i + O(\beta^2 \theta_i + \beta \theta_i^2). \end{aligned} \quad (8.2)$$

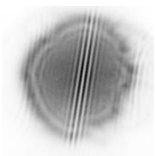


From this expression, it is clear that the effects of the two angles are independent up to the third-order Taylor terms, so that these effects can readily be mitigated. As  $\beta$  is a constant number for all apertures, the effect of the  $\beta$ -dependent term is to shift the center of mass position of all diffraction spots of a given wavelength by an equal amount. Therefore only the linear Zernike terms in the horizontal and vertical direction (tip and tilt, respectively) would be affected. By having multiple grating orientations in the SHM, the effect of this constant offset can be fully eliminated, as only the subset of apertures diffracting in the plane of rotation of  $\beta$  is affected by this offset. The presence of an angle  $\beta$  in either direction will therefore show up as a different tip/tilt measurement for both subsets of apertures, from which the offsets can be deduced and corrected for. As a result, spectrally-dependent variations in tip and tilt can be quantified with the SHM.

The  $\theta_i$ -term in Eq. 8.2 means that the center of mass position displaces more than the direct transmission in case of a local wavefront tilt along the grating diffraction direction. This effect needs to be corrected for to avoid a slight overestimation of the wavefront tilt. The size of this error depends only on known parameters and can be calculated to be  $\sim 0.5\%$  per degree wavefront tilt at a wavelength of 30 nm. It is therefore straightforward to correct for this effect by first performing a wavefront reconstruction, finding an initial value for  $\theta_i$ , and subsequently correcting the center of mass position using the term from Eq. 8.2. This correction could be performed in multiple iterations, but we find that one correction step suffices for an accurate wavefront reconstruction. Finally, the higher-order terms in Eq. 8.2 are found to be at least a factor  $10^3$  smaller than the linear terms and can be safely ignored.

## Wavefront reconstruction

The analysis of the SHM diffraction patterns yields a set of Hartmann spot patterns for all the individual harmonics. These patterns can then be compared to the reference structure to find a displacement for every aperture on the sensor. This comparison yields the gradient of the wavefront  $\nabla\phi(\vec{r}) = \Delta\vec{r}/L$ , in which  $\Delta r$  is the spot displacement with respect to the calibration. We characterized the reference pattern



at  $0.7 \mu\text{m}$  spatial resolution from an image of the SHM recorded by an optical microscope. This pattern is then rotated and centered with respect to the measured data.

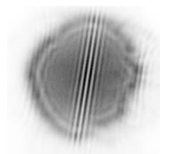
A calibration of the distance  $L$  is required for the analysis. To this end we recorded the SHM pattern from Krypton harmonics with the sensor placed at three different distances from the camera, with a precisely known displacement  $\Delta L$  between them. These images allowed calibration of the harmonic wavelengths from the measurement geometry (Fig. 8.4), upon which a consistent value for  $L$  could be retrieved. As an independent verification of the wavelengths of the different harmonics, spatially resolved Fourier-transform spectroscopy (FTS) [129] was used to measure the spectra of the individual spots on the camera. In our case where multiple harmonics are detected,  $L$  can in principle also be obtained from the spot separation of consecutive harmonics on the camera image, if the assumption of an equal frequency spacing of twice the driving laser frequency between harmonics holds. Because this equal-spacing-assumption is not exact, we find that this approach leads to a slightly less accurate wavelength and distance calibration. For the reconstructed wavefronts,  $L$  acts only as a scaling factor and does not influence the shape of the reconstructed wavefronts.

From the measured local wavefront tilts the total wavefront can then be reconstructed using a two-dimensional integration of the measured gradient. In order to do so, a bi-cubic spline interpolation is used to resample the data from the non-rectangular arrangement of subpupils to convert it to a rectangular grid. The complete wavefront is obtained by numerical integration of the gradient.

## 8.3 Wavefront characterization of a high-harmonic beam

### Wavefront reconstructions of individual harmonics

Figure 8.5 shows the reconstructed wavefronts for a range of nine harmonics generated in argon. To visualize these wavefronts and show their small features in addition to the curvature, they are displayed as how they would interfere with a plane wave. As the HHG beam



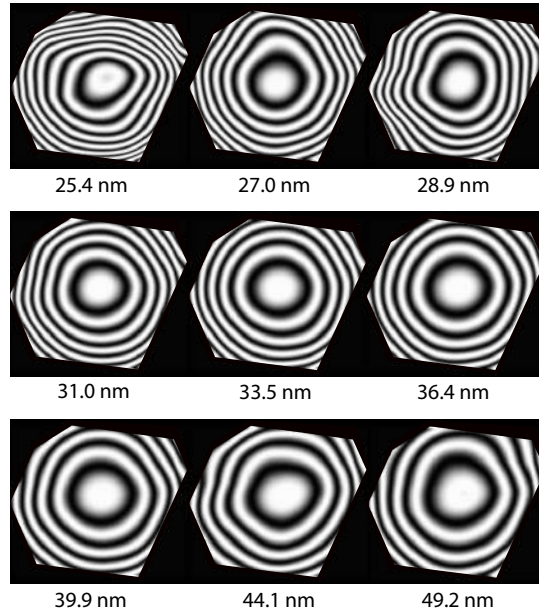


Figure 8.5: Reconstructed wavefronts for nine harmonics produced in argon, visualized by calculating their interference pattern with a plane wave. The center wavelength of the harmonic is indicated below each image.

undergoes free-space propagation from its generation point to the SHM, we measure a diverging beam with a significant spherical wavefront curvature. The brightest harmonics (33.5, 36.4 and 39.9 nm) appear to be nearly diffraction-limited, while the other harmonics show some deviations from an ideal spherical wavefront.

Because an uncertainty in the position of each aperture affects the final wavefront reconstruction in a different and complex way, we analyze the achieved wavefront accuracy by a Monte Carlo type analysis. From the center positions and uncertainties of the Gaussian fits of all the individual diffraction spots, we construct a distribution of Hartmann spot patterns that are all statistically consistent with the original measurement. We reconstruct wavefronts for all these spot patterns and compare the results. For the measurement shown in

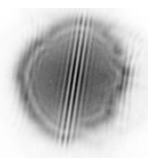


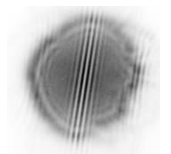
Fig. 8.5, we find a wavefront reproducibility better than  $\lambda/9$ . The result is more accurate for the brightest harmonics, which show an uncertainty of  $\lambda/32$ .

The information acquired from such a SHM measurement is not limited to wavefronts. Since each SHM aperture is a small transmission grating, a spectrum can be obtained for all apertures in the sensor. This enables a measurement of the linewidth of the harmonics as well as the spatial intensity distribution. Since a non-zero linewidth would result in elliptical spots, an accurate measurement of the linewidth can be made by fitting the spots with a 2D Gaussian that has different widths parallel and perpendicular to the diffraction direction. The width of each harmonic can then be extracted by deconvolution as  $\text{FWHM} = (\sigma_w^2 - \sigma_h^2)^{1/2}$ , where  $\sigma_w$  and  $\sigma_h$  are the  $1/e$ -widths in the parallel and perpendicular directions respectively. This analysis assumes that the Gaussian shape is appropriate for both the spectrum and the diffraction spot shape.

### Spectroscopic wavefront analysis

To quantify the wavefront aberrations we expand the retrieved wavefronts in terms of Zernike polynomials, including the lowest 11 polynomial terms from  $Z_0$  to  $Z_3$  and  $Z_4^0$  [169]. The unit circle on which the Zernike polynomials are defined has a diameter of  $740 \mu\text{m}$  and is chosen to fit within the region covered by the sensor apertures, ensuring accurate Zernike coefficients within this region.

Figure 8.6 shows a set of results from such a wavefront analysis in terms of Zernike polynomials over a range of detected harmonic wavelengths, for HHG produced in both argon and krypton. As discussed above, the SHM provides some information about spectral parameters such as the linewidth of the harmonics, which is displayed in Fig. 8.6(a). At shorter wavelengths the harmonics are more broadband, and we observe broader harmonics in krypton than in argon. The harmonics in krypton also appear slightly blue-shifted (Fig. 8.6(e)), which together with the broader harmonics is indicative of the rather high intensity used for HHG in krypton. Figure 8.6(b) shows the root-mean-square (RMS) deviation of the wavefronts from a perfect spherical shape, which can be viewed as a measure of the deviations from a diffraction-



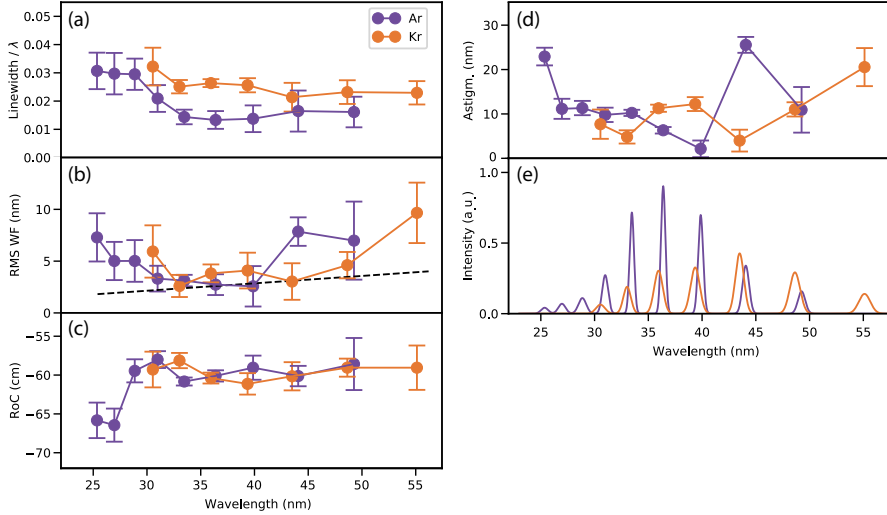
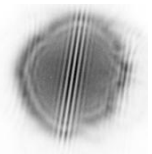


Figure 8.6: Wavelength-dependence of several beam parameters retrieved from a SHM measurement on high-harmonics produced in Ar and Kr. All error bars constitute one standard deviation. (a) Linewidth of individual harmonics. (b) RMS deviation of the wavefronts from a spherical wave. The Marechal-criterion of  $\lambda/14$  is indicated by a dashed line. (c) Radius of curvature (RoC) of the respective HHG wavelengths. (d) Astigmatism magnitude as calculated from the Zernike terms. (e) Reconstructed HHG spectra, normalized to the brightest argon line. The krypton spectrum is scaled by a factor of 2 in intensity for visibility purposes.

limited wavefront. Within the measurement accuracy, the wavefront deviations are found to be either at, or slightly above, the Marechal criterion of  $\lambda/14$  (dashed line), indicating that the EUV beams are in general close to diffraction-limited.

While the strongest harmonics appear close to diffraction-limited, stronger wavefront aberrations are observed for the weaker harmonics. As an example, Fig. 8.6(d) shows the magnitude of astigmatism, calculated as the root mean square of the  $Z_2^{+2}$  and  $Z_2^{-2}$  Zernike terms corresponding to straight and diagonal astigmatism. We found astigmatism



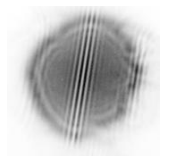
to form the main contribution to the wavefront deviations observed in Fig. 8.5, although there are small amounts of coma and trifolium present in the wavefronts as well.

One further parameter which is of interest is the radius of curvature (RoC) of the spherical wavefront component of the individual harmonics, as it has previously been reported that there can be a variation of the apparent focal distance with high-harmonic number [161]. Retrieving the RoC from the SHM data involves a combination of the defocus, spherical aberration and astigmatism Zernike terms [169]. From our measurement data, the observed radii of curvature (Fig. 8.6(c)) roughly match the source-to-mask distance of 60 cm, but no clear trend can be observed. This may be attributed to different phase-matching conditions in the high-harmonic generation. At the shortest wavelengths a deviation towards longer RoC is retrieved, although the error bars for these low-intensity harmonics also increase significantly.

#### Detection of HHG pulse front tilts

A remarkable feature of the SHM is the ability to measure relative wavefront tilts between the individual harmonics. Especially for ultrafast pulsed sources, the ability to measure tilts allows a characterization of spatiotemporal coupling such as pulse front tilts, and associated effects such as the attosecond lighthouse effect [163], [164]. Since a wavefront tilt leads to a constant displacement of all spots on the camera, an accurate tilt measurement can only be performed with a Hartmann sensor if the exact position of the reference grid with respect to the camera is calibrated. For the SHM, an absolute wavefront tilt can in principle be determined if an accurate calibration of  $\beta$  is performed. Such a calibration would require measurements of at least two collinear monochromatic beams with different wavelengths and is challenging to perform, while the physical significance of an absolute tilt measurement is limited.

Knowledge of a possible relative tilt between different harmonics is relevant for many ultrafast experiments, as it constitutes a spatial chirp, which is equivalent to a tilt of the pulse front. Such a spatial chirp can modify the outcome of experiments that are sensitive to space-time coupling of ultrashort pulses. In a SHM wavefront measure-



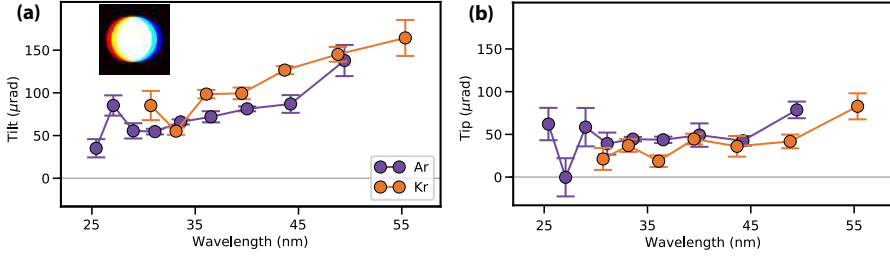
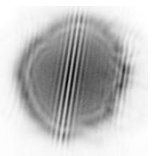


Figure 8.7: Measured relative wavefront tilt in the horizontal (tilt, (a)) and vertical (tip, (b)) directions as a function of wavelength, retrieved from the SHM analysis, for HHG produced in argon and krypton with 810 nm fundamental wavelength. A significant wavelength-dependent wavefront tilt in the horizontal plane (tilt) is observed, indicating the presence of a spatial chirp of the HHG beam as schematically drawn in the inset to (a).

ment, we can use any of the detected harmonics as reference. Because in a SHM measurement the wavefronts of all harmonics are measured simultaneously in a common geometry, the relative difference in tip and tilt for different harmonics can readily be measured.

In this analysis the effect of a possible camera tilt needs to be included. As already discussed before with Eq. 8.2, a camera tilt along the diffraction direction leads to an additional displacement of the center-of-mass positions that needs to be corrected to obtain correct spot positions for wavefront reconstruction. Since the displacement perpendicular to the grating direction is only sensitive to the wavefront tilt, an SHM containing gratings with two different directions can directly isolate this effect and measure the actual wavefront tilt relative to the reference wavelength.

In this way we extract relative wavefront tilts for the individual high-harmonics produced in argon and krypton. The resulting wavefront tilt and tip are shown in Figs. 8.7(a) and 8.7(b). We find wavefront-tilt variations up to 0.1 mrad across our full HHG spectrum. In comparison, the divergence of the high harmonic beams is approximately 1 mrad, which means that even though the individual harmonics remain largely overlapped, there is a spectral variation and associated

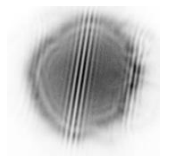


pulse front tilt in the HHG beam. We observe similar pulse front tilts in argon and krypton, indicating that this tilt is most likely due to a pulse front tilt in the driving laser beam [163], [164]. This is to be expected, as the employed beam path contains some birefringent components with a slight intentional misalignment in the horizontal direction [129]. Similar geometries have been used to intentionally induce strong tilts in the HHG beam, leading to the attosecond lighthouse effect [164]. The SHM provides a sensitive measurement device to quantify the presence of even small tilts, aiding the alignment and optimization of broadband HHG wavefronts and spatiotemporal couplings.

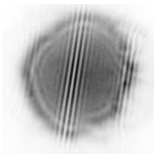
## 8.4 Conclusions

In summary, we have demonstrated a spectrally-resolved single-shot wavefront sensor for broadband high-harmonic beams. To achieve this capability, we designed a specific Hartmann mask that incorporates transmission gratings to acquire wavefront measurements of the individual harmonics. A detailed analysis of a single measured pattern provides information on harmonic wavefronts, relative intensities, and spectral linewidths. Given sufficient sensitivity and incident flux, this information can in principle be retrieved for individual HHG pulses, rather than for an average over many shots. This feature opens up the prospect of detecting shot-to-shot variations of HHG beams, which has already been shown to be important information for sensitive experiments [170].

The calibration procedure of the SHM is not more complicated than for a conventional Hartmann sensor, as only the SHM-camera distance and the orientation of the mask need to be determined, and we have shown that these parameters can even be achieved from a wavefront measurement in a self-consistent manner, if several harmonics are present in the beam. Although the current work demonstrates spectrally resolved wavefront measurements for wavelengths between 25 and 50 nm, this technique is not limited to these wavelengths. By changing the SHM design parameters such as the grating pitch and distance to the camera, the SHM method can be extended to wavelengths ranging from soft x-rays to infrared. By further refining the analysis



procedure, it may be possible to extend the SHM technology to the characterization of more complex or partially continuous spectra.



# Intrinsic wavefront variations in gas-cell-based high-harmonic generation

## 9.1 Chromatic wavefront variation of high harmonics

The spectrally resolved Hartmann sensor described in chapter 8 is uniquely suited to measure wavelength-dependent differences in the wavefront. There are various reasons why such a chromatic wavefront variation may arise. For visible and near-infrared wavelengths, refractive lenses are a well-known cause of chromatic dispersion. The reason is that the refractive index depends on the wavelength, which means that the strength of a lens becomes wavelength-dependent.

Extreme-ultraviolet light is normally focused with reflective optics or with diffractive optics such as Fresnel zone plates. Of these, the former are completely achromatic, while diffractive optics have such extreme chromatic aberration that they are not employed for broadband radiation at all.

That is not to say that at EUV wavelengths, chromatic effects are of no concern. In fact, the HHG-process used to generate broadband EUV radiation can itself be a cause of chromatic aberration. Around the same time that the spectrally resolved Hartmann sensor was developed, H. Wikmark and coworkers from the group of Anne L'Huillier



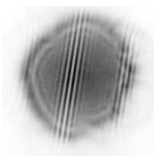
at Lund University predicted that optimized HHG produces EUV with significant spatio-temporal coupling (STC) [171]. In short, this implies that the electric field of the lightwave cannot be expressed as the product of a spatial wave profile and a temporal wave profile. STC can appear in many forms, but the predicted STC [171] is very similar to the chromatic aberration produced by chromatic lenses in the visible domain.

Spatio-temporal coupling in HHG beams has several implications. Using reflective optics, it will be hard or impossible to focus all spectral components to a spot of the same size. For high-precision multi-wavelength EUV metrology, an accurate measurement of the wavelength-dependent wavefront variation will enable correction for errors induced by this variation. Furthermore, the field of attosecond physics is driven by ultrashort HHG pulses. It is often necessary to focus the attosecond pulses for maximum intensity. Wikmark *et al.* predict that the STC leads to significant pulse stretching in the focus of an HHG beam, and indicate that there may be a trade-off between pulse duration and generation efficiency.

In particular, Wikmark *et al.* predict that the wavelength-dependent wavefront of high harmonics is related to the exact generation geometry [171]. They provide a model and simulations for the chromatic dispersion as a function of distance between the gas cell and the focus of the driving laser. Shortly after the publication of Chapter 8 describing the spectral Hartmann mask (SHM), we therefore started a scientific collaboration with the Lund team, aiming to measure the predicted spatio-temporal coupling.

## 9.2 The Lund high-power EUV beamline

To show the presence of chromatic aberration in HHG, we used the high power beamline at the Lund University Laser Centre. This laser provides up to 100 mJ pulses at 10 Hz, with a pulse duration of 40 fs and center wavelength 800 nm [156]. To achieve the correct intensity for HHG, these pulses are focused with an 8-meter focal length mirror into a 1-cm-long gas cell. The exact focal point is controlled with a deformable mirror, enabling controlled scanning of the focus position.



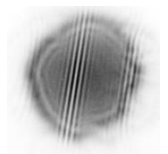
In addition, the high pulse energy of this system makes it an ideal target to explore the limits of single-shot wavefront measurements. This was identified as a secondary goal of the experiment.

After the HHG gas cell, the beam freely propagates over 4 meters before reaching the first EUV optics. Over this distance, the high harmonics diverge from a roughly 200  $\mu\text{m}$  beam to roughly 800  $\mu\text{m}$ . At that point, a gold-coated mirror at 45° angle of incidence is used to reflect the high harmonics into the measurement chamber. This mirror can be taken out of the beam path to let the EUV propagate to a set of other experimental chambers, which includes a grating spectrometer that can be used to monitor the EUV spectrum.

The wavefront measurement relies on accurate detection of the diffraction from the Hartmann mask. As the CCD camera is roughly equally sensitive to infrared and EUV, it is important to effectively block the remaining fundamental radiation. The main method of IR rejection is a 200 nm thin aluminum foil, which transmits EUV while the infrared is reflected. The infrared transmission of such an aluminum foil is typically less than  $10^{-9}$  [172]. This level of rejection is necessary given the low conversion efficiency of HHG. It should be noted however that the infrared power is close to a level where it may damage the aluminum foil. Therefore, additional IR rejection is necessary before the aluminum foil. This is achieved by a pair of fused-silica plates at 10° grazing incidence, placed before the gold mirror. The plates are anti-reflection coated for infrared radiation while still reflecting EUV. This reduces the on-axis IR power roughly by four orders of magnitude, while the EUV loss is less than 50%.

The rejected infrared light can still pose a problem as it scatters and reflects around the vacuum chambers. In order to reject off-axis background light, the beam passes through a 10 cm long tube between the mirror chamber and the measurement chamber. The entrance and exit of this tube are reduced to 5 mm apertures using thick aluminum foil. The aluminum filter is placed directly after the exit of the tube.

The actual wavefront measurement setup consists of an in-vacuum CCD camera and a three-dimensional translation stage to position the spectral Hartmann mask. The distance between the camera and sensor can be varied between 1 and 3 cm. This is important as it enables to match the detection geometry to the detected EUV spectrum, mini-



mizing overlap between diffraction spots. Finally, more aluminum foil is used to ensure that only diffracted light from the spectral Hartmann mask reaches the camera.

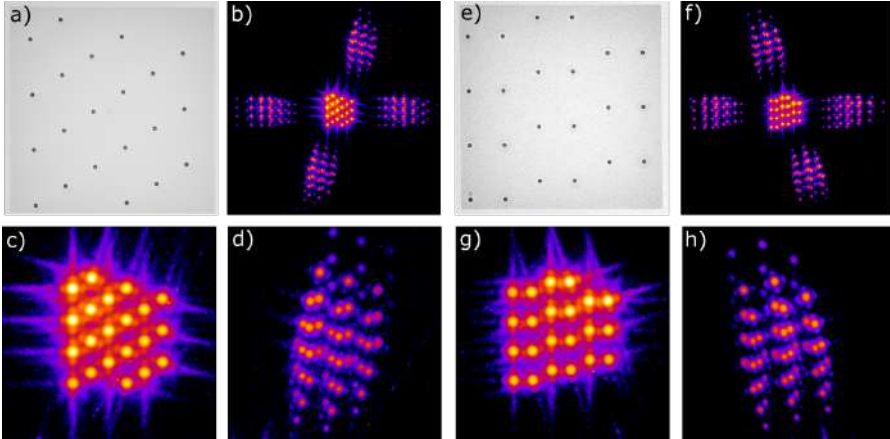
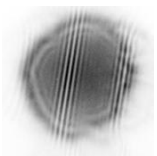


Figure 9.1: Overview of the wavefront sensors and example measurement data. **a**: SEM image of the first wavefront sensor with the original design. **b**: Corresponding measurement data taken with the high power EUV beamline in Lund. **c** and **d**: Zoom-in on the direct transmission and one first order of diffraction of the measurement shown in panel **b**. **e**: SEM image of the new design. **f**: Corresponding measurement data, for the same EUV beam as in **b**. **g** and **h**: Zoom-in on the direct transmission and one first order of diffraction of the measurement shown in panel **f**.

The sample holder contains three 3 mm sample apertures. One of these apertures is left open to facilitate a direct view of the EUV beam, and spectral Hartmann masks are placed in the other two. Of these, the first mask uses the same design (Fig. 8.2) as the original sensor. The other sensor uses a slightly different design with larger spot separation and one extra aperture. With two different sensors, it is possible to verify that the sample design does not influence the measured wavefront. A comparison of SEM images and example measurements for the two sensors is given in Fig. 9.1.



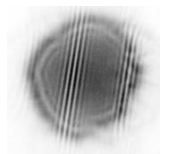
### 9.3 Measurement analysis

Similar to a traditional Hartmann wavefront sensor [152], the SHM measures spot displacements that are proportional to the wavefront gradient. In order to calculate the gradient from the measured spot displacements, the exact distance to the camera has to be known. Therefore, we performed a distance calibration by measuring the SHM diffraction pattern for a range of different camera distances. The relative distance between these positions is known to micron-level accuracy from the translation stage itself. By measuring the spacing between the +1<sup>st</sup> and -1<sup>st</sup> diffraction orders as a function of SHM-camera distance and extrapolating to their zero crossing position, the exact mask-to-camera distance is determined. After this distance calibration, the mask-to-camera distance was set to 18.9 mm, which yielded good quality Hartmann patterns.

A limitation of the experimental setup in Lund was the height of the beam path. As a result, it was not possible to align the beam to be horizontal at the wavefront sensor, leading to an angle of incidence (AOI) on the SHM of roughly 2 degrees. As explained in Section 8.2, the non-zero angle of incidence leads to a shift of the center of mass of the +1<sup>st</sup> and -1<sup>st</sup> diffraction orders, which exceeds the geometrical shift induced by the different AOI. This shift depends on the angles involved, the wavelength and the grating direction. The different grating subsets of the SHM therefore get a different shift.

In order to correct for the AOI-induced shift, the different grating subsets are considered individually. For each of these, the spot displacements are extracted for the center of mass of the first diffraction orders of all high harmonics, as well as for the zeroth order. Since the zeroth order does not suffer from the AOI-induced shift, it can act as a reference for the first orders of diffraction. The spot displacements are averaged over all the apertures of a single grating direction for a single wavelength. This average displacement is then compared to the average displacement measured in the zeroth orders of those apertures, which yields the AOI-induced shift for that grating direction and wavelength combination. This procedure is performed for all combinations of aperture subsets and HHG wavelengths.

The resulting list of AOI-induced shifts can then be used to correct



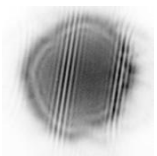
the spot displacements as extracted from the first orders of diffraction. The elimination of the AOI-induced shift unfortunately rules out the possibility to measure the average wavefront tilt of individual high harmonics. However, the determined tilts can also be used to correct for other measurements performed in the same alignment. It is therefore still possible to distinguish a relative change in wavefront tilt between two different measurements.

### 9.4 Preliminary results

The measurements for this joint research activity were performed over the course of one week, and data analysis was mostly performed in the weeks following the experiment. After the initial alignment and wavefront measurement tests, three main measurement series were taken: one measurement in which the focus position was varied in small steps, one measurement in which the focus position and gas pressure were varied, and finally a similar measurement in which xenon was used instead of argon to achieve a larger flux in order to enable single-shot wavefront measurements.

In the first measurement, the wavefront was measured as a function of focus position relative to the gas cell. For this measurement, a 10 mm gas cell was chosen as the generation medium, and the pressure was optimized to achieve a stable, Gaussian beam profile. The short gas cell is important as the model assumes a constant wavefront curvature throughout the generation medium. This is an important parameter in the physical model. On the other hand, the gas cell is also long enough for significant HHG flux to build up. The focus position was stepped through 23 steps using the voltage-controlled deformable mirror. The center position of this scan, for which the HHG was aligned, is measured three times: before, during and after the scan.

At each measurement position, a wavefront measurement averaged over 600 laser shots was measured. In addition, 25 single-shot beam intensity patterns are measured, as well as five wavefront measurements averaged over 10 shots. These measurements provide extra information regarding the stability of the beam. Combining the measured beam intensity patterns with the retrieved wavefront provides the complex



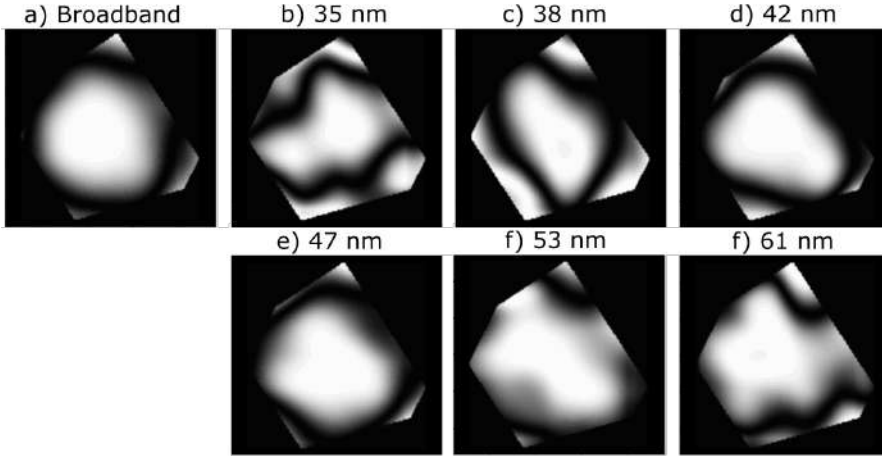
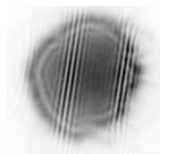


Figure 9.2: Examples of the reconstructed wavefronts obtained in the first measurement series, visualized as the interference pattern with a perfect plane wave. Wavefront **a** is obtained from the zeroth order transmission while **b** to **f** are obtained from the first orders of diffraction.

electric field, which can be used to reconstruct the beam at the HHG generation position.

An example of the set of reconstructed wavefronts for a 600-shot exposure is shown in Fig. 9.2. From this example, it is clear that the total wavefront curvature at the wavefront sensor is quite small. The total peak to valley distance in the wavefronts is less than 100 nm. This follows from the long distance between the source and sensor. Furthermore, there are clear differences in the wavefront between high harmonics.

To quantify the wavefront information, it is decomposed into Zernike polynomials. The distance to the focus can then directly be calculated from the Zernike focus term. Fig. 9.3 shows the extracted focus distance for the 600-shot measurements. From these results, several conclusions can be drawn. First, the error margins on the broadband wavefronts are significantly smaller than those for the individual harmonics. This is related to the lower flux in the diffraction



## 9. INTRINSIC WAVEFRONT VARIATIONS IN GAS-CELL HHG

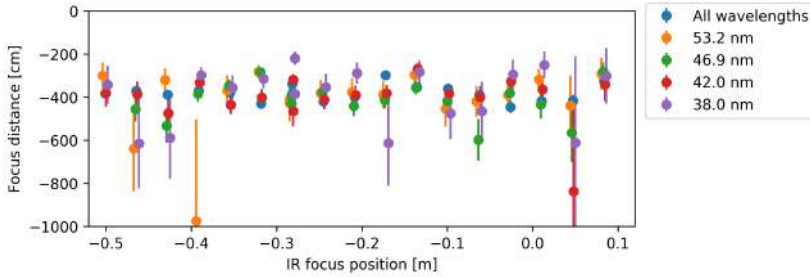
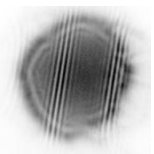


Figure 9.3: Focus distances retrieved from the first measurement series for the average broadband beam and four individual high harmonics. Negative infrared focus positions indicate a focus after the gas cell. Four measurements near the IR focus position of  $-0.6$  m and one at  $0.15$  m are not shown because these have significantly larger error margins resulting from the low HHG flux at these positions.

of the SHM. In the center of the scan, at optimal HHG, the diffracted signal strength ranges between 100 to 3000 counts per pixel, while the standard deviation of the background counts is roughly 8 counts. The direct transmission typically has an order of magnitude more counts. Towards the edges of the focus scan the HHG flux decreases strongly, leading to weaker signals and larger error margins.

Another consideration for the relatively large error margins follows from the long distance between source and sensor. The measured focus distance is proportional to the inverse of the wavefront curvature. Due to the long distance, the curvature is very small. The error margin on the curvature is determined by the signal strength and does not depend on distance. The relative error is therefore larger at longer distances. Unfortunately, we were unable to find a direct correlation with the theory in the results of the first measurement series (Fig. 9.3). In part, this is caused by large error margins, and for another part due to the large shot-to-shot variation. There is no obvious trend visible in the data.

In the second measurement series, both the gas pressure in the cell and the focus position were varied. At higher pressures, the phase matching contributions of both the neutral gas and of the plasma will



increase. In addition, self-focusing and guiding of the driving pulse can occur, altering the wavefront of the fundamental. All of these processes can alter the wavefronts of the high harmonics.

The pressure was varied in five steps between the lowest pressure where a measurable HHG signal is observed to the maximal pressure that could be achieved with the system. Although no absolute gas pressure measurements could be taken, a measurement of the vacuum pressure indicates that the high pressure was roughly 20 times higher than the lowest pressure. The focus position was scanned in five large steps covering the same range as for the first series. Similar to the first series, at each position a 600-shot wavefront measurement was taken, as well as single-shot intensity profiles. Analysis of these results showed neither the expected wavefront variation as a function of focus position nor a significant wavefront change with gas pressure.

Finally, the third measurement series was measured using xenon, as this provides a slightly larger flux. This enabled the recording of single-shot wavefront measurements, while the averaged measurements provide the same information as in the previous series. Using a triggered wavefront sensor, infrared wavefronts were recorded simultaneously with the single-shot HHG wavefronts. In addition, a camera was used to measure the IR focus shape and position. With this data, it is possible to correlate EUV wavefront properties with driving beam properties such as focus position, wavefront aberration and pulse intensity.

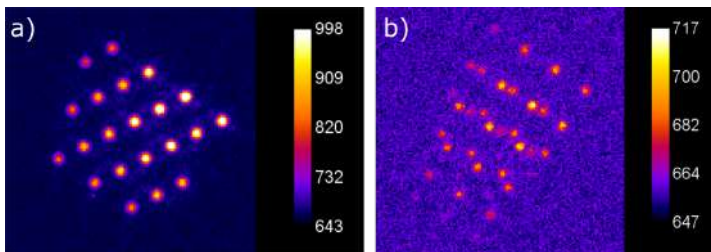
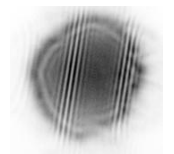


Figure 9.4: **a**: Zoom-in on the SHM direct transmission of a single-shot xenon wavefront measurement. **b**: Zoom-in on one of the corresponding first orders of diffraction.



## 9. INTRINSIC WAVEFRONT VARIATIONS IN GAS-CELL HHG

For this measurement series, the focus position was stepped over eight positions. At each position, 40 wavefront measurements were performed as well as 40 intensity profile measurements. Every time, the beam was blocked during one of the 40 shots. With this dark shot, it is possible to check the synchronization with the infrared wavefront sensor and in-focus camera. Close-ups of typical wavefront measurements are shown in Fig. 9.4.

As a first step in the analysis of this data, the single-shot wavefront measurements were averaged to yield long-exposure wavefront measurements with decent signal strength. This provides a measurement of the EUV wavefront as a function of focus position for HHG in xenon, similar to the first measurement series. The results of this averaged scan are shown in Fig. 9.5. Contrary to the results obtained in argon,

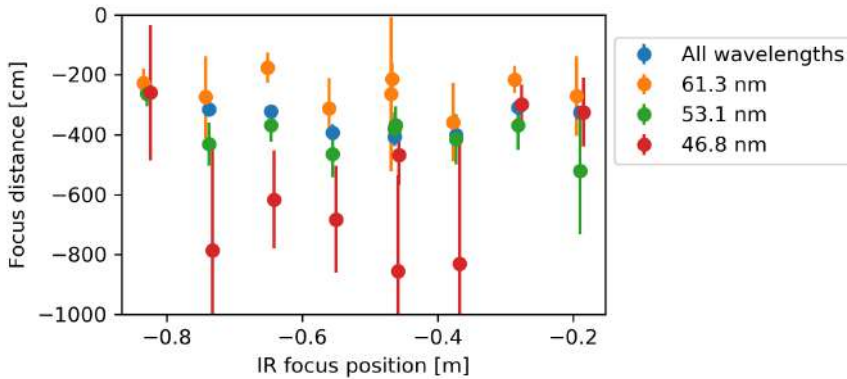
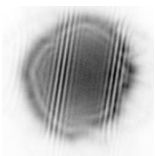


Figure 9.5: EUV focus distances measured as a function of infrared focus position relative to the xenon gas cell. Each wavefront measurement is averaged over 40 laser shots. The infrared focus position is given in Rayleigh ranges, negative indicating a focus after the gas cell.

a trend can be seen in the xenon wavefront data. Despite the large error margins, Fig. 9.5 shows that the longer wavelengths are generated closer to the wavefront sensor than the short wavelengths. There also seems to be a focus-position dependence to this behavior, as it is not



visible at the edges of the scan. The wavefront simulations show a similar feature, shown in Fig 9.6. However, the predicted effect is much smaller and depends differently on wavelength. Furthermore, it should be noted that these simulations only take the short HHG trajectories in account. A separate analysis of the long trajectories shows a different behaviour.

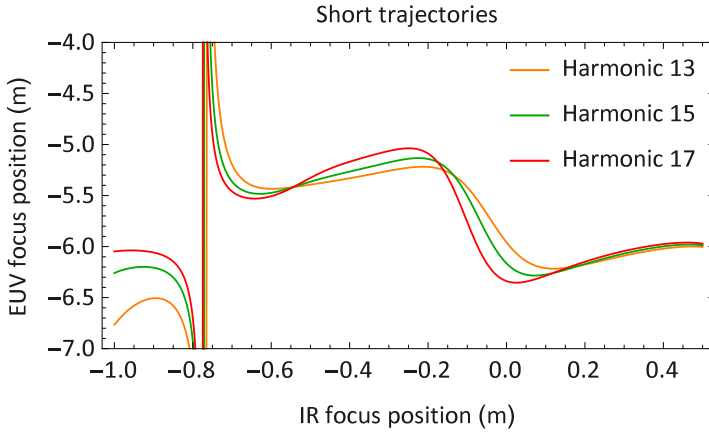
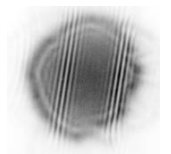


Figure 9.6: Simulation provided by H. Wikmark showing the EUV focus distances as a function of infrared focus position relative to the xenon gas cell. The simulation considers short trajectories only.

For the analysis of the single-shot wavefront measurements, a small adjustment has been made in the process. Due to the low signal to noise, the Gaussian fitting procedure is unable to fit all spots accurately. Therefore, the algorithm first fits the direct transmission spots. An intensity threshold is then applied to select only those apertures which are sufficiently illuminated. This varies from shot to shot due to beam pointing variations. If at least eight apertures are illuminated, the measurement is then further processed.

Based on this analysis, the EUV wavefront parameters can then be compared to the single-shot infrared wavefront parameters. In Fig. 9.7, the Zernike focus terms for infrared and EUV are correlated. For the presented data, the infrared focus was set for optimal high harmonic generation. Although a correlation between the focus terms might be



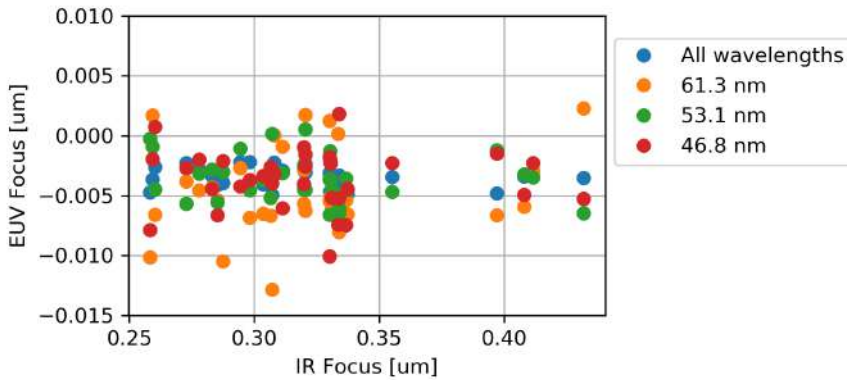


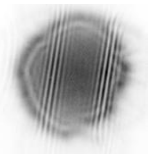
Figure 9.7: Correlation plot of the EUV Zernike focus terms with the infrared Zernike focus term. For clarity, the error margins of the EUV focus values are not plotted but range typically from 2 to 5 nm.

expected from first principles, no such correlation is observed. For both the EUV and IR data, a wide variation is observed.

## 9.5 Outlook

While the xenon data provides a hint that some effect can be measured, the results of our first measurements are obscured by noise. In order to validate the simulation predictions, it is therefore necessary that the signal-to-noise ratio of the EUV wavefront measurement is significantly improved. This can be done both by reducing the noise level and by increasing the strength of the expected signal.

There are two main contributions to the error margins on the Zernike terms. These are the precision with which the spot positions can be determined through least-squares fitting and the number of apertures contributing to the wavefront measurement. The fitting precision is directly related to the signal quality on the camera, which is determined by the camera readout, EUV intensity and background level. During the experiment, the camera was already cooled to  $-50\text{ }^{\circ}\text{C}$ , optimizing the readout. Therefore, longer exposures to increase the



EUV signal and improved infrared rejection are the most promising means to increase fitting accuracy. It is conceivable that the signal-to-noise ratio of the raw data can be improved by one or two orders of magnitude.

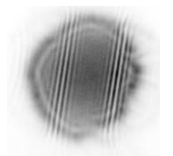
The number of apertures in the SHM is limited by the need to clearly separate the diffraction of all spots. There is, however, space for a third set of apertures with a different diffraction direction. This would lead to six lobes of diffraction orders, making more efficient use of the camera. The apertures can be placed between the existing apertures, keeping the wavefront sensor matched to a beam size that is typically 1 mm. This results in 50% more apertures, which will allow for a better wavefront reconstruction precision. For a wavefront consisting only of a focus term, each unique pair of apertures provides a single measurement of the focus term. A SHM sensor with  $n$  apertures therefore provides  $n(n-1)$  measurements. Assuming equal error margins for all these measurements, the total precision of the focus measurement with  $n$  apertures scales with  $1/\sqrt{n(n-1)}$ . Consequently, a 50% increase in apertures leads to a roughly 50% reduction of the error margins. The actual improvement will be slightly different as the individual measurements will have differing error margins. This is the case because each measurement needs to be weighed by the aperture separation and corrected for the signal-to-noise level at the apertures.

Finally, it is important to take the expected signal strength into account. Consider two individual high harmonics, appearing to emerge as perfect spherical waves from  $-dz$  before and  $+dz$  after the infrared focus. The difference between the two wavefronts can then be calculated to be approximately

$$\delta\Phi(x) \approx \frac{dz}{z^2}x^2, \quad (9.1)$$

in which  $x$  is the position in the sensor plane, and  $z$  is the distance between sensor and the infrared focus. The spot displacement measured by the SHM is given by the gradient of the wavefront. The difference in spot displacement for the two spherical waves is then

$$\nabla\delta\Phi(x) \approx 2\frac{dz}{z^2}x. \quad (9.2)$$



As this scales with  $1/z^2$ , it follows that the expected signal is much stronger when the sensor is placed closer to the source. The range  $x$  over which this is measured is given the wavefront sensor size or the beam size, depending on which of the two is smaller. In the situation where the beam size is limiting,  $x$  is proportional to  $z$ , and the increase in signal is limited to scale with  $1/z$ .

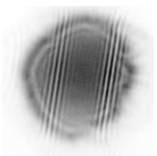
It is however not possible to place the SHM arbitrarily close to the source. Before the SHM, it is still necessary to filter out the infrared. The thin aluminum foils used for this purpose can melt due to the high incident power levels. To avoid such damage the laser energy needs to be distributed over a sufficiently large area, resulting in a minimum distance requirement between filter and source.

The minimum sensor distance can be expressed as a multiple  $m$  of the Rayleigh range  $z_R$  of the beam. The strength  $dz$  of the chromatic aberration scales with the Rayleigh range. In this situation, Eq. 9.2 can be rewritten as

$$\nabla\delta\Phi(x) \propto 2\frac{1}{m^2z_R}x. \quad (9.3)$$

It follows that the signal strength is proportional to  $1/z_R$ . This relations shows that the expected effects can be more easily measured for a tightly focused beam with a short Rayleigh range. Of course, a shorter Rayleigh range also necessitates the use of a shorter generation medium. This may be difficult to achieve and may yield lower HHG flux.

Concluding, an experiment that optimizes the sensitivity for the wavefront curvature variations should be based on a high-repetition rate laser source focused tightly in a short generation medium. This can be a short gas cell or a thin gas jet. As close as possible to the source, an aluminum filter must be used to block the driving laser. AR-coated silica plates can be useful to achieve sufficient IR power reduction sooner, enabling the aluminum filter to be closer to the source. Finally, a modified SHM wavefront sensor should be placed close after the aluminum filter.



# Bibliography

- [1] A. Lipson, S. G. Lipson, and H. Lipson, *Optical Physics*. Cambridge University Press, Oct. 2010.
- [2] G. E. Moore, „Cramming more components onto integrated circuits”, *Electronics*, pp. 114–117, 1965.
- [3] E. Ruska, „The development of the electron microscope and of electron microscopy”, *Rev. Mod. Phys.*, vol. 59, no. 3, pp. 627–638, Jul. 1987.
- [4] G. Binnig and H. Rohrer, „Scanning tunneling microscopy — from birth to adolescence”, *Rev. Mod. Phys.*, vol. 59, no. 3, pp. 615–625, Jul. 1987.
- [5] E. Betzig, G. H. Patterson, R. Sougrat, O. W. Lindwasser, S. Olenych, J. S. Bonifacino, M. W. Davidson, J. Lippincott-Schwartz, and H. F. Hess, „Imaging Intracellular Fluorescent Proteins at Nanometer Resolution”, *Science*, vol. 313, no. 5793, pp. 1642–1645, Sep. 2006.
- [6] M. Uchida, G. McDermott, M. Wetzler, M. A. L. Gros, M. Myllys, C. Knoechel, A. E. Barron, and C. A. Larabell, „Soft X-ray tomography of phenotypic switching and the cellular response to antifungal peptoids in *Candida albicans*”, *PNAS*, vol. 106, no. 46, pp. 19 375–19 380, Nov. 2009.
- [7] W. Chao, J. Kim, S. Rekawa, P. Fischer, and E. H. Anderson, „Demonstration of 12 nm Resolution Fresnel Zone Plate Lens based Soft X-ray Microscopy”, *Opt. Express*, vol. 17, no. 20, pp. 17 669–17 677, Sep. 2009.
- [8] H. N. Chapman and K. A. Nugent, „Coherent lensless X-ray imaging”, *Nat. Photonics*, vol. 4, no. 12, pp. 833–839, Dec. 2010.

- [9] J. Miao, P. Charalambous, J. Kirz, and D. Sayre, „Extending the methodology of X-ray crystallography to allow imaging of micrometre-sized non-crystalline specimens”, *Nature*, vol. 400, no. 6742, pp. 342–344, Jul. 1999.
- [10] S. Marchesini, H. N. Chapman, S. P. Hau-Riege, R. A. London, A. Szoke, H. He, M. R. Howells, H. Padmore, R. Rosen, J. C. H. Spence, and U. Weierstall, „Coherent X-ray diffractive imaging: applications and limitations”, *Opt. Express*, vol. 11, no. 19, pp. 2344–2353, Sep. 2003.
- [11] J. R. Fienup, „Reconstruction of an object from the modulus of its Fourier transform”, *Opt. Lett.*, vol. 3, no. 1, pp. 27–29, Jul. 1978.
- [12] D. Sayre, „Some implications of a theorem due to Shannon”, *Acta Crystallogr.*, vol. 5, no. 6, pp. 843–843, Nov. 1952.
- [13] V. Elser, „Phase retrieval by iterated projections”, *JOSA A*, vol. 20, no. 1, pp. 40–55, Jan. 2003.
- [14] J. C. H. Spence, U. Weierstall, and M. Howells, „Coherence and sampling requirements for diffractive imaging”, *Ultramicroscopy*, vol. 101, no. 2, pp. 149–152, Nov. 2004.
- [15] B. Abbey, L. W. Whitehead, H. M. Quiney, D. J. Vine, G. A. Cadenazzi, C. A. Henderson, K. A. Nugent, E. Balaur, C. T. Putkunz, A. G. Peele, G. J. Williams, and I. McNulty, „Lensless imaging using broadband X-ray sources”, *Nat. Photonics*, vol. 5, no. 7, pp. 420–424, Jul. 2011.
- [16] H. M. Quiney, A. G. Peele, Z. Cai, D. Paterson, and K. A. Nugent, „Diffractive imaging of highly focused X-ray fields”, *Nat. Phys.*, vol. 2, no. 2, p. 101, Feb. 2006.
- [17] H. N. Chapman, A. Barty, M. J. Bogan, S. Boutet, M. Frank, S. P. Hau-Riege, S. Marchesini, B. W. Woods, S. Bajt, W. H. Benner, R. A. London, E. Plönjes, M. Kuhlmann, R. Treusch, S. Düsterer, T. Tschentscher, J. R. Schneider, E. Spiller, T. Möller, C. Bostedt, M. Hoener, D. A. Shapiro, K. O. Hodgson, D. v. d. Spoel, F. Burmeister, M. Bergh, C. Caleman, G. Huldtt, M. M. Seibert, F. R. N. C. Maia, R. W. Lee, A. Szöke, N. Timneanu,

- and J. Hajdu, „Femtosecond diffractive imaging with a soft-X-ray free-electron laser”, *Nat. Phys.*, vol. 2, no. 12, p. 839, Dec. 2006.
- [18] A. McPherson, G. Gibson, H. Jara, U. Johann, T. S. Luk, I. A. McIntyre, K. Boyer, and C. K. Rhodes, „Studies of multiphoton production of vacuum-ultraviolet radiation in the rare gases”, *JOSA B*, vol. 4, no. 4, pp. 595–601, Apr. 1987.
- [19] P. Corkum, „Plasma perspective on strong field multiphoton ionization”, *Phys. Rev. Lett.*, vol. 71, no. 13, pp. 1994–1997, Sep. 1993.
- [20] R. Zerne, C. Altucci, M. Bellini, M. B. Gaarde, T. W. Hänsch, A. L’Huillier, C. Lyngå, and C.-G. Wahlström, „Phase-Locked High-Order Harmonic Sources”, *Phys. Rev. Lett.*, vol. 79, no. 6, pp. 1006–1009, Aug. 1997.
- [21] M. Bellini, C. Lyngå, A. Tozzi, M. B. Gaarde, T. W. Hänsch, A. L’Huillier, and C.-G. Wahlström, „Temporal Coherence of Ultrashort High-Order Harmonic Pulses”, *Phys. Rev. Lett.*, vol. 81, no. 2, p. 297, Jul. 1998.
- [22] R. A. Bartels, A. Paul, H. Green, H. C. Kapteyn, M. M. Murnane, S. Backus, I. P. Christov, Y. Liu, D. Attwood, and C. Jacobsen, „Generation of Spatially Coherent Light at Extreme Ultraviolet Wavelengths”, *Science*, vol. 297, no. 5580, pp. 376–378, Jul. 2002.
- [23] X. F. Li, A. L’Huillier, M. Ferray, L. A. Lompré, and G. Mainfray, „Multiple-harmonic generation in rare gases at high laser intensity”, *Phys. Rev. A*, vol. 39, no. 11, pp. 5751–5761, Jun. 1989.
- [24] J. Rothhardt, G. K. Tadesse, W. Eschen, and J. Limpert, „Tabletop nanoscale coherent imaging with XUV light”, *J. Opt.*, vol. 20, no. 11, p. 113 001, Oct. 2018.
- [25] D. F. Gardner, M. Tanksalvala, E. R. Shanblatt, X. Zhang, B. R. Galloway, C. L. Porter, R. Karl Jr, C. Bevis, D. E. Adams, H. C. Kapteyn, M. M. Murnane, and G. F. Mancini, „Subwavelength

- coherent imaging of periodic samples using a 13.5 nm table-top high-harmonic light source”, *Nat. Photonics*, vol. 11, no. 4, pp. 259–263, Apr. 2017.
- [26] G. K. Tadesse, R. Klas, S. Demmler, S. Hädrich, I. Wahyutama, M. Steinert, C. Spielmann, M. Zürch, T. Pertsch, A. Tünnermann, J. Limpert, and J. Rothhardt, „High speed and high resolution table-top nanoscale imaging”, *Opt. Lett.*, vol. 41, no. 22, pp. 5170–5173, Nov. 2016.
- [27] J. H. Hubbell, W. J. Veigele, E. A. Briggs, R. T. Brown, D. T. Cromer, and R. J. Howerton, „Atomic form factors, incoherent scattering functions, and photon scattering cross sections”, *J. Phys. Chem. Ref. Data*, vol. 4, no. 3, pp. 471–538, Jul. 1975.
- [28] B. L. Henke, E. M. Gullikson, and J. C. Davis, „X-Ray Interactions: Photoabsorption, Scattering, Transmission, and Reflection at  $E = 50\text{--}30,000$  eV,  $Z = 1\text{--}92$ ”, *At. Data Nucl. Data Tables*, vol. 54, no. 2, pp. 181–342, Jul. 1993.
- [29] B. Enders, M. Dierolf, P. Cloetens, M. Stockmar, F. Pfeiffer, and P. Thibault, „Ptychography with broad-bandwidth radiation”, *Appl. Phys. Lett.*, vol. 104, no. 17, p. 171 104, Apr. 2014.
- [30] B. Chen, R. A. Dilanian, S. Teichmann, B. Abbey, A. G. Peele, G. J. Williams, P. Hannaford, L. Van Dao, H. M. Quiney, and K. A. Nugent, „Multiple wavelength diffractive imaging”, *Phys. Rev. A*, vol. 79, no. 2, p. 023 809, Feb. 2009.
- [31] G. O. Williams, A. I. Gonzalez, S. Künzel, L. Li, M. Lozano, E. Oliva, B. Iwan, S. Daboussi, W. Boutu, H. Merdji, M. Fajardo, and P. Zeitoun, „Fourier transform holography with high harmonic spectra for attosecond imaging applications”, *Opt. Lett.*, vol. 40, no. 13, pp. 3205–3208, Jul. 2015.
- [32] B. Zhang, D. F. Gardner, M. H. Seaberg, E. R. Shanblatt, C. L. Porter, R. Karl, C. A. Mancuso, H. C. Kapteyn, M. M. Murnane, and D. E. Adams, „Ptychographic hyperspectral spectro-microscopy with an extreme ultraviolet high harmonic comb”, *Opt. Express*, vol. 24, no. 16, pp. 18 745–18 754, Aug. 2016.

- 
- [33] P. Hariharan and K. Creath, „Interferometry”, *The Optics Encyclopedia: Basic Foundations and Practical Applications*, 2007.
- [34] A. A. Michelson and E. W. Morley, „On the relative motion of the Earth and the luminiferous ether”, *Am. J. Sci.*, vol. Series 3 Vol. 34, no. 203, pp. 333–345, Nov. 1887.
- [35] D. Gabor, „A New Microscopic Principle”, *Nature*, vol. 161, pp. 777–778, May 1948.
- [36] LIGO Scientific Collaboration and Virgo Collaboration, B. P. Abbott, R. Abbott, *et al.*, „Observation of Gravitational Waves from a Binary Black Hole Merger”, *Phys. Rev. Lett.*, vol. 116, no. 6, p. 061 102, Feb. 2016.
- [37] R. J. Bell, *Introductory Fourier Transform Spectroscopy*, 1st Edition edition. New York: Academic Pr, Apr. 1972.
- [38] C. J. Manning, R. A. Palmer, and J. L. Chao, „Step-scan Fourier-transform infrared spectrometer”, *Rev. Sci. Instrum.*, vol. 62, no. 5, pp. 1219–1229, May 1991.
- [39] M. Lewenstein, P. Balcou, M. Y. Ivanov, A. L’Huillier, and P. B. Corkum, „Theory of high-harmonic generation by low-frequency laser fields”, *Phys. Rev. A*, vol. 49, no. 3, p. 2117, Mar. 1994.
- [40] J. Tate, T. Augustine, H. G. Muller, P. Salières, P. Agostini, and L. F. DiMauro, „Scaling of Wave-Packet Dynamics in an Intense Midinfrared Field”, *Phys. Rev. Lett.*, vol. 98, no. 1, p. 013 901, Jan. 2007.
- [41] E. L. Falcão-Filho, V. M. Gkortsas, A. Gordon, and F. X. Kärtner, „Analytic scaling analysis of high harmonic generation conversion efficiency”, *Opt. Express*, vol. 17, no. 13, pp. 11 217–11 229, Jun. 2009.
- [42] T. Popmintchev, M.-C. Chen, D. Popmintchev, P. Arpin, S. Brown, S. Ališauskas, G. Andriukaitis, T. Balčiunas, O. D. Mücke, A. Pugzlys, A. Baltuška, B. Shim, S. E. Schrauth, A. Gaeta, C. Hernández-García, L. Plaja, A. Becker, A. Jaron-Becker, M. M. Murnane, and H. C. Kapteyn, „Bright Coherent Ultrahigh Harmonics in the keV X-ray Regime from Mid-

- Infrared Femtosecond Lasers”, *Science*, vol. 336, no. 6086, pp. 1287–1291, Jun. 2012.
- [43] J.-C. Diels and W. Rudolph, *Ultrashort laser pulse phenomena*. Elsevier, 2006.
- [44] P. Balcou, P. Salières, A. L’Huillier, and M. Lewenstein, „Generalized phase-matching conditions for high harmonics: The role of field-gradient forces”, *Phys. Rev. A*, vol. 55, no. 4, pp. 3204–3210, Apr. 1997.
- [45] M.-C. Chen, M. R. Gerrity, S. Backus, T. Popmintchev, X. Zhou, P. Arpin, X. Zhang, H. C. Kapteyn, and M. M. Murnane, „Spatially coherent, phase matched, high-order harmonic EUV beams at 50 kHz”, *Opt. Express*, vol. 17, no. 20, pp. 17376–17383, Sep. 2009.
- [46] T. Popmintchev, M.-C. Chen, A. Bahabad, M. Gerrity, P. Sidorenko, O. Cohen, I. P. Christov, M. M. Murnane, and H. C. Kapteyn, „Phase matching of high harmonic generation in the soft and hard X-ray regions of the spectrum”, *PNAS*, vol. 106, no. 26, pp. 10516–10521, Jun. 2009.
- [47] P. Salières, A. L’Huillier, and M. Lewenstein, „Coherence Control of High-Order Harmonics”, *Phys. Rev. Lett.*, vol. 74, no. 19, pp. 3776–3779, May 1995.
- [48] E. Constant, D. Garzella, P. Breger, E. Mével, C. Dorrer, C. Le Blanc, F. Salin, and P. Agostini, „Optimizing High Harmonic Generation in Absorbing Gases: Model and Experiment”, *Phys. Rev. Lett.*, vol. 82, no. 8, pp. 1668–1671, Feb. 1999.
- [49] M. Schnürer, Z. Cheng, M. Hentschel, G. Tempea, P. Kálmán, T. Brabec, and F. Krausz, „Absorption-Limited Generation of Coherent Ultrashort Soft-X-Ray Pulses”, *Phys. Rev. Lett.*, vol. 83, no. 4, pp. 722–725, Jul. 1999.
- [50] C. M. Heyl, J. Güdde, A. L’Huillier, and U. Höfer, „High-order harmonic generation with  $\mu\text{J}$  laser pulses at high repetition rates”, *J. Phys. B: At., Mol. Opt. Phys.*, vol. 45, no. 7, p. 074020, Mar. 2012.

- 
- [51] A. Rundquist, C. G. Durfee, Z. Chang, C. Herne, S. Backus, M. M. Murnane, and H. C. Kapteyn, „Phase-Matched Generation of Coherent Soft X-rays”, *Science*, vol. 280, no. 5368, pp. 1412–1415, May 1998.
- [52] R. Trebino, *Frequency-resolved optical gating: the measurement of ultrashort laser pulses*. Springer Science & Business Media, 2012.
- [53] E. Treacy, „Optical pulse compression with diffraction gratings”, *IEEE J. Quantum Electron.*, vol. 5, no. 9, pp. 454–458, Sep. 1969.
- [54] O. E. Martinez, J. P. Gordon, and R. L. Fork, „Negative group-velocity dispersion using refraction”, *JOSA A*, vol. 1, no. 10, pp. 1003–1006, Oct. 1984.
- [55] R. Szipöcs, K. Ferencz, C. Spielmann, and F. Krausz, „Chirped multilayer coatings for broadband dispersion control in femtosecond lasers”, *Opt. Lett.*, vol. 19, no. 3, pp. 201–203, Feb. 1994.
- [56] M. Nisoli, S. D. Silvestri, O. Svelto, R. Szipöcs, K. Ferencz, C. Spielmann, S. Sartania, and F. Krausz, „Compression of high-energy laser pulses below 5 fs”, *Opt. Lett.*, vol. 22, no. 8, pp. 522–524, Apr. 1997.
- [57] J. Rothhardt, S. Hädrich, A. Klenke, S. Demmler, A. Hoffmann, T. Gotschall, T. Eidam, M. Krebs, J. Limpert, and A. Tünnermann, „53W average power few-cycle fiber laser system generating soft x rays up to the water window”, *Opt. Lett.*, vol. 39, no. 17, pp. 5224–5227, Sep. 2014.
- [58] R. H. Stolen and C. Lin, „Self-phase-modulation in silica optical fibers”, *Phys. Rev. A*, vol. 17, no. 4, pp. 1448–1453, Apr. 1978.
- [59] J. Kasparian, R. Sauerbrey, and S. Chin, „The critical laser intensity of self-guided light filaments in air”, *Appl. Phys. B*, vol. 71, no. 6, pp. 877–879, Dec. 2000.
- [60] A. Braun, G. Korn, X. Liu, D. Du, J. Squier, and G. Mourou, „Self-channeling of high-peak-power femtosecond laser pulses in air”, *Opt. Lett.*, vol. 20, no. 1, pp. 73–75, Jan. 1995.

- [61] B. La Fontaine, F. Vidal, Z. Jiang, C. Y. Chien, D. Comtois, A. Desparois, T. W. Johnston, J.-C. Kieffer, H. Pépin, and H. P. Mercure, „Filamentation of ultrashort pulse laser beams resulting from their propagation over long distances in air”, *Phys. Plasmas*, vol. 6, no. 5, pp. 1615–1621, Apr. 1999.
- [62] D. E. Spence, P. N. Kean, and W. Sibbett, „60-fsec pulse generation from a self-mode-locked Ti:sapphire laser”, *Opt. Lett.*, vol. 16, no. 1, pp. 42–44, Jan. 1991.
- [63] F. Salin, J. Squier, and M. Piché, „Mode locking of Ti:Al<sub>2</sub>O<sub>3</sub> lasers and self-focusing: a Gaussian approximation”, *Opt. Lett.*, vol. 16, no. 21, pp. 1674–1676, Nov. 1991.
- [64] U. Keller, „Recent developments in compact ultrafast lasers”, *Nature*, vol. 424, no. 6950, p. 831, Aug. 2003.
- [65] S. Witte and K. S. E. Eikema, „Ultrafast Optical Parametric Chirped-Pulse Amplification”, *IEEE J. Sel. Top. Quantum Electron.*, vol. 18, no. 1, p. 296, Jan. 2012.
- [66] T. Wilhelm, J. Piel, and E. Riedle, „Sub-20-fs pulses tunable across the visible from a blue-pumped single-pass noncollinear parametric converter”, *Opt. Lett.*, vol. 22, no. 19, pp. 1494–1496, Oct. 1997.
- [67] G. Cerullo and S. De Silvestri, „Ultrafast optical parametric amplifiers”, *Rev. Sci. Instrum.*, vol. 74, no. 1, pp. 1–18, Jan. 2003.
- [68] D. Strickland and G. Mourou, „Compression of amplified chirped optical pulses”, *Opt. Commun.*, vol. 55, no. 6, pp. 447–449, Oct. 1985.
- [69] C. Sauteret, D. Husson, G. Thiell, S. Seznec, S. Gary, A. Migus, and G. Mourou, „Generation of 20-TW pulses of picosecond duration using chirped-pulse amplification in a Nd:glass power chain”, *Opt. Lett.*, vol. 16, no. 4, pp. 238–240, Feb. 1991.
- [70] A. Dubietis, G. Jonušauskas, and A. Piskarskas, „Powerful femtosecond pulse generation by chirped and stretched pulse parametric amplification in BBO crystal”, *Opt. Commun.*, vol. 88, no. 4, pp. 437–440, Apr. 1992.

- 
- [71] I. N. Ross, P. Matousek, M. Towrie, A. J. Langley, and J. L. Collier, „The prospects for ultrashort pulse duration and ultrahigh intensity using optical parametric chirped pulse amplifiers”, *Opt. Commun.*, vol. 144, no. 1, pp. 125–133, Dec. 1997.
- [72] I. N. Ross, P. Matousek, G. H. C. New, and K. Osvay, „Analysis and optimization of optical parametric chirped pulse amplification”, *JOSA B*, vol. 19, no. 12, pp. 2945–2956, Dec. 2002.
- [73] S. Witte, *Terawatt-intensity few-cycle laser pulses: Optical parametric chirped pulse amplification and frequency comb spectroscopy*. Amsterdam: Vrije Universiteit Amsterdam, Jun. 2007.
- [74] S. Witte, R. T. Zinkstok, A. L. Wolf, W. Hogervorst, W. Ubachs, and K. S. E. Eikema, „A source of 2 terawatt, 2.7 cycle laser pulses based on noncollinear optical parametric chirped pulse amplification”, *Opt. Express*, vol. 14, no. 18, pp. 8168–8177, Sep. 2006.
- [75] D. W. E. Noom, S. Witte, J. Morgenweg, R. K. Altmann, and K. S. E. Eikema, „High-energy, high-repetition-rate picosecond pulses from a quasi-CW diode-pumped Nd:YAG system”, *Opt. Lett.*, vol. 38, no. 16, p. 3021, Aug. 2013.
- [76] D. W. E. Noom, *Lensless microscopy using visible and extreme ultraviolet radiation*. Amsterdam: Vrije Universiteit Amsterdam, Jun. 2016.
- [77] J. Morgenweg and K. S. E. Eikema, „A 1.8 mJ, picosecond Nd:YVO<sub>4</sub> bounce amplifier pump front-end system for high-accuracy XUV-frequency comb spectroscopy”, *Laser Phys. Lett.*, vol. 9, no. 11, p. 781, Aug. 2012.
- [78] J. E. Bernard, E. McCullough, and A. J. Alcock, „High gain, diode-pumped Nd:YVO<sub>4</sub> slab amplifier”, *Opt. Commun.*, vol. 109, no. 1, pp. 109–114, Jun. 1994.
- [79] W. C. Scott and M. de Wit, „Birefringence compensation and TEM<sub>00</sub> mode enhancement in a Nd:YAG laser”, *Appl. Phys. Lett.*, vol. 18, no. 1, pp. 3–4, Jan. 1971.

- [80] H. J. Eichler, A. Haase, R. Menzel, and A. Siemoneit, „Thermal lensing and depolarization in a highly pumped Nd:YAG laser amplifier”, *J. Phys. D: Appl. Phys.*, vol. 26, no. 11, pp. 1884–1891, Nov. 1993.
- [81] E. Hecht, „Optics”, *Addison Wesley*, vol. 997, 2002.
- [82] J. W. Goodman, *Introduction to Fourier Optics*. Roberts and Company Publishers, 2005.
- [83] J. Miao, T. Ishikawa, E. H. Anderson, and K. O. Hodgson, „Phase retrieval of diffraction patterns from noncrystalline samples using the oversampling method”, *Phys. Rev. B*, vol. 67, no. 17, p. 174 104, May 2003.
- [84] S. Marchesini, H. He, H. N. Chapman, S. P. Hau-Riege, A. Noy, M. R. Howells, U. Weierstall, and J. C. H. Spence, „X-ray image reconstruction from a diffraction pattern alone”, *Phys. Rev. B*, vol. 68, no. 14, p. 140 101, Oct. 2003.
- [85] J. R. Fienup, „Phase retrieval algorithms: a comparison”, *Appl. Opt.*, vol. 21, no. 15, pp. 2758–2769, Aug. 1982.
- [86] J. M. Rodenburg and H. M. L. Faulkner, „A phase retrieval algorithm for shifting illumination”, *Appl. Phys. Lett.*, vol. 85, no. 20, pp. 4795–4797, Nov. 2004.
- [87] P. Thibault, M. Dierolf, A. Menzel, O. Bunk, C. David, and F. Pfeiffer, „High-Resolution Scanning X-ray Diffraction Microscopy”, *Science*, vol. 321, no. 5887, pp. 379–382, Jul. 2008.
- [88] B. C. McCallum and J. M. Rodenburg, „Simultaneous reconstruction of object and aperture functions from multiple far-field intensity measurements”, *JOSA A*, vol. 10, no. 2, pp. 231–239, Feb. 1993.
- [89] P. Thibault, M. Dierolf, O. Bunk, A. Menzel, and F. Pfeiffer, „Probe retrieval in ptychographic coherent diffractive imaging”, *Ultramicroscopy*, vol. 109, no. 4, pp. 338–343, Mar. 2009.
- [90] A. M. Maiden, M. J. Humphry, M. C. Sarahan, B. Kraus, and J. M. Rodenburg, „An annealing algorithm to correct positioning errors in ptychography”, *Ultramicroscopy*, vol. 120, pp. 64–72, Sep. 2012.

- 
- [91] M. Odstrcil, P. Baksh, S. A. Boden, R. Card, J. E. Chad, J. G. Frey, and W. S. Brocklesby, „Ptychographic coherent diffractive imaging with orthogonal probe relaxation”, *Opt. Express*, vol. 24, no. 8, pp. 8360–8369, Apr. 2016.
- [92] I. McNulty, J. Kirz, C. Jacobsen, E. H. Anderson, M. R. Howells, and D. P. Kern, „High-Resolution Imaging by Fourier Transform X-ray Holography”, *Science*, vol. 256, no. 5059, pp. 1009–1012, May 1992.
- [93] S. Eisebitt, J. Lüning, W. F. Schlotter, M. Lörngen, O. Hellwig, W. Eberhardt, and J. Stöhr, „Lensless imaging of magnetic nanostructures by X-ray spectro-holography”, *Nature*, vol. 432, no. 7019, pp. 885–888, Dec. 2004.
- [94] R. L. Sandberg, D. A. Raymondson, C. La-o-vorakiat, A. Paul, K. S. Raines, J. Miao, M. M. Murnane, H. C. Kapteyn, and W. F. Schlotter, „Tabletop soft-x-ray Fourier transform holography with 50 nm resolution”, *Opt. Lett.*, vol. 34, no. 11, pp. 1618–1620, Jun. 2009.
- [95] R. L. Sandberg, A. Paul, D. A. Raymondson, S. Hädrich, D. M. Gaudiosi, J. Holtsnider, R. I. Tobey, O. Cohen, M. M. Murnane, H. C. Kapteyn, C. Song, J. Miao, Y. Liu, and F. Salmassi, „Lensless Diffractive Imaging Using Tabletop Coherent High-Harmonic Soft-X-Ray Beams”, *Phys. Rev. Lett.*, vol. 99, no. 9, p. 098 103, Aug. 2007.
- [96] S. Marchesini, S. Boutet, A. E. Sakdinawat, M. J. Bogan, S. Bajt, A. Barty, H. N. Chapman, M. Frank, S. P. Hau-Riege, A. Szöke, C. Cui, D. A. Shapiro, M. R. Howells, J. C. H. Spence, J. W. Shaevitz, J. Y. Lee, J. Hajdu, and M. M. Seibert, „Massively parallel X-ray holography”, *Nat. Photonics*, vol. 2, no. 9, pp. 560–563, Sep. 2008.
- [97] O. Kfir, S. Zayko, C. Nolte, M. Sivilis, M. Möller, B. Hebler, S. S. P. K. Arekapudi, D. Steil, S. Schäfer, M. Albrecht, O. Cohen, S. Mathias, and C. Ropers, „Nanoscale magnetic imaging using circularly polarized high-harmonic radiation”, *Sci. Adv.*, vol. 3, no. 12, eaao4641, Dec. 2017.

- [98] P. D. Baksh, M. Odstrčil, H.-S. Kim, S. A. Boden, J. G. Frey, and W. S. Brocklesby, „Wide-field broadband extreme ultraviolet transmission ptychography using a high-harmonic source”, *Opt. Lett.*, vol. 41, no. 7, pp. 1317–1320, Apr. 2016.
- [99] F. Krausz and M. Ivanov, „Attosecond physics”, *Rev. Mod. Phys.*, vol. 81, no. 1, p. 163, Feb. 2009.
- [100] T. Popmintchev, M.-C. Chen, P. Arpin, M. M. Murnane, and H. C. Kapteyn, „The attosecond nonlinear optics of bright coherent X-ray generation”, *Nat. Photonics*, vol. 4, no. 12, p. 822, Dec. 2010.
- [101] P. Salières, L. Le Déroff, T. Auguste, P. Monot, P. d’Oliveira, D. Campo, J.-F. Hergott, H. Merdji, and B. Carré, „Frequency-Domain Interferometry in the XUV with High-Order Harmonics”, *Phys. Rev. Lett.*, vol. 83, no. 26, p. 5483, Dec. 1999.
- [102] N. A. Papadogiannis, B. Witzel, C. Kalpouzos, and D. Charalambidis, „Observation of Attosecond Light Localization in Higher Order Harmonic Generation”, *Phys. Rev. Lett.*, vol. 83, no. 21, p. 4289, Nov. 1999.
- [103] D. Descamps, C. Lyngå, J. Norin, A. L’Huillier, C.-G. Wahlström, J.-F. Hergott, H. Merdji, P. Salières, M. Bellini, and T. W. Hänsch, „Extreme ultraviolet interferometry measurements with high-order harmonics”, *Opt. Lett.*, vol. 25, no. 2, p. 135, Jan. 2000.
- [104] M. Kovačev, S. V. Fomichev, E. Priori, Y. Mairesse, H. Merdji, P. Monchicourt, P. Breger, J. Norin, A. Persson, A. L’Huillier, C.-G. Wahlström, B. Carré, and P. Salières, „Extreme Ultraviolet Fourier-Transform Spectroscopy with High Order Harmonics”, *Phys. Rev. Lett.*, vol. 95, no. 22, p. 223 903, Nov. 2005.
- [105] Y. Nabekawa, T. Shimizu, Y. Furukawa, E. J. Takahashi, and K. Midorikawa, „Interferometry of Attosecond Pulse Trains in the Extreme Ultraviolet Wavelength Region”, *Phys. Rev. Lett.*, vol. 102, no. 21, p. 213 904, May 2009.

- 
- [106] D. Z. Kandula, C. Gohle, T. J. Pinkert, W. Ubachs, and K. S. E. Eikema, „Extreme Ultraviolet Frequency Comb Metrology”, *Phys. Rev. Lett.*, vol. 105, no. 6, p. 063 001, Aug. 2010.
- [107] Y. Meng, C. Zhang, C. Marceau, A. Y. Naumov, P. B. Corkum, and D. M. Villeneuve, „Interferometric time delay correction for Fourier transform spectroscopy in the extreme ultraviolet”, *J. Mod. Opt.*, vol. 63, no. 17, p. 1661, Apr. 2016.
- [108] J. B. Bertrand, H. J. Wörner, P. Salières, D. M. Villeneuve, and P. B. Corkum, „Linked attosecond phase interferometry for molecular frame measurements”, *Nat. Phys.*, vol. 9, no. 3, p. 174, Feb. 2013.
- [109] D. R. Austin, T. Witting, C. A. Arrell, F. Frank, A. S. Wyatt, J. P. Marangos, J. W. G. Tisch, and I. A. Walmsley, „Lateral shearing interferometry of high-harmonic wavefronts”, *Opt. Lett.*, vol. 36, no. 10, pp. 1746–1748, May 2011.
- [110] A. S. Wyatt, T. Witting, A. Schiavi, D. Fabris, P. Matia-Hernando, I. A. Walmsley, J. P. Marangos, and J. W. G. Tisch, „Attosecond sampling of arbitrary optical waveforms”, *Optica*, vol. 3, no. 3, p. 303, Mar. 2016.
- [111] S. Witte, V. T. Tenner, D. W. Noom, and K. S. Eikema, „Lensless diffractive imaging with ultra-broadband table-top sources: from infrared to extreme-ultraviolet wavelengths”, *Light Sci. Appl.*, vol. 3, no. 3, e163, Mar. 2014.
- [112] A. Klisnick, O. Guilbaud, D. Ros, K. Cassou, S. Kazamias, G. Jamelot, J. .-.-C. Lagron, D. Joyeux, D. Phalippou, Y. Lechantre, M. Edwards, P. Mistry, and G. J. Tallents, „Experimental study of the temporal coherence and spectral profile of the 13.9nm transient X-ray laser”, *J. Quant. Spectrosc. Radiat. Transfer*, Radiative Properties of Hot Dense Matter, vol. 99, no. 1–3, p. 370, May 2006.
- [113] N. de Oliveira, M. Roudjane, D. Joyeux, D. Phalippou, J.-C. Rodier, and L. Nahon, „High-resolution broad-bandwidth Fourier-transform absorption spectroscopy in the VUV range down to 40 nm”, *Nature Photon.*, vol. 5, no. 3, p. 149, Mar. 2011.

- [114] J. A. Terschlüsen, M. Agåker, M. Svanqvist, S. Plogmaker, J. Nordgren, J. -.-E. Rubensson, H. Siegbahn, and J. Söderström, „Measuring the temporal coherence of a high harmonic generation setup employing a Fourier transform spectrometer for the VUV/XUV”, *Nucl. Instrum. Methods Phys. Res., Sect. A*, vol. 768, p. 84, Dec. 2014.
- [115] M.-C. Chen, C. Mancuso, C. Hernández-García, F. Dollar, B. Galloway, D. Popmintchev, P.-C. Huang, B. Walker, L. Plaja, A. A. Jaroń-Becker, A. Becker, M. M. Murnane, H. C. Kapteyn, and T. Popmintchev, „Generation of bright isolated attosecond soft X-ray pulses driven by multicycle midinfrared lasers”, *PNAS*, vol. 111, no. 23, E2361, May 2014.
- [116] D. Brida, C. Manzoni, and G. Cerullo, „Phase-locked pulses for two-dimensional spectroscopy by a birefringent delay line”, *Opt. Lett.*, vol. 37, no. 15, p. 3027, Aug. 2012.
- [117] A. Oriana, J. Réhault, F. Preda, D. Polli, and G. Cerullo, „Scanning Fourier transform spectrometer in the visible range based on birefringent wedges”, *JOSA A*, vol. 33, no. 7, pp. 1415–1420, Aug. 2016.
- [118] M. J. Padgett and A. R. Harvey, „A static Fourier-transform spectrometer based on Wollaston prisms”, *Rev. Sci. Instrum.*, vol. 66, no. 4, pp. 2807–2811, Aug. 1995.
- [119] The Center for X-Ray Optics (CXRO). (). X-Ray Database, [Online]. Available: [http://henke.lbl.gov/optical\\_constants/](http://henke.lbl.gov/optical_constants/) (visited on 11/19/2018).
- [120] D. Shapiro, P. Thibault, T. Beetz, V. Elser, M. Howells, C. Jacobsen, J. Kirz, E. Lima, H. Miao, A. M. Neiman, and D. Sayre, „Biological imaging by soft x-ray diffraction microscopy”, *PNAS*, vol. 102, no. 43, pp. 15 343–15 346, Oct. 2005.
- [121] M. Holler, M. Guizar-Sicairos, E. H. R. Tsai, R. Dinapoli, E. Müller, O. Bunk, J. Raabe, and G. Aeppli, „High-resolution non-destructive three-dimensional imaging of integrated circuits”, *Nature*, vol. 543, no. 7645, pp. 402–406, Mar. 2017.

- 
- [122] M. Zürch, J. Rothhardt, S. Hädrich, S. Demmler, M. Krebs, J. Limpert, A. Tünnermann, A. Guggenmos, U. Kleineberg, and C. Spielmann, „Real-time and Sub-wavelength Ultrafast Coherent Diffraction Imaging in the Extreme Ultraviolet”, *Sci. Rep.*, vol. 4, p. 7356, Dec. 2014.
- [123] W. J. Huang, J. M. Zuo, B. Jiang, K. W. Kwon, and M. Shim, „Sub-ångström-resolution diffractive imaging of single nanocrystals”, *Nat. Phys.*, vol. 5, no. 2, pp. 129–133, Feb. 2009.
- [124] A. V. Martin, F. Wang, N. D. Loh, T. Ekeberg, F. R. N. C. Maia, M. Hantke, G. v. d. Schot, C. Y. Hampton, R. G. Sierra, A. Aquila, S. Bajt, M. Barthelmess, C. Bostedt, J. D. Bozek, N. Coppola, S. W. Epp, B. Erk, H. Fleckenstein, L. Foucar, M. Frank, H. Graafsma, L. Gumprecht, A. Hartmann, R. Hartmann, G. Hauser, H. Hirsemann, P. Holl, S. Kassemeyer, N. Kimmel, M. Liang, L. Lomb, S. Marchesini, K. Nass, E. Pedersoli, C. Reich, D. Rolles, B. Rudek, A. Rudenko, J. Schulz, R. L. Shoeman, H. Soltau, D. Starodub, J. Steinbrener, F. Stellato, L. Strüder, J. Ullrich, G. Weidenspointner, T. A. White, C. B. Wunderer, A. Barty, I. Schlichting, M. J. Bogan, and H. N. Chapman, „Noise-robust coherent diffractive imaging with a single diffraction pattern”, *Opt. Express*, vol. 20, no. 15, pp. 16 650–16 661, Jul. 2012.
- [125] V. T. Tenner, K. S. E. Eikema, and S. Witte, „Fourier transform holography with extended references using a coherent ultra-broadband light source”, *Opt. Express*, vol. 22, no. 21, pp. 25 397–25 409, Oct. 2014.
- [126] D. Gauthier, M. Guizar-Sicairos, X. Ge, W. Boutu, B. Carré, J. R. Fienup, and H. Merdji, „Single-shot Femtosecond X-Ray Holography Using Extended References”, *Phys. Rev. Lett.*, vol. 105, no. 9, p. 093 901, Aug. 2010.
- [127] M. E. Riley and M. A. Gusinow, „Laser beam divergence utilizing a lateral shearing interferometer”, *Appl. Opt.*, vol. 16, no. 10, pp. 2753–2756, Oct. 1977.

- [128] C. Falldorf, C. v. Kopylow, and R. B. Bergmann, „Wave field sensing by means of computational shear interferometry”, *JOSA A*, vol. 30, no. 10, pp. 1905–1912, Oct. 2013.
- [129] G. S. M. Jansen, D. Rudolf, L. Freisem, K. S. E. Eikema, and S. Witte, „Spatially resolved Fourier transform spectroscopy in the extreme ultraviolet”, *Optica*, vol. 3, no. 10, pp. 1122–1125, Oct. 2016.
- [130] L. Loetgering, H. Froese, T. Wilhein, and M. Rose, „Phase retrieval via propagation-based interferometry”, *Phys. Rev. A*, vol. 95, no. 3, p. 033 819, Mar. 2017.
- [131] S. Marchesini, „Invited Article: A unified evaluation of iterative projection algorithms for phase retrieval”, *Rev. Sci. Instrum.*, vol. 78, no. 1, p. 011 301, Jan. 2007.
- [132] F. Capotondi, E. Pedersoli, M. Kiskinova, A. V. Martin, M. Barthelmess, and H. N. Chapman, „A scheme for lensless X-ray microscopy combining coherent diffraction imaging and differential corner holography”, *Opt. Express*, vol. 20, no. 22, pp. 25 152–25 160, Oct. 2012.
- [133] R. Souffi and E. M. Gullikson, „Optical constants of materials for multilayer mirror applications in the EUV/soft x-ray region”, in *Grazing Incidence and Multilayer X-Ray Optical Systems*, vol. 3113, International Society for Optics and Photonics, Jul. 1997, pp. 222–230.
- [134] E. Louis, A. E. Yakshin, T. Tsarfati, and F. Bijkerk, „Nanometer interface and materials control for multilayer EUV-optical applications”, *Prog. Surf. Sci.*, vol. 86, no. 11, pp. 255–294, Dec. 2011.
- [135] Y.-S. Ku, C.-L. Yeh, Y.-C. Chen, C.-W. Lo, W.-T. Wang, and M.-C. Chen, „EUV scatterometer with a high-harmonic-generation EUV source”, *Opt. Express*, vol. 24, no. 24, pp. 28 014–28 025, Nov. 2016.

- 
- [136] C. T. Chantler, „Theoretical Form Factor, Attenuation, and Scattering Tabulation for  $Z=1-92$  from  $E=1-10$  eV to  $E=0.4-1.0$  MeV”, *J. Phys. Chem. Ref. Data*, vol. 24, no. 1, pp. 71–643, Jan. 1995.
- [137] C. Tarrío, R. N. Watts, T. B. Lucatorto, J. M. Slaughter, and C. M. Falco, „Optical constants of in situ-deposited films of important extreme-ultraviolet multilayer mirror materials”, *Appl. Opt.*, vol. 37, no. 19, pp. 4100–4104, Jul. 1998.
- [138] H. Y. Kang, J. D. Lim, P. Peranantham, and C. K. HwangBo, „Determination of Optical Constants of Thin Films in Extreme Ultraviolet Wavelength Region by an Indirect Optical Method”, *J. Opt. Soc. Korea*, vol. 17, no. 1, pp. 38–43, Feb. 2013.
- [139] R. Soufli and E. M. Gullikson, „Reflectance measurements on clean surfaces for the determination of optical constants of silicon in the extreme ultraviolet–soft-x-ray region”, *Appl. Opt.*, vol. 36, no. 22, pp. 5499–5507, Aug. 1997.
- [140] D. L. Windt, W. C. Cash, M. Scott, P. Arendt, B. Newnam, R. F. Fisher, A. B. Swartzlander, P. Z. Takacs, and J. M. Pinneo, „Optical constants for thin films of C, diamond, Al, Si, and CVD SiC from 24 Å to 1216 Å”, *Appl. Opt.*, vol. 27, no. 2, pp. 279–295, Jan. 1988.
- [141] B. Mills, C. F. Chau, E. T. F. Rogers, J. Grant-Jacob, S. L. Stebbings, M. Praeger, A. M. de Paula, C. A. Froud, R. T. Chapman, T. J. Butcher, J. J. Baumberg, W. S. Brocklesby, and J. G. Frey, „Direct measurement of the complex refractive index in the extreme ultraviolet spectral region using diffraction from a nanosphere array”, *Appl. Phys. Lett.*, vol. 93, no. 23, p. 231 103, Dec. 2008.
- [142] B. Kjornrattanawanich, D. L. Windt, J. A. Bellotti, and J. F. Seely, „Measurement of dysprosium optical constants in the 2-830 eV spectral range using a transmittance method, and compilation of the revised optical constants of lanthanum, terbium, neodymium, and gadolinium”, *Appl. Opt.*, vol. 48, no. 16, pp. 3084–3093, Jun. 2009.

- [143] B. Sae-Lao and R. Soufli, „Measurements of the refractive index of yttrium in the 50–1300 eV energy region”, *Appl. Opt.*, vol. 41, no. 34, pp. 7309–7316, Dec. 2002.
- [144] Y. A. Uspenskii, J. F. Seely, N. L. Popov, A. V. Vinogradov, Y. P. Pershin, and V. V. Kondratenko, „Efficient method for the determination of extreme-ultraviolet optical constants in reactive materials: application to scandium and titanium”, *JOSA A*, vol. 21, no. 2, pp. 298–305, Feb. 2004.
- [145] C. Chang, E. Anderson, P. Naulleau, E. Gullikson, K. Goldberg, and D. Attwood, „Direct measurement of index of refraction in the extreme-ultraviolet wavelength region with a novel interferometer”, *Opt. Lett.*, vol. 27, no. 12, pp. 1028–1030, Jun. 2002.
- [146] L. Poletto, F. Frassetto, F. Calegari, S. Anumula, A. Trabattoni, and M. Nisoli, „Micro-focusing of attosecond pulses by grazing-incidence toroidal mirrors”, *Opt. Express*, vol. 21, no. 11, pp. 13 040–13 051, Jun. 2013.
- [147] M. Hofstetter, M. Schultze, M. Fieß, B. Dennhardt, A. Guggenmos, J. Gagnon, V. S. Yakovlev, E. Goulielmakis, R. Kienberger, E. M. Gullikson, F. Krausz, and U. Kleineberg, „Attosecond dispersion control by extreme ultraviolet multilayer mirrors”, *Opt. Express*, vol. 19, no. 3, pp. 1767–1776, Jan. 2011.
- [148] F. Ferrari, F. Calegari, M. Lucchini, C. Vozzi, S. Stagira, G. Sansone, and M. Nisoli, „High-energy isolated attosecond pulses generated by above-saturation few-cycle fields”, *Nat. Photonics*, vol. 4, no. 12, pp. 875–879, Dec. 2010.
- [149] H. Mashiko, S. Gilbertson, C. Li, S. D. Khan, M. M. Shakya, E. Moon, and Z. Chang, „Double Optical Gating of High-Order Harmonic Generation with Carrier-Envelope Phase Stabilized Lasers”, *Phys. Rev. Lett.*, vol. 100, no. 10, p. 103 906, Mar. 2008.
- [150] D. J. Batey, D. Claus, and J. M. Rodenburg, „Information multiplexing in ptychography”, *Ultramicroscopy*, vol. 138, pp. 13–21, Mar. 2014.

- 
- [151] E. J. Candes and M. B. Wakin, „An Introduction To Compressive Sampling”, *IEEE Signal Process. Mag.*, vol. 25, no. 2, pp. 21–30, Mar. 2008.
- [152] J. Hartmann, „Bemerkungen über den Bau und die Justirung von Spektrographen”, *Zeitschrift für Instrumentenkunde*, vol. 20, pp. 47–58, 1900.
- [153] B. C. Platt and R. Shack, „History and Principles of Shack-Hartmann Wavefront Sensing”, *J. Refract. Surg.*, vol. 17, S573, 2001.
- [154] P. Mercère, P. Zeitoun, M. Idir, S. Le Pape, D. Douillet, X. Levecq, G. Dovillaire, S. Bucourt, K. a. Goldberg, P. P. Naulleau, and S. Rekawa, „Hartmann wave-front measurement at 13.4 nm with  $\lambda_{EUV}/120$  accuracy”, *Opt. Lett.*, vol. 28, no. 17, pp. 1534–1536, Sep. 2003.
- [155] C. Valentin, J. Gautier, J.-P. Goddet, C. Hauri, T. Marchenko, E. Papalazarou, G. Rey, S. Sebban, O. Scrick, P. Zeitoun, G. Dovillaire, X. Levecq, S. Bucourt, and M. Fajardo, „High-order harmonic wave fronts generated with controlled astigmatic infrared laser”, *JOSA B*, vol. 25, no. 7, B161–B166, Jul. 2008.
- [156] P. Rudawski, C. M. Heyl, F. Brizuela, J. Schwenke, a. Persson, E. Mansten, R. Rakowski, L. Rading, F. Campi, B. Kim, P. Johnsson, and a. L’Huillier, „A high-flux high-order harmonic source.”, *Rev. Sci. Instrum.*, vol. 84, no. 7, p. 073 103, Jul. 2013.
- [157] S. L. Cousin, F. Silva, S. Teichmann, M. Hemmer, B. Buades, and J. Biegert, „High-flux table-top soft x-ray source driven by sub-2-cycle, CEP stable, 1.85- $\mu\text{m}$  1-kHz pulses for carbon K-edge spectroscopy”, *Opt. Lett.*, vol. 39, no. 18, p. 5383, Sep. 2014.
- [158] P. M. Kraus, B. Mignolet, D. Baykusheva, A. Rupenyan, L. Horný, E. F. Penka, G. Grassi, O. I. Tolstikhin, J. Schneider, F. Jensen, L. B. Madsen, A. D. Bandrauk, F. Remacle, and H. J. Wörner, „Measurement and laser control of attosecond charge migration in ionized iodoacetylene”, *Science*, vol. 350, no. 6262, pp. 790–795, Nov. 2015.

- [159] F. Silva, S. M. Teichmann, S. L. Cousin, M. Hemmer, and J. Biegert, „Spatiotemporal isolation of attosecond soft X-ray pulses in the water window”, *Nat. Commun.*, vol. 6, p. 6611, Mar. 2015.
- [160] X. He, M. Miranda, J. Schwenke, O. Guilbaud, T. Ruchon, C. Heyl, E. Georgadiou, R. Rakowski, A. Persson, M. B. Gaarde, and A. L’Huillier, „Spatial and spectral properties of the high-order harmonic emission in argon for seeding applications”, *Phys. Rev. A*, vol. 79, no. 6, p. 063 829, Jun. 2009.
- [161] E. Frumker, G. G. Paulus, H. Niikura, A. Naumov, D. M. Villeneuve, and P. B. Corkum, „Order-dependent structure of high harmonic wavefronts”, *Opt. Express*, vol. 20, no. 13, pp. 13 870–13 877, Jun. 2012.
- [162] F. Schapper, M. Holler, T. Auguste, A. Zaïr, M. Weger, P. Salières, L. Gallmann, and U. Keller, „Spatial fingerprint of quantum path interferences in high order harmonic generation”, *Opt. Express*, vol. 18, no. 3, pp. 2987–2994, Feb. 2010.
- [163] H. Vincenti and F. Quéré, „Attosecond Lighthouses: How To Use Spatiotemporally Coupled Light Fields To Generate Isolated Attosecond Pulses”, *Phys. Rev. Lett.*, vol. 108, no. 11, p. 113 904, Mar. 2012.
- [164] K. T. Kim, C. Zhang, T. Ruchon, J.-F. Hergott, T. Auguste, D. M. Villeneuve, P. B. Corkum, and F. Quéré, „Photonic streaking of attosecond pulse trains”, *Nat. Photonics*, vol. 7, no. 8, pp. 651–656, Aug. 2013.
- [165] E. Frumker, G. G. Paulus, H. Niikura, D. M. Villeneuve, and P. B. Corkum, „Frequency-resolved high-harmonic wavefront characterization”, *Opt. Lett.*, vol. 34, no. 19, pp. 3026–3028, Oct. 2009.
- [166] D. T. Lloyd, K. O’Keeffe, and S. M. Hooker, „Complete spatial characterization of an optical wavefront using a variable-separation pinhole pair”, *Opt. Lett.*, vol. 38, no. 7, pp. 1173–1175, Apr. 2013.

- 
- [167] M. M. Mang, C. Bourassin-Bouchet, and I. A. Walmsley, „Simultaneous spatial characterization of two independent sources of high harmonic radiation”, *Opt. Lett.*, vol. 39, no. 21, pp. 6142–6145, Nov. 2014.
- [168] X. Ge, W. Boutu, D. Gauthier, F. Wang, A. Borta, B. Barbrel, M. Ducouso, A. I. Gonzalez, B. Carré, D. Guillaumet, M. Perdrix, O. Gobert, J. Gautier, G. Lambert, F. R. N. C. Maia, J. Hajdu, P. Zeitoun, and H. Merdji, „Impact of wave front and coherence optimization in coherent diffractive imaging”, *Opt. Express*, vol. 21, no. 9, pp. 11 441–11 447, May 2013.
- [169] J. Wyant and K. Creath, „Basic wavefront aberration theory for optical metrology”, in *Applied Optics and Optical Engineering*, vol. XI, New York: Academic Press, 1992, pp. 1–53.
- [170] S. Künzel, G. O. Williams, W. Boutu, E. Galtier, B. Barbrel, H. J. Lee, B. Nagler, U. Zastra, G. Dovillaire, R. W. Lee, H. Merdji, P. Zeitoun, and M. Fajardo, „Shot-to-shot intensity and wavefront stability of high-harmonic generation”, *Appl. Opt.*, vol. 54, no. 15, pp. 4745–4749, May 2015.
- [171] H. Wikmark, C. Guo, J. Vogelsang, P. W. Smorenburg, H. Coudert-Alteirac, J. Lahl, J. Peschel, P. Rudawski, H. Dacasa, S. Carlström, S. Maclot, M. B. Gaarde, P. Johnsson, C. L. Arnold, and A. L’Huillier, „Spatiotemporal coupling of attosecond pulses”, *PNAS*, p. 201 817 626, Mar. 2019.
- [172] R. B. Hoover and A. B. C. Walker, „Multilayer and Grazing Incidence X-Ray/EUV Optics II”, in *SPIE Proceedings Series*, vol. 2011, San Diego, California: SPIE, Jul. 1993, p. 11.
- [173] A. Perri, B. E. N. d. Faria, D. C. T. Ferreira, D. Comelli, G. Valentini, F. Preda, D. Polli, A. M. d. Paula, G. Cerullo, and C. Manzoni, „Hyperspectral imaging with a TWINS birefringent interferometer”, *Opt. Express*, vol. 27, no. 11, pp. 15 956–15 967, May 2019.



# List of Publications

**This thesis is based on the following publications:**

**Chapter 4:** G. S. M. Jansen, D. Rudolf, L. Freisem, K. S. E. Eikema, and S. Witte, *Spatially Resolved Fourier Transform Spectroscopy in the Extreme Ultraviolet*, *Optica* **3**, 1122-1125(2016).

**Chapter 5:** G. S. M. Jansen, A. de Beurs, X. Liu, K. S. E. Eikema, and S. Witte, *Diffraction shear interferometry for extreme ultraviolet high-resolution lensless imaging*, *Opt. Express* **26**, 12479-12489 (2018).

**Chapter 6:** G. S. M. Jansen, X. Liu, K. S. E. Eikema, and S. Witte, *Broadband extreme ultraviolet dispersion measurements using a high-harmonic source*, *Opt. Lett.* **44**, 3625-3628 (2019).

**Chapter 8:** L. Freisem, G. S. M. Jansen, D. Rudolf, K. S. E. Eikema, and S. Witte, *Spectrally resolved single-shot wavefront sensing of broadband high-harmonic sources*, *Opt. Express* **26**, 6860-6871 (2018).

**The author also contributed to the following publications:**

- (i) S. M. Witte, G. S. M. Jansen, L. C. Freisem, K. S. E. Eikema, S. G. J. Mathijssen, *Methods and Apparatus for Predicting Performance of a Measurement Method*, *Measurement Method and Apparatus*, US Patent App. 15/979,990, (2018).

- (ii) J. L. Ellis, K. M. Dorney, D. D. Hickstein, N. J. Brooks, C. Gentry, C. Hernández-García, D. Zusin, J. M. Shaw, Q. L. Nguyen, C. A. Mancuso, G. S. M. Jansen, S. Witte, H. C. Kapteyn, and M. M. Murnane, *High harmonics with spatially varying ellipticity*, *Optica* **5**(4), 479-485 (2018).
  
- (iii) T. J. Pinkert, O. Böll, L. Willmann, G. S. M. Jansen, E. A. Dijck, B. G. H. M. Groeneveld, R. Smets, F. C. Bosveld, W. Ubachs, K. Jungmann, K. S. E. Eikema, J. C. J. Koelemeij, *Effect of soil temperature on optical frequency transfer through unidirectional dense-wavelength-division-multiplexing fiber-optic links*, *Appl. Opt.* **54**(4), 728-738 (2015).

# Summary

High harmonic generation (HHG) provides a table-top source of coherent extreme ultraviolet (EUV) radiation. A particularly promising application of HHG is in coherent diffractive imaging (CDI), where the short wavelengths enable much higher spatial resolution than what can be achieved with visible light. One of the key features of HHG is that it produces a broad spectrum consisting of narrow harmonics spanning the EUV spectral range. As CDI on the other hand requires monochromatic illumination, HHG-based CDI experiments effectively have to dump most of the EUV flux generated.

In chapter 4, we demonstrate spatially resolved Fourier transform spectroscopy with high harmonics. This is possible because of the unique coherence of the HHG process: generating high harmonics with identical driving pulses yields identical EUV pulses. Using a common-path interferometer based on birefringent wedges, we generate a pulse pair with which we generate two high harmonic beams.

The laser from which these pulses are derived is described in chapter 2. The non-collinear optical parametric chirped pulse amplifier, which is seeded by a Ti:sapphire modelocked laser, has been subject to a significant development during this project. As a result of this, the output has changed from 45 fs, 4 mJ pulses to 25 fs pulses with more than 10 mJ per pulse. This leads to a pulse energy of more than 2.5 mJ after the birefringent wedge interferometer with similar pulse duration. Operating at 300 Hz, this system is capable of creating a large photon flux at extreme ultraviolet wavelengths, which is crucial for coherent diffractive imaging.

To ensure that both driving pulses generate HHG independent of each other, the pulses are separated by at least 300 micron in the focus. After the focus, the high harmonics diverge and form two overlapping Gaussian beams in the far field. Due to the sub-attosecond timing stability of the interferometer, we are able to observe EUV interference

at wavelengths as short as 17 nm.

We perform Fourier transform spectroscopy (FTS) by measuring the EUV interference on a CCD camera as a function of delay. This yields a spectrum for every pixel on the camera. We use FTS to measure the high harmonic spectra as generated in argon, krypton and neon, and in order to demonstrate that spatial resolution can be obtained from this measurement, we measure the spatially-dependent spectral absorption of a thin titanium film.

In chapter 5, we demonstrate diffractive shear interferometry (DSI), a type of spectrally resolved lensless imaging. This extends the spatial resolution obtained in spatially resolved FTS to beyond the camera pixel size. The main difference with traditional CDI is caused by the slight angle between the two beams, arising from the two separate foci. This shears the diffraction pattern of one beam with respect to the other. Fourier transform spectroscopy measured the complex-valued overlap between the diffraction patterns.

In chapter 5, an image reconstruction algorithm for such interference patterns is developed and demonstrated. We show that the algorithm enables diffraction-limited image reconstructions similar to those achieved in traditional CDI. In particular, it is possible to reconstruct images of highly complex samples. From simulations comparing DSI and CDI, it is clear that the interferometric measurement and reconstruction leads to a faster image reconstruction. Finally, we demonstrate that DSI is compatible with Fourier transform holography.

Chapter 6 focuses on the measurement of spectral phases. Fourier transform spectroscopy is sensitive to the phase difference between the beams. This is used to measure the optical path length introduced by a thin film sample in one of the beams. This provides a direct measurement of the group velocity dispersion of a sample, and it can be extended to a full refractive index measurement. If the refractive index is known, this can be used to measure the thickness of the sample.

In chapter 7, a few possible future developments are discussed. In particular, further demonstration of spectrally resolved lensless imaging will allow the determination of elemental composition and thickness for structured thin films. A promising extension of DSI is the combination with scanning illumination techniques based on ptychography.

In chapters 8 and 9, an alternative solution to spectrally resolved

---

metrology is investigated. A carefully designed Hartmann wavefront sensor with gratings inscribed in the apertures is used to disperse the high harmonics. From the near-field diffraction pattern of this spectral Hartmann mask (SHM), Hartmann wavefront measurements can be extracted for the individual high harmonics. After analysis, this yields full wavefront information in addition to the wavelengths and linewidths of the high harmonics.

In chapter 8, the SHM is demonstrated using our high harmonic generation beam line. After the publication of these results, we initiated a collaboration with Prof. Anne l’Huillier and her coworkers at Lund University, Sweden. Chapter 9 provides a short report on the first measurements that were taken as part of this collaboration, which aims to demonstrate that HHG in a focused beam leads to a natural chromatic aberration of the high harmonics.

Although one of the measurements hints at chromatic aberration in high harmonics produced in xenon, the achieved precision in this first measurement series was not enough to clearly demonstrate high harmonic chromatic aberration. Chapter 9 therefore follows up with a discussion on the signal strength and precision obtained in an SHM measurement. This discussion yields the following recommendations: The signal-to-noise ratio of raw SHM measurements must be optimized as much as possible to achieve good wavefront sensitivity. This can be achieved with long exposures and excellent infrared rejection. The strength of the measured chromatic aberration will be stronger closer to the source. It is therefore important to place the SHM as close as possible to the HHG source. Furthermore, it is expected that stronger chromatic aberration will be observed in a more tightly focused HHG geometry.



# Samenvatting

## Achtergrond en motivatie

De titel van dit proefschrift kan vertaald worden als *lens-vrije, spectraal opgeloste microscopie en metrologie met extreem ultraviolet licht*. Het gaat hier om de ontwikkeling van een microscopietechniek met specifieke eigenschappen die andere microscopietechnieken niet hebben.

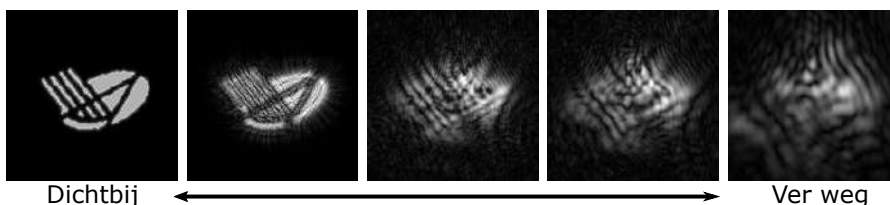
De microscoop is al eeuwenlang een van de belangrijkste onderzoeksmiddelen in de wetenschap. Een bekend voorbeeld is het werk van Antonie van Leeuwenhoek, die met behulp van zijn eigen handgemaakte microscopen allerlei biologische cellen bestudeerde. Sindsdien heeft de microscoop een gigantische ontwikkeling doorgemaakt. Tegenwoordig bestaan er talloze microscoop-soorten die allemaal geoptimaliseerd zijn voor verschillende situaties. Een belangrijke drijfveer voor de ontwikkeling van nieuwe, betere microscopietechnieken is de zoektocht naar hogere resolutie om zo kleinere details te kunnen waarnemen. In optische microscopen hangt de resolutie af van de kwaliteit van het lenzensysteem in combinatie met de golflengte (oftewel kleur) van het licht dat gebruikt wordt. Volgens de *diffraactielimiet* van Ernst Abbe (vergelijking 1.1 op pagina 1) kan de resolutie van een optische microscoop niet beter zijn dan de helft van de golflengte. Voor zichtbaar licht komt dit neer op een resolutielimiet van ongeveer 200 nanometer.

Voor veel toepassingen is deze resolutie is goed genoeg. Het is bijvoorbeeld mogelijk om de individuele bestanddelen van biologische cellen te bestuderen. Toch zijn er veel toepassingen die een hogere resolutie vragen, zoals bijvoorbeeld onderzoek naar virussen (100 nanometer) en DNA (2 nanometer). Een ander goed voorbeeld is de kwaliteitscontrole van transistors in de moderne elektronica. De kleinste transistoren in moderne telefoon- en computerprocessors zijn tegenwoordig slechts 10 nanometer groot, en kleinere transistoren worden continu ontwikkeld. Om de productie van dergelijke processoren te

kunnen controleren is microscopie een belangrijk middel.

Er bestaan verschillende microscopietechnieken die een hogere resolutie behalen, zoals elektronenmicroscopie, 'scanning tunneling' microscopie en fluorescentiemicroscopie. Toch blijft de techniek achter microscopie een actief wetenschappelijk vakgebied en worden er nog steeds nieuwe technieken ontwikkeld. Dit heeft ermee te maken dat een microscopietechniek normaal gesproken ontwikkeld wordt voor een specifieke toepassing. Met scanning tunneling microscopie is het bijvoorbeeld mogelijk individuele atomen waar te nemen met een resolutie van 0.1 nanometer, maar het is niet mogelijk om verder dan één atoom diep te kijken onder het oppervlak.

In het kader van microscopie met een resolutie in de orde van nanometers is extreem ultraviolet (EUV) licht interessant. EUV, wat met golflengtes tussen 10 en 124 nanometer tussen ultraviolet en röntgenstraling valt, is goed geschikt voor microscopie met hoge resolutie. Daarnaast is EUV erg gevoelig voor de elementaire samenstelling van het materiaal waar naar gekeken wordt. Het is ook mogelijk om door dunne lagen metaal heen te kijken. Er zijn echter een aantal cruciale verschillen tussen zichtbaar licht en EUV die de ontwikkeling van EUV-microscopie bemoeilijken. Van deze complicaties is het gebrek aan traditionele lenzen waarschijnlijk het belangrijkste. Een veelgebruikte methode om dit probleem te omzeilen is *coherent diffractive imaging* (CDI), een lens-vrije techniek waarbij de lenzen vervangen worden door data-analyse op de computer.



Figuur 1: Berekening van de diffractie van monochromatisch, coherent licht. In dit geval belicht een homogene bundel een scherm met daarin een opening in de vorm van een ARCNL-logo. De plaatjes laten het verwachte bundelprofiel zien van direct na de opening links tot ver weg rechts.

---

CDI is gebaseerd op de wetenschap over hoe een lichtgolf zich voortplant. Hieruit volgt namelijk dat, als het profiel van een lichtbundel op een bepaald punt volledig bekend is, het mogelijk is het bundelprofiel op een andere plek (eerder of later) te berekenen. In het voorbeeld van figuur 1 kan het bundelprofiel ver weg van de opening gebruikt worden om het bundelprofiel direct na de opening te berekenen. Hiervoor is het wel noodzakelijk om de *amplitude* en de *fase* te kennen, terwijl camera's alleen de intensiteit en dus amplitude meten. De data-analyse in CDI is erop gericht om de fase te reconstrueren op basis van de amplitudemeting en andere informatie die bekend is over de bundel.

Een voorwaarde voor CDI en correcte fasereconstructie is monochromatische, coherente belichting. Als de lichtbundel bijvoorbeeld meerdere golflengtes bevat, dan detecteert de camera de som van de sterk golflengte-afhankelijke diffractiepatronen. Zoals in figuur 3.4 te zien is, kan dit de fijne details van een diffractiepatroon vervagen, waardoor fasereconstructie onmogelijk is.

## Hogere harmonische generatie

Een interessante lichtbron voor EUV is hogere harmonische generatie (HHG). In tegenstelling tot andere bronnen van coherent EUV licht is een HHG-opstelling compact op te bouwen, zodat de opstelling op een gewone labtafel past. Hogere harmonische generatie begint met een extreem korte en intense lichtpuls, die sterker is dan de Coulomb-potentiaal die elektronen aan hun atomen bindt. De ontwikkeling van een lasersysteem dat dergelijke pulsen levert wordt in hoofdstuk 2 beschreven.

Om hogere harmonischen te genereren wordt de lichtpuls gefocuseerd in een gaswolk van bijvoorbeeld argon. Het elektrisch veld van de lichtpuls wordt daarbij zo sterk dat een elektron uit het atoom kan tunnelen. Dit elektron wordt dan versneld in het lichtveld. Omdat licht een golf is draait het elektrisch veld vervolgens om, waardoor het elektron eerst wordt afgeremd en daarna versneld richting het oorspronkelijke atoom. Zodra het elektron bij het oorspronkelijke atoom terug komt, is er een kans dat het elektron weer geabsorbeerd wordt. De bewegingsenergie van het elektron wordt dan omgezet in een hoog-energetisch (EUV) foton. Aangezien dit proces door een coherente

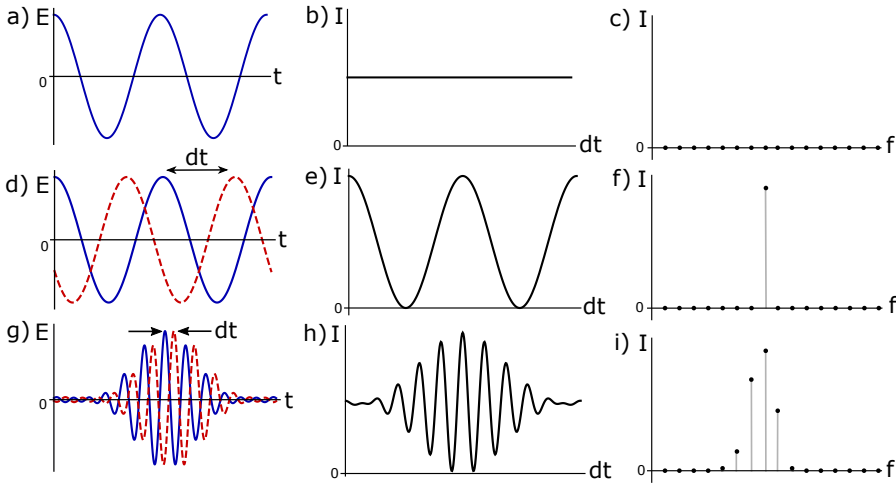
lichtpuls gestuurd word en bij talloze atomen tegelijk gebeurt, ontstaat zo een coherente, laser-achtige EUV-bundel. Aangezien EUV sterk geabsorbeerd wordt door lucht, vind het hele experiment vanaf EUV-generatie tot -detectie plaats in een vacuümkamer.

Hoewel de gegenereerde bundel coherent is, is deze niet monochromatisch. Een typisch HHG-spectrum gegenereerd door een lichtpuls met golflengte  $\lambda_0$  bestaat uit een verzameling smalle pieken waarvan de golflengtes bijvoorbeeld  $\lambda_0/13$ ,  $\lambda_0/15$ ,  $\lambda_0/17$ ,  $\lambda_0/19$ , ... zijn. Het spectrum bevat in dit geval dus de 13de, 15de, 17de, 19de, ... boventonen van de oorspronkelijke lichtgolf, waarop de naam *hogere harmonischen* is gebaseerd. Een veelgebruikte manier om hogere harmonischen te gebruiken voor CDI is met behulp van multilaags EUV-spiegels, die door de precies gecontroleerde dikte van de laagjes slechts een enkele golflengte reflecteren. Dit geeft de benodigde monochromatische coherente EUV-bundel voor CDI. Op deze manier hebben verschillende onderzoeksgroepen HHG gebruikt voor microscopie met een resolutie beter dan 20 nanometer.

## Interferentie van hogere harmonischen

Zoals kleurenfotografie veel meer informatie overbrengt dan zwart-witfotografie, zo zou spectraal opgeloste EUV microscopie (waarbij voor elke golflengte een afbeelding wordt gemeten) een waardevolle techniek zijn voor de moderne wetenschap. Door beelden te vergelijken bij verschillende golflengtes, is het mogelijk om efficiënter gebruik te maken van de elementgevoeligheid van EUV. Ondanks dat HHG coherent licht produceert met veel verschillende golflengtes is het echter niet zo eenvoudig om al deze golflengtes tegelijkertijd te gebruiken voor CDI. In hoofdstuk 4 wordt beschreven hoe het mogelijk is de HHG-bundel spectraal en ruimtelijk opgelost te meten met behulp van fouriertransformatiespectroscopie (FTS). In hoofdstuk 5 gebruiken wij deze methode om spectraal opgeloste CDI te doen.

In FTS, uitgelegd in figuur 2, wordt het spectrum bepaald aan de hand van de interferentie van twee identieke pulsen. Omdat dit principe slechts een enkele intensiteitsdetector nodig heeft, is het mogelijk om met een camera het spectrum op verschillende pixels te



Figuur 2: Het werkingsprincipe van fouriertransformatiespectroscopie. Als een enkele lichtgolf (a) op een lichtsensoren zoals een camera valt, dan detecteert die een constante intensiteit (b). Hier is geen nuttige spectrale informatie uit te winnen (c). Als we dan de som van twee identieke golven met een controleerbaar tijdsverschil  $dt$  (d) meten, dan hangt de intensiteit van het tijdsverschil af (e). Met behulp van een fouriertransformatie is het dan mogelijk de frequentie van de golf te berekenen (f). Dit werkt ook twee identieke complexere golven (g). Uit het resulterende interferentiepatroon (h) kan dan het volledige spectrum berekend worden (i).

meten. Dit zou gebruikt kunnen worden om bundels met een complex ruimtelijk en spectraal profiel, zoals een meerkleurig diffractiepatroon, te meten. Dit is een opvallend verschil met andere methodes om het spectrum te meten, waarbij de verschillende golflengtes bijvoorbeeld door een tralie ruimtelijk gescheiden worden. FTS wordt veel gebruikt voor spectroscopie van infrarood en zichtbaar licht. Een interessante toepassing is spectraal opgeloste fotografie waarbij meer informatie wordt verkregen dan in traditionele kleurenfotografie [173]. Voor EUV wordt FTS echter bemoeilijkt door de korte golflengte en de limitaties van optische elementen voor EUV. Anders dan voor langere golflengtes is het niet mogelijk om met een bundelsplitser een directe kopie van

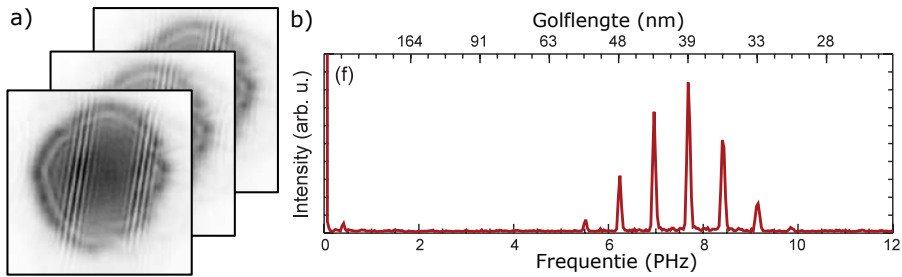
de bundel te maken. Een mogelijke alternatieve oplossing is om de bundel ruimtelijk te splitsen met behulp van een gespleten spiegel waarvan de helften ten opzichte van elkaar kunnen bewegen. In deze situatie leidt diffractie aan de rand van de spiegels vaak ertoe dat de individuele bundels een complex en verschillend intensiteitsprofiel krijgen. Aangezien een complex bundelprofiel het beeld vervormt in CDI, zijn dergelijke 'split-mirror' technieken niet goed geschikt voor CDI.

Om dit probleem te voorkomen, maken wij gebruik van de coherentie van hogere harmonische generatie. Twee identieke laserpulsen in identieke gaswolken genereren daarom precies dezelfde EUV-lichtpuls. Zulke identieke laserpulsen zijn relatief makkelijk te produceren. Door de EUV-pulsen te overlappen en in de tijd te verschuiven is het dus mogelijk om EUV-FTS te doen zonder speciale optische elementen voor extreem ultraviolet licht. Het is daarbij wel belangrijk dat de stabiliteit van het tijdsverschil tussen de pulsen beter is dan een fractie van de oscillatieperiode van het licht. De meeste interferometers voor zichtbaar licht zijn niet stabiel genoeg voor EUV, waarvan de oscillatieperiode slechts een fractie van een femtoseconde is. In hoofdstuk 4 maken wij daarom gebruik van een interferometer gebaseerd op dubbelbrekende wiggen (smalle prisma's). Een enkele laserpuls wordt hierin opgesplitst in twee pulsen met verschillende polarisatie. Deze pulsen zien een verschillende brekingsindex en worden dus opgesplitst in tijd. Het tijdsverschil tussen de pulsen kan op attoseconde-niveau gecontroleerd worden door een wig verder in de bundel te schuiven en zo meer dubbelbrekend materiaal te introduceren. Aangezien de laserpulsen hetzelfde pad volgen kunnen vibraties van spiegels het tijdsverschil tussen de pulsen niet beïnvloeden, waardoor de interferometer extreem stabiel is.

De interferometer wordt als een module tussen de laser en de hogere harmonische generatie geplaatst. De oorspronkelijke laserpulsen worden opgesplitst in pulsparen met een tijdsverschil tussen de  $-25$  en  $+25$  femtoseconden, en vervolgens gefocusseerd in een gaswolk in de vacuümkamer. Om de gasdruk in de rest van de vacuümkamer zo laag mogelijk te houden gebruiken we een gepulste klep om de gaswolk te maken. Belangrijk is dat de laatste wig van de interferometer zo gedraaid is dat de twee pulsen van elk paar op ongeveer 0.3 millimeter

---

afstand van elkaar gefocuseerd worden. Dit zorgt ervoor dat de het sterke elektrische veld van de ene puls de hogere harmonische generatie van de andere puls niet beïnvloed en dat onafhankelijk van het tijdsverschil tussen de pulsen gelijke EUV-pulsen worden gegenereerd.



Figuur 3: EUV spectrum dat hoort bij de meting die in de marges van deze thesis geprint is (symbolisch weergegeven met **a**). Om het spectrum (**b**) te berekenen, is het tijdsafhankelijke interferentiepatroon fouriergetransformeerd en zijn de spectra van de 100 pixels opgeteld.

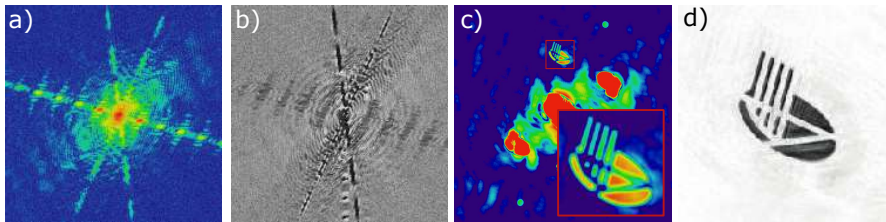
Na de hogere harmonische generatie wordt het infrarode laserlicht geblokkeerd door een 200 nanometer dun stuk aluminiumfolie. Dit werkt als een spiegel voor zichtbaar en infrarood licht, maar is relatief transparant voor EUV. Pas dan is het mogelijk om met een digitale camera het EUV te meten. Typische beelden van de gemeten EUV-bundel zijn te zien in de marges van dit proefschrift tussen bladzijde 1 en 135. De rechte, bijna verticale lijnen in deze plaatjes zijn het gevolg van interferentie tussen de twee EUV-pulsen. Deze lijnen verschuiven van plaatje tot plaatje omdat elk van deze metingen is gedaan met een ander tijdsverschil tussen de pulsen. Dit proefschrift laat zo een (gedeelte van een) FTS-meting zien. Het ruimtelijk opgeloste spectrum kan vervolgens berekend worden door voor elke pixel op de camera het tijdsafhankelijke interferentiepatroon te fouriertransformeren (figuur 3). In hoofdstuk 4 laten wij zien dat deze meting gebruikt kan worden voor golflengtes tussen 17 en 55 nanometer, kortere golflengtes dan ooit gedemonstreerd in fouriertransformatiespectroscopie.

## Spectraal opgeloste diffractie microscopie

Om de metingen voor spectraal opgeloste microscopie te doen met onze opstelling volstaat het om een object tussen de HHG en de camera te plaatsen. Als eerst hebben wij zo de transmissie van een titanium membraan met een gat erin bepaald. In dit geval was het object zo groot en stond het zo dicht bij de camera dat diffractie geen rol speelde. Het was dus mogelijk om de transmissie van het membraan en die van het gat te onderscheiden op basis van de locatie op de camera (zie figuur 4.5). Dit levert een direct gekalibreerde meting van de spectrale transmissie van het membraan.

Hoewel dit experiment al als microscopie beschouwd kan worden is de resolutie enkele tientallen micrometers, gelimiteerd door het formaat van de pixels. In hoofdstuk 5 wordt beschreven hoe een betere resolutie behaald kan worden met behulp van CDI. In de eerste meting combineren we CDI met holografie door enkele referentiegaatjes te plaatsen naast het object. Aan de hand van de interferentie tussen de diffractie van het object en van de referentie is het mogelijk om een afbeelding van het object te krijgen in een enkele, relatief simpele berekening. Deze eerste versie kan dan verbeterd worden met behulp van iteratieve fasereconstructie, wat tot een hogere resolutie en minder ruis kan leiden. De resultaten hiervan zijn voor één golflengte te zien in figuur 4. Uit de volledige dataset was het mogelijk om voor vier golflengten beelden te reconstrueren (figuur 5.5).

Een belangrijke conclusie van dit experiment is dat de diffractiepatronen die door EUV-FTS gemeten worden niet volledig gelijk zijn aan de diffractiepatronen die andere CDI experimenten meten. Dit komt doordat de twee EUV-pulsen op verschillende plekken worden gegenereerd zodat er een kleine hoek tussen de twee bundels is. Het verschil in de meting zorgt ervoor dat er ook een ander fasereconstructiealgoritme nodig is. Het eerste deel van hoofdstuk 5 beschrijft de ontwikkeling en karakterisatie van een dergelijk algoritme. Het blijkt dat FTS meer informatie geeft over de fase van het diffractiepatroon maar minder over de amplitude van het diffractiepatroon. Uit de karakterisatie van het algoritme, waarbij onze methode wordt vergeleken met standaard CDI, blijkt dat de extra fase-informatie leidt tot een efficiënter reconstructiealgoritme. Dat wil zeggen dat het algoritme vergelijkbare



Figuur 4: **a:** Een van de monochromatische diffractiepatronen (golflengte 32 nanometer) gemeten met FTS met een ARCNL logo in de bundel. **b:** Het gemeten FTS-fasepatroon, dat het faseverschil tussen de twee EUV-bundels aangeeft. **c:** Holografische reconstructie van het object op basis van de data uit **a** en **b**. **d:** Het uiteindelijke beeld na volledige fasereconstructie.

kwaliteit levert in minder rekenstappen. Uit andere resultaten in dit hoofdstuk blijkt bovendien dat deze manier van microscopie ook werkt voor significant complexere objecten (figuur 5.6).

Het is duidelijk dat FTS spectraal opgeloste microscopie met hogere harmonischen mogelijk maakt. De beste ruimtelijke resolutie in de gepresenteerde experimenten is 270 nanometer. Deze resolutie is begrensd door het lage aantal fotonen dat met grote hoek van het object verstrooit. Het is dus mogelijk om de resolutie te verbeteren door langer te meten en door objecten te gebruiken die meer fijne structuur bevatten. De spectrale resolutie is ruim voldoende om de individuele hogere harmonischen te kunnen waarnemen. Een van de vervolgonderzoeken is het benutten van deze spectrale resolutie om zo te kunnen meten wat de elementaire samenstelling is van een object op verschillende plaatsen in dat object.

## Fase metrologie

De fase-gevoeligheid van FTS kan ook direct gebruikt worden voor precisemetingen in het EUV domein. Een voorbeeld hiervan is het meten van materiaaleigenschappen zoals de brekingsindex en de absorptiecoëfficiënt. In hoofdstuk 6 gebruiken we FTS om de faseverschuiving van EUV licht dat door dunne lagen metaal beweegt te meten.

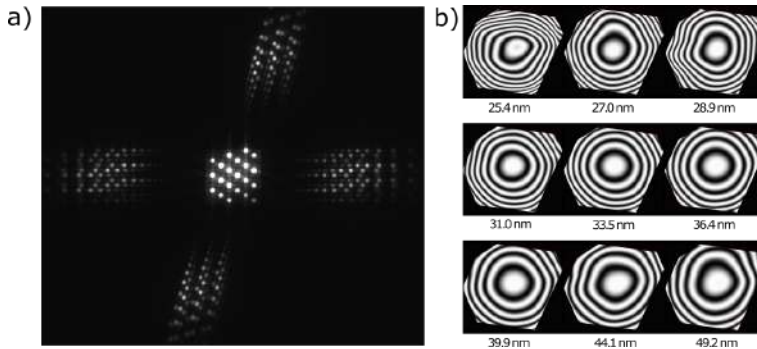
Dit levert een directe meting van de dispersie van dat materiaal en kan gebruikt worden om de golflengte-afhankelijke brekingsindex te bepalen. Omdat deze methode werkt voor alle golflengtes die met HHG geproduceerd kunnen worden, overbrugt deze methode het gat tussen UV en röntgenstraling, waar relatief weinig informatie bekend is over de brekingsindex van materialen.

Voor deze meting gebruiken we een gekromde spiegel om de EUV-pulsen te herfocusseren. Daarbij worden de twee pulsen op verschillende plekken gefocusseerd. In het focus plaatsen we een gestructureerd siliciumnitride membraan, zodat een van de bundels door een metaallaag op het membraan loopt en de andere bundel door een gat in het membraan loopt (figuur 6.1). De eerste bundel wordt daarbij extra vertraagd door de aanwezigheid van het membraan. Deze faseverschuiving kan wordt direct gemeten met FTS. Voor de vier verschillende materialen die we gemeten hebben vinden we een goede overeenkomst met de verwachting op basis van de best bekende waarden voor de brekingsindex.

## Gecontroleerde diffractie als meetapparaat

Diffractie is sterk golffront-afhankelijk. Een gecollimeerde bundel leidt bijvoorbeeld tot een ander diffractiepatroon dan een divergerende bundel. In CDI wordt dit gebruikt om het golffront van een onbekend object te bepalen. Als het object bekend is, dan is de reconstructie van het golffront vaak makkelijker en betrouwbaarder. In hoofdstuk 8 beschrijven wij hoe het mogelijk is om met een slim gekozen object het golffront te reconstrueren van de verschillende hogere harmonischen in een enkele meting, iets wat met andere methodes niet mogelijk is. Hiervoor maken we gebruik van een Hartmann-sensor met tralies in de openingen van de sensor.

Deze spectraal opgeloste Hartmann-sensor kan goed gebruikt worden om de kwaliteit van HHG bundels te controleren. De gemeten golffronten kunnen gebruikt worden als referentie in een spectraal opgelost CDI experiment. Daarnaast is goede golffrontkennis van cruciaal belang voor talloze precisieingen. Om deze reden is het concept van de spectraal opgeloste golffrontsensor dan ook gepatenteerd.



Figuur 5: **a**: Diffractie van een HHG-bundel aan de spectraal opgeloste Hartmann-sensor. **b**: Gereconstrueerde golffronten van verschillende harmonischen op basis van **a**.

## Metten aan de hogere harmonische generatie

Een van de toepassingen van de spectraal opgeloste golffrontsensor is de studie van het proces *hogere harmonische generatie* zelf. HHG is een van de bekendste voorbeelden van *strong field physics*, waarbij het elektrische veld van de laser te sterk is om als een verstoring van de Coulombpotentialaal gezien te worden. In begin 2018 toonden H. Wikmark en zijn collega's uit de onderzoeksgroep van Prof. A. L'Huillier aan dat hogere harmonischen met een golflengte-afhankelijk golffront geproduceerd kunnen worden door een wisselwerking tussen het golffront van de laserpuls en de beweging van elektronen in het sterke veld.

Het ligt voor de hand om dit effect te meten met de spectraal opgeloste Hartmann-sensor. Hoofdstuk 9 beschrijft het experimentele werk en de resultaten van een samenwerking tussen de groep in Lund en onze groep in Amsterdam met dit doel. Voor dit experiment hebben we gebruik gemaakt van de hoge intensiteit HHG bundel in Lund. In deze opstelling is het mogelijk om de golffrontkromming van de laser gecontroleerd aan te passen met een buigbare spiegel, waardoor een goed gecontroleerde meting mogelijk is. Daarnaast is de pulsenergie van de laser zo groot dat het meten van golffronten van individuele EUV-pulsen een mogelijkheid is.

Om de juiste veldsterkte te bereiken met deze hoge puls energie wordt de laser zwak gefocuseerd, met slechts een licht gekromd golffront in de gas-cel waar HHG plaatsvindt. Dit leidt tot een weinig divergente EUV-bundel die pas vier meter verderop gemeten kan worden. De combinatie van deze factoren zorgt ervoor dat de golffrontkromming van de hogere harmonischen bij de sensor zeer zwak is. In onze metingen was het daarom moeilijk om het signaal te onderscheiden van de ruis, die voornamelijk een gevolg is van het relatief sterke achtergrondlicht op de camera. We hebben slechts in één situatie een duidelijk golflengte-afhankelijk signaal waargenomen, maar dit resultaat kan niet direct gecorreleerd worden aan de voorspelling van H. Wikmark *et al.*

Ten slotte worden er verschillende aanpassingen voorgesteld om het golflengte-afhankelijke golffront te meten. Dit omvat het verbeteren van de signaal-ruis verhouding in de ruwe data, het aanpassen van de golffrontsensor om het golffront op meer punten te meten, en het aanpassen van de meetopstelling om het verwachtte effect te verbeteren.

## Conclusies

In dit proefschrift zijn er verschillende spectraal opgeloste meetmethoden met hogere harmonischen gepresenteerd. Dankzij een ultrastabiele interferometer met dubbelbrekende wiggen is het mogelijk om FTS uit te voeren met het volledige spectrum gegenereerd met hogere harmonische generatie. Dit maakt het mogelijk om hoge ruimtelijke resolutie te combineren met spectrale resolutie. De fasegevoeligheid van deze meting maakt FTS uitermate geschikt voor spectraal opgeloste microscopie. FTS kan ook direct ingezet worden om materiaaleigenschappen te meten. Een andere methode om spectraal opgeloste metingen te doen, specifiek aan de HHG-bundel zelf, is door middel van diffractie aan een speciaal daarvoor ontwikkeld masker. Wij hebben dit gebruikt om het golffront van individuele harmonischen te bepalen. Dit levert gedetailleerde informatie over het HHG-proces die waardevol is voor EUV precisie metrologie en microscopie. Met fouriertransformatiespectroscopie en gecontroleerde diffractie wordt het mogelijk om beter van het unieke spectrum van hogere harmonischen gebruik te maken.

# Dankwoord

Zonder de hulp van een grote groep mensen had dit proefschrift niet zo kunnen ontstaan. Tijdens mijn promotieproject heb ik bij veel mensen op de een of andere manier steun gevonden. Op deze laatste pagina's wil ik die mensen graag bedanken.

Ten eerste is dat Stefan Witte. Stefan, ik heb enorm genoten van ruim vijf jaar werk onder jou begeleiding. Ik heb veel van je geleerd, en volgens mij hebben we ook veel bereikt. Dank je voor de fijne onderzoeksgroep, zowel aan de VU als bij ARCNL, en dank je voor je rustige houding als ik voor de zoveelste keer een optische isolator kapot geschoten had.

Ik kan Stefan niet noemen zonder ook aan Kjeld Eikema te denken. Kjeld, over een periode van bijna tien jaar heb ik, geloof ik, vijf projecten van verschillend formaat bij jou in de onderzoeksgroep gedaan. Ik heb me altijd hartelijk welkom gevoeld en ook altijd veel geleerd, niet in het minst over communicatie: exact en to-the-point. Dank je voor deze mooie tijd.

Daniel, dank je dat ik als master-student bij jou aan de laser kon knutselen. Zonder jouw werk had ik er nooit zoveel HHG-experimenten mee had kunnen doen.

Denis, toen jij bij ons in het lab kwam, ging alles ineens zoveel sneller. Zonder jou was het interferometrie-artikel nooit zo goed geworden als het nu is.

Lars, the things you can do with a focused ion beam are absolutely amazing. Thanks for the bounce amplifier and all the work on the spectral Hartmann sensor.

Anne and Kevin, thank you both for joining me for the last part of my PhD and for continuing the work where I left off. With Anne working on the phase retrieval and Kevin operating the laser, I believe you will produce many amazing results. I look forward to it!

Minstens net zo belangrijk als de wetenschappelijke staf is de tech-

nische ondersteuning. Met name wil ik Rob Kortekaas en Nik Noest bedanken, maar natuurlijk ook de volledige teams van de mechanische en elektronische werkplaatsen van de VU en het AMOLF. Jullie stonden altijd klaar als ik iets nodig had.

During my PhD, I have been in close contact with several other research groups. Thank you, Hampus, Per and all the others in Lund, for the great measurement campaign and a good time in Lund. Thank you Nan, Peter, Seth, Sander and the others at ASML, for the fruitful collaboration and your interest in our work at ARCNL. Thank you also to Sander, Wim and the others at TU Delft for your useful analytical insights and interest in our work.

Wim Ubachs, Rick Bethlem en ook Wim Vassen, hartelijk bedankt voor de geweldige AML groep, de jaarlijkse uitjes en de borrels. Thanks also to all the others in the AML group. Our daily lunches and regular *borrels*, as well as all the scientific get-togethers have been great fun.

Thanks to the EUV Generation & Imaging group at ARCNL. Due to the distance between VU and ARCNL, I have spoken less to all of you than I would have liked, but seeing you build up all the new experiments has been a wonderful experience. Keep up the good work!

Ruud en Laura, de afgelopen jaren hebben we meer samen gedaan dan ik kan onthouden: van samen studeren voor onze master tot een biertje drinken in de zon of samen op ski-vakantie. Dank jullie voor alle gezelligheid. Ook Caspar, Dianne, Eelco, Wesley en Vincent, bedankt voor alle afleiding in de vorm van fietstochtjes, borrels en vakanties.

Aan mijn familie, bedankt voor jullie steun en voortdurende interesse in mijn werk. Ik heb veel van jullie geleerd over de communicatie van wetenschappelijk onderzoek, en dat ik mijn werk enigzins begrijpelijk heb kunnen uitleggen.

Lieve Cyriana, dank je voor alles.